Title	Voltage modulation of interfacial Dzyaloshinskii-Moriya interaction in artificial multilayer
Author(s)	縄岡, 孝平
Citation	大阪大学, 2017, 博士論文
Version Type	VoR
URL	https://doi.org/10.18910/61818
rights	
Note	

Voltage modulation of *interfacial* Dzyaloshinskii-Moriya interaction in artificial multilayer

Kohei NAWAOKA

MARCH 2017

Voltage modulation of *interfacial* Dzyaloshinskii-Moriya interaction in artificial multilayer
Kohei NAWAOKA
MARCH 2017

Voltage modulation of *interfacial* Dzyaloshinskii-Moriya interaction in artificial multilayer

A dissertation submitted to
The GRADUATE SCHOOL OF ENGINEERING SCIENCE
OSAKA UNIVERSITY
in partial fulfillment of the requirement for the degree of
DOCTOR OF PHILOSOPHY IN SCIENCE

BY

Kohei NAWAOKA

MARCH 2017

ABSTRACT

Magnetic Random Access Memory (MRAM) is one of the most attractive new functional device in the research field of Spintronics. This MRAM memorizes information by using magnetization, therefore, it is non-volatile memory. MRAM is superior in terms of reliability and operational speed but is inferior in terms of information-writing energy to the other non-volatile memory, since for writing, spin-polarized current is used. The voltage control of magnetism is expected to be able to reduce writing energy, and a lot of research about voltage controlled magnetism have been performed. Voltage-induced Fe|MgO *interfacial* anisotropy change is known as one of the candidate to control magnetization direction by externally input voltage. Recently, magnetization direction control by using pulse voltage was achieved by using this voltage effect by Shiota. They mentioned that its technique can reduce writing energy and also high reliability and that high speed operation can be guaranteed as well as spin-polarized current writing. However, its technique requires ultra-short pulse (< 1ns) and thickness of ferromagnetic layer is limited to few monolayer to realize magnetization switching, therefore enough thermal stability cannot be obtained. In this research, I discovered new voltage effect in artificial multilayer (**voltage-induced *interfacial* Dzyaloshinskii-Moriya interaction (DMI)**) to realize magnetization direction switching without pulse voltage. I also proposed new film structure and estimated them to enhance voltage-induced *interfacial* anisotropy change and voltage-induced *interfacial* DMI change.

I focused on voltage-induced *interfacial* DMI change as new voltage effect. This *interfacial* DMI was firstly observed by Bode et al in 2009 and it can be induced at surface and/or interface, where spatial inversion symmetry was broken, together with spin-orbit interaction. The bulk DMI is known as voltage-controllable and leads to the formation of multiferroics in oxides. Therefore, *interfacial* DMI may also be voltage-controllable, and its voltage control makes it possible to multiferroic-control of magnetization in artificial multilayer. This multiferroic-control will realize voltage switching of magnetization direction without pulse voltage. In this research, I excited propagating spin waves in artificial multilayer, and by using its chirality, depending on propagation direction, I estimated voltage-induced *interfacial* DMI change in artificial multilayer.

Chapter 2 describes the dynamics of spin waves. By applying magnetic field normal to spin-wave propagation direction, I excited Magneto static surface spin waves. I derive **a dispersion relation of MSSW** from the basic electromagnetics and Landau Lifshitz equation.

Chapter 3 describe the sample fabrication, in terms of **Film fabrication and microfabrication**.

Chapter 4 describes the development of the measurement technique and the analysis method for **voltage-control of propagating spin waves in artificial multilayer consisting of Au|Fe|MgO system**. Artificial multilayer was micro-fabricated to the spin-wave device with two micro-sized antennas, and the property of propagating spin waves were investigated by electric measurement. By applying external voltage, I succeeded in voltage control of propagating spin waves in artificial multilayer first in the world. I also revealed that voltage modulated spin-wave-resonant frequency and voltage-induced *interfacial* anisotropy change played a dominant role for it.

Chapter 5 and 6 describe **voltage-induced *interfacial* DMI change**. Spin waves were investigated by the almost same method as Chapter 3. I succeeded in observing voltage-induced *interfacial* DMI change first in the world by investigating spin-wave-propagation-diction dependent voltage effect, since the chirality of spin waves depends on the propagation direction of spin waves. These results suggest not only the possibility for multiferroic-voltage-control of artificial multilayer but also the possibility of voltage-control of magnetic skyrmion, which is one of the smallest magnetic structure. I also demonstrated enhancement of voltage induced *interfacial* anisotropy change and voltage induced *interfacial* DMI change by inserting few monolayer Pt into Fe|MgO interface.

論文内容の要旨

磁気ランダムアクセスメモリ(MRAM)は情報の保存に磁性を利用した不揮発メモリであり、スピントロニクスの領域において特に注目を集めている新機能性デバイスである。他の不揮発メモリと比較した際、現在一部実用化されつつある MRAM は高速動作と高信頼性が期待できる一方で、スピン偏極電流を用いた書き込みを行っているためその電力が大きいという問題を抱えている。電圧による磁性層制御はこの書き込み電力低減を期待できる手法として期待され、近年様々な電圧による磁性制御に関する研究が行われてきている。中でも電圧による Fe|MgO 界面の磁気異方性変調を応用した、パルス電圧による金属ナノ磁性体の磁化反転はこれまでのスピン偏極電流によるものに比べ書き込み電力低減が実現でき、動作速度かつ信頼性において優れる他、劣化も少ない理想的な磁化反転手法として注目を集めている。しかし、この技術は ns 以下の超短パルスが不可欠である他、効果が小さいため強磁性数原子層における磁化反転しか実現できないという課題を抱えている。そこで本研究では、パルス電圧を用いない磁化反転技術を実現するため、新規の磁性の電圧変調現象探索を行った**(界面ジャロシンスキー守谷相互作用の電圧変調(DMI))**。また、電圧誘起界面磁気異方性変調と界面 DMI の電圧変調量を増大させるための薄膜構造の提案、評価を行った。

新規の磁性の電圧変調現象として本研究では金属人工格子における界面ジャロシンスキー守谷相互作用(DMI)の電圧変調に注目した。界面ジャロシンスキー守谷相互作用は近年になり観測されるようになった、界面における空間反転対称性の破れとスピン軌道相互作用により発現する界面の効果である。バルク酸化物において観測されているバルク DMI は電圧制御可能な磁気的相互作用として知られている。そのため金属人工格子における界面 DMI も同様に電圧制御可能であるはずであり、電圧変調が可能となれば金属人工格子においてもマルチフェロ的な磁性層の制御が可能となり、パルス電圧を必要としない磁化反転が実現可能となることを意味する。本研究では金属人工格子中に伝搬スピン波を励起し、スピン波の伝搬方向に依存したカイラリティを利用しこの界面 DMI の電圧変調の評価を行った。

2 節ではスピン波ダイナミクスに関する紹介を行う。本研究では磁場を面内かつスピン波の伝搬方向に対し垂直方向に印可することで静磁表面波を励起した。ここでは**静磁表面波の分散関係を基本的な電磁気学とランラウリフシッツ方程式より導出する**。

3 節ではサンプル作成に関して、特に**分子線エピタキシー法による薄膜作成と微細加工によるスピン波素子の作成**に関して紹介する。

4 節では Au|Fe|MgO 構造を有する**金属人工格子中を伝搬するスピン波の電圧変調に関して実験方法の確立と評価手法の確立**を行う。マイクロメートルサイズのアンテナを有するスピン波素子を作成し、電気的手法によりスピン波の検出を行った。外部電圧印可による金属人工格子を伝搬するスピン波の電圧変調の観測に世界に先駆けて成功した他、電圧によりスピン波の共鳴磁場が変調された事、界面磁気異方性の電圧変調が支配的に寄与していることを明らかにした。

5、6 節では**界面 DMI の電圧変調をスピン波の電圧変調を応用し実験的観測**を行う。スピン波は 3 節と同様にスピン波素子を電気測定により評価した。スピン波のカイラリティが伝搬方向に依存することを応用し、伝搬方向に依存した電圧印可共鳴周波数変調量を精査することで、世界に先駆けて界面 DMI が電圧変調可能であることを明らかにした。これは金属人工格子におけるマルチフェロ的な電圧制御の実現の可能性を示しただけでなく、磁性の最小格子となりえるスキルミオン格子の電圧制御の可能性までも示した。更に Fe|MgO 界面に数原子層の Pt を挿入することで界面 DMI の電圧変調量と界面磁気異方性変調の変調量の増大を実現させた。

CONTENTS

Chapter 1. Introduction

Spintronics is one of the research area in condensed matter physics where electron-charge and electron-spin in the solid are treated evenly. By treating them evenly, many new physical phenomena were observed, and new functional devices, based on new physics, were proposed and some of them were produced. One of the most functional device in Spintronics is Magnetic Random Access Memory (MRAM). It is a non-volatile memory, since magnetization direction is used to memorize information. To read the magnetization direction of MRAM, Magneto Resistive (MR) ratio, especially Tunnel Magneto resistive ratio (TMR), is used. In this chapter, first, I introduce two contents; MR ratio, electrical control of magnetization direction. Then, I simply describe the recent research of interfacial Dzyaloshinskii-Moriya interaction. Finally, I show the purpose of this research.

1.1 MR effect

Generally, the magneto resistive change is electric resistance change in solid device attributed to the change of the external magnetic field. MR effect was firstly observed in Fe and Ni by Thomson in 1857[1]. Then, the research of MR effect was shifted to Anisotropic Magneto Resistance (AMR), which is few percent change in resistance depending on relative angle between Magnetization and current flow, in 3-*d* transition metals[3]. This AMR effect is attributed to the spin-orbit interaction, and large spin-orbit interaction enhances its effect.

In 1988-1989, Fert in Paris and Grünberg in Jülich were reported Giant Magneto Resistance (GMR) effect, which was one of the greatest discovery in spintronics. This GMR was observed in (Fe(001)|Cr(001)) multilayer structure as shown in Fig. 1. By sandwiching non-magnetic layer, which is Cr, with ferromagnetic layer, which is Fe, inter-layer exchange coupling can be induced to the ferromagnetic films. Because of this inter-layer exchange coupling, magnetization direction of two ferromagnetic layer separated by non-magnetic layer becomes antiparallel without external magnetic field. The origin of GMR attributes to this coupling effect. Most of the early research of GMR was focused on Current flows in the film plane (CIP), on the other hands, current flows perpendicular to the film plane (CPP) was focused in recent. This Discovery of GMR was the milestone of the research of spintronics. This GMR effect was also used for electric device, such as reading head of Hard Disk Drive (HDD), which reads leak magnetic field of disk, and enhanced their specific greatly. Because of these achievement, Fert and Grunberg won

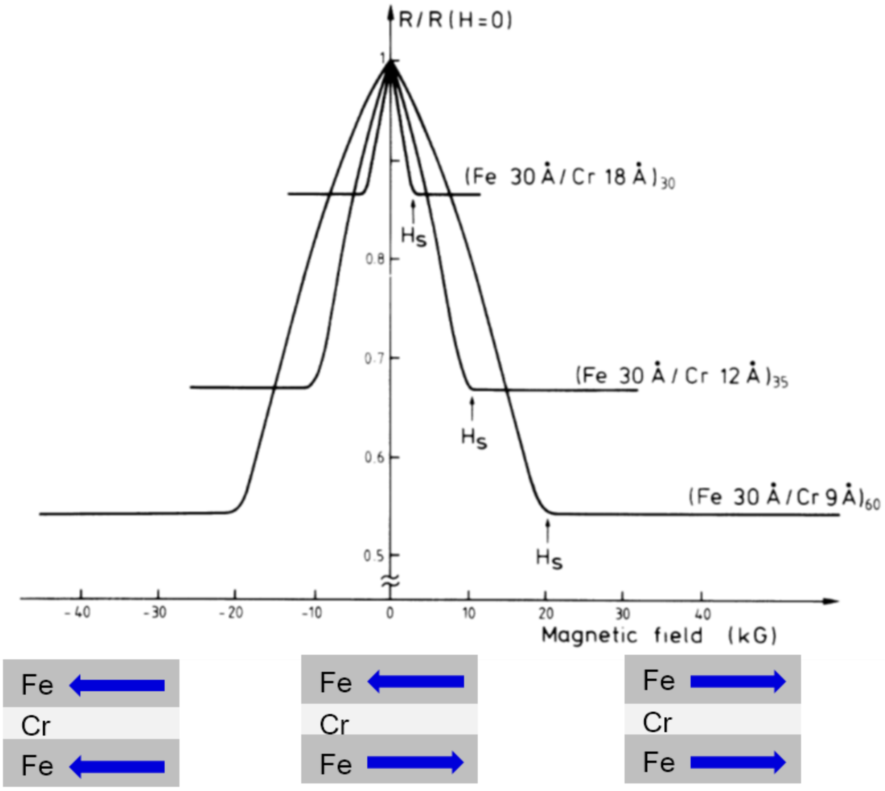

Figure. 1 Typical GMR curves observed in Fe(100)|Cr(100) multilayer reported by Baibich[4]

When large magnetic field was applied, magnetization direction of Fes were saturated to the magnetic field direction. On the other hands, when magnetic field was small, magnetization direction of Fes became antiparallel because of inter-layer exchange coupling.

the Nobel Prize in 2008.

The TMR is also related to the relative angle between two ferromagnets. The difference between TMR and GMR is the separation layer. For the case of TMR, insulating layer (AlOx, MgO, etc.) is employed therefore electron conduction depends on tunneling effect. Therefore, their film stacks are called as magnetic tunnel Junction (MTJ). The TMR was firstly observed in Fe|Ge|Co by Julliere in 1975[2]. TMR was observed before GMR, however, its ratio was about 10 % and large TMR ratio was only observed below 4 K, therefore, it was not much attracted at that time. In 1995, Miyazaki and Moodera reported large MR ratio (~20 %) at room temperature by using AlOx amorphous layer[6,7]. These observed MR ratios were larger than that of GMR at that time and they were observed at room temperature, therefore, AlOx based TMR device was also used as new reading head of HDD.

In 2001, Bulter and Mathon predicted a huge TMR ratio (> 1000 %)in Fe(100)|MgO(100)|MgO(100) structure by first-principle calculation[8,9]. These huge TMR are attributed to the coherent tunneling of electron-spin; that is, for the case of amorphous AlOx, electron-spin cannot transverse insulating layer coherently because of scattering, on the other hand, for the case of single crystalline MgO, electron-spin can transverse insulating layer without scattering. After this prediction, many experiments to fabricate MgO-based MTJ were conducted. In 2004, Yuasa and Parkin demonstrated huge TMR ratios (~200 %) by fabricating MgO-based MTJ[10-12]. These high TMR ratios make it possible to design new MTJ-based functional devices; oscillator, sensor, etc. Generally, recent MRAM consists of MgO-based MTJ. By using this TMR effect, we can easily detect the direction of magnetization as change of resistance. In next section, I describe electrical-magnetization control technique.

1.2 Electrical control of magnetization direction

To develop MRAM, we have to control magnetization direction of MTJ electrically. In this subsection, I simply describe the history of the switching technique of magnetization direction first. Next, I focus on “voltage effect” observed in artificial multilayer. Finally, I describe the current problem of voltage-induced magnetization direction switching and propose the idea to solve their problems.

In early stage of development of MRAM, additional magnetic field was used to control magnetization direction. A schematic image of a cell of MRAM is shown in Fig. 2 (a). To switch magnetization direction, electric current is injected to the wire above an MTJ, and Oersted magnetic field can be induced to the MTJ as red arrow. Then, if magnetic field is enoughly large, magnetization direction can be switched. The idea of switching is very simple, however, this switching technique has many problems,

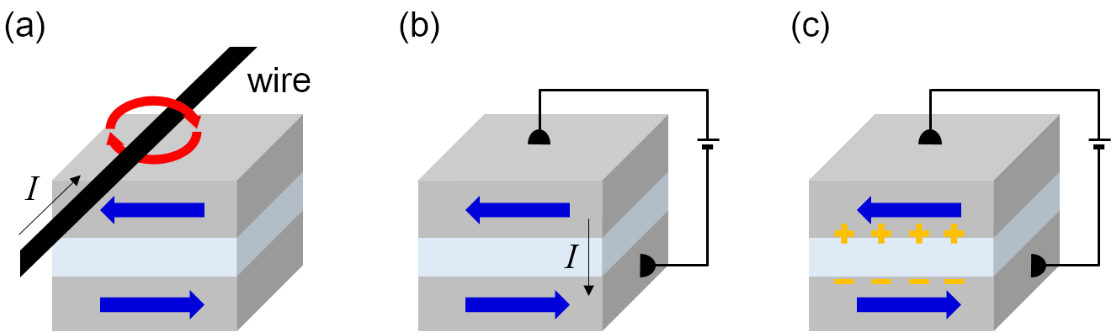

Figure. 2 Schematic image of control techniques
(a) External additional magnetic field. (b) Spin-current injection. (c) Voltage induction

especially in terms of integration, since magnetic field produced by wire affects to neighborhood MTJ. In contrast, in Fig. 2 (b) electric current is directly injected to the MTJ. By injecting electric current into ferromagnetic layer, conduction electron can be spin polarized, therefore, electric current becomes spin-polarized current. By injecting this spin-polarized current to the other ferromagnetic layer, magnetization direction can be switched because of momentum conservation. This switching technique, called as spin-transfer switching, can solve the problem of integration. When we make MTJ smaller, required total spin moment can be reduced; that is, we can reduce the required electric current. Therefore, this technique excels in terms of scaling and writing-energy consumption. Recent MRAM is based on this switching technique. However, if we can control magnetization direction with external voltage shown in Fig. 2 (c), we may reduce furthermore writing-energy consumption.

Recently, many research was performed to control magnetization direction with voltage. By attaching piezo device to the MTJ, we can control magnetic property of MTJ through the magneto-striction change[13]. However, this voltage control may reduce rewriting-tolerance of MRAM, therefore, it doesn't suit to control magnetization direction in MTJ. For the case of direct-voltage-application to the ferromagnetic film, there were two famous voltage induced effects; one was carrier injection to the ferromagnetic semiconductor[15-15] and the other was multiferroic control by using DMI in Bulk Oxides[16-18]. In ferromagnetic semiconductor, not only voltage control magnetic anisotropy and voltage induced Curie temperature change but also voltage-induced switch of magnetization direction was also demonstrated. However, because of very low Curie temperature (< 50 K) of ferromagnetic semiconductor, it doesn't suit for applying to MRAM. Bulk Oxides doesn't match to current microfabrication process of electric device, therefore, it also doesn't suit for applying MRAM.

The voltage induced anisotropy change in 3*d*-transition metal, reported in 2007 by Weisheit first, wass one of the most attractive technique to manipulate magnetic property with voltage[19]. They applied large electric field to the epitaxially grown FePt and FePd (2 and 4 nm thickness) by using ion liquid shown in Fig. 2 (a) and by measuring magnetization curve by magneto optical kerr effect (MOKE), they succeeded in measuring voltage-induced magnetic anisotropy change at room temperature shown in Fig. 2 (b). Generally, electric field is shield on the metal surface, therefore, electric field cannot act on the inside of metallic ferromagnet. However, electric field can be applied to few monolayer surface ferromagnets. Therefore, the interfacial property, which is *interfacial* anisotropy here, can be modulated. In this research, they directly sinked artificial multilayers into the ion liquid, so this voltage-induced *interfacial* anisotropy

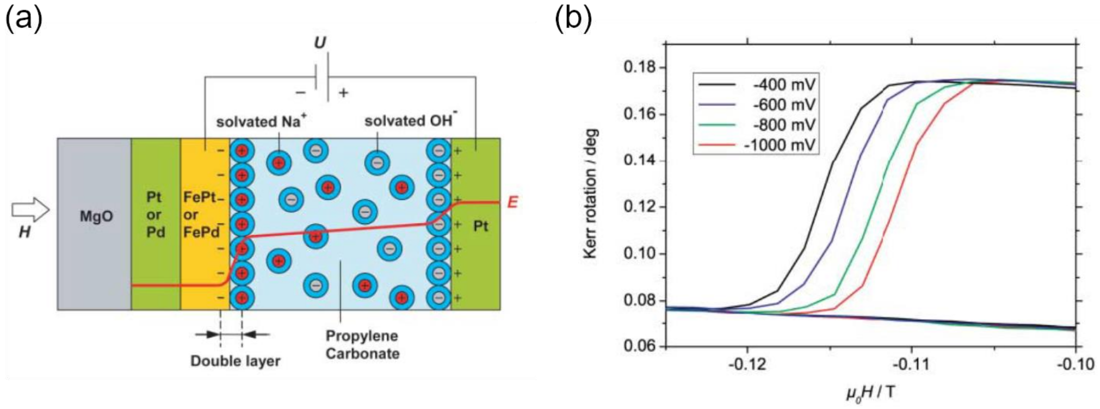

Figure. 3 Electric field control of magnetic anisotropy in thin ferromagnet reported by Weisheit[19]

(a) Schematic image of voltage application. (b) Voltage-induced interfacial anisotropy change. Its change was attributed to the voltage-induced electron state change and chemical property change of thin ferromagnet.

change is attributed to electron state change and/or chemical change. However, this demonstration attracts many researcher to this voltage-induced *interfacial* anisotropy change.

In 2009, Maruyama demonstrated voltage-induced *interfacial* anisotropy change in all-solid device. The device structure is MgO(001) substrate|MgO (10 nm)|Cr (10 nm)|Au (50 nm)|Fe (2-4 ML)|MgO (10 nm)|Polyimide (1,500 nm)|ITO (100 nm). Figure

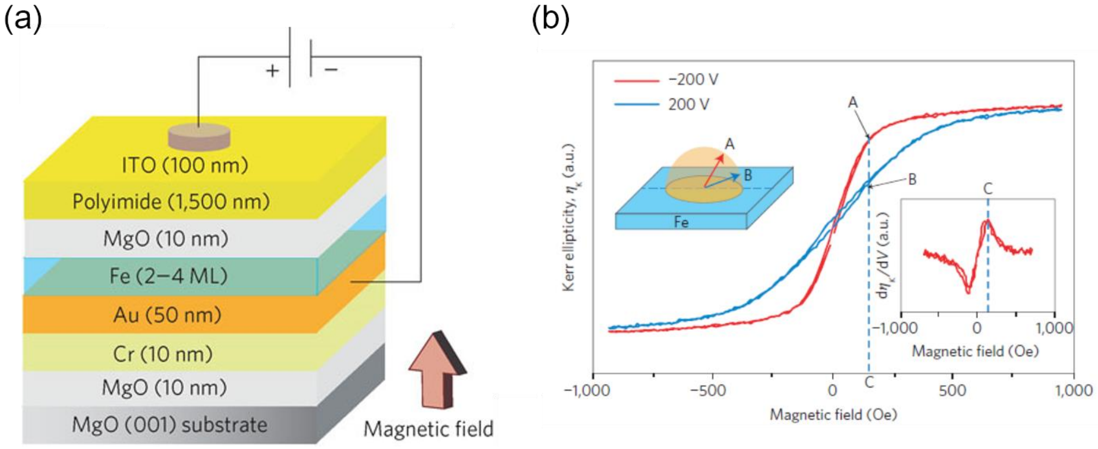

Figure. 4 Electric field control of interfacial magnetic anisotropy in all-solid thin ferromagnet reported by Maruyama[19]

(a) Schematic image of film structure and measurement setup for the voltage application. (b) Voltage-induced interfacial anisotropy change obtained. Its change was almost attributed to voltage-induced electron-state change.

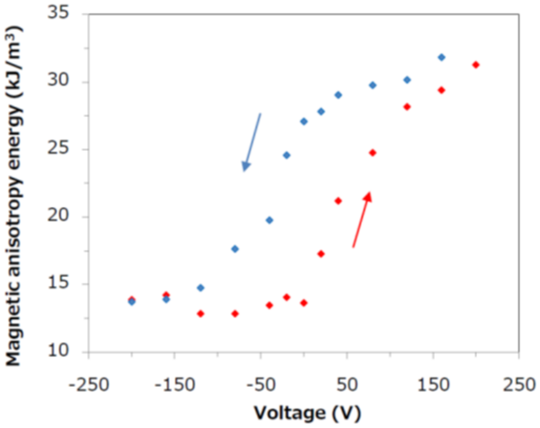

Figure. 5 Magnetic anisotropy energy as function of applied voltage reported by Maruyama[19]

Voltage sweep measurement shows hysteresis. This attributes to eh charge trapping in the MgO|Polyimide interface and/or chemical reaction.

4 (a) shows measurement set up and measurement geometry. They also measured voltage-induced *interfacial* anisotropy change by polar MOKE shown in Fig. 4 (b). Compared with ion liquid, applied electric field was reduced because of low dielectric constant of Polyimide, however, by using few monolayer ferromagnet, they succeeded in observing voltage induced *interfacial* anisotropy change. To discuss the magnitude of this voltage-induced *interfacial* anisotropy change, generally the voltage-induced anisotropy energy change, obtained by 1 V/nm and averaged by ferromagnetic thickness, is used. In this research, the obtained magnitude of voltage induced *interfacial* anisotropy change was almost about 90 fJ/Vm. In this letter, they also reported the possibility of voltage-induced magnetization direction switching in artificial multilayer by the numerical simulation shown. Figure 5 shows the result of magnetic anisotropy energy as function of voltage. The hysteresis is observed in the voltage sweep measurement. This may attribute to the charge-trapping in the MgO|Polyimide interface and/or chemical reaction of the ferromagnetic layer.

This voltage-induced *interfacial* anisotropy change was also observed in MTJ by Shiota in 2011[21], and it showed a possibility of practical application of this voltage-induced *interfacial* anisotropy change for magnetization control in MTJ. This voltage-induced *interfacial* anisotropy change can act on magnetization dynamics as voltage-induced torque. In 2012, by injecting pulse voltage (0.4 ns, e.g.), corresponds to the time of precession of magnetization dynamics, Shiota succeeded in switching of magnetization direction at room temperature[22]. Figure 6 (a) and (b) show the schematic diagram of magnetization dynamics for the voltage pulse of 0.4 ns and 0.8 ns. As shown in Fig. 6 (a) and (b), this switching is bistable. Figure 6 (c) and (d) shows the result of experimentally

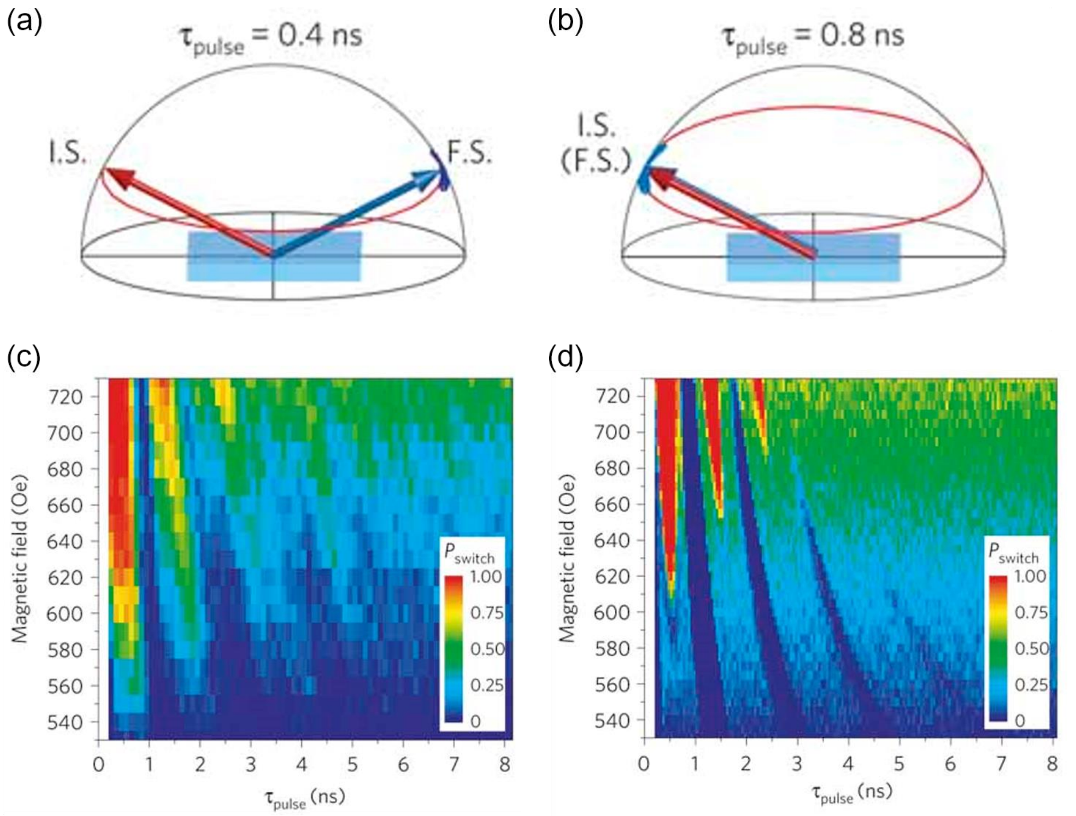

Figure. 6 Schematic image of pulse voltage induced magnetization switching in CoFe 0.7, the experimentally obtained switching probability mapping and switching probability mapping obtained by micro-spin calculation reported by Shiota[22].

(a), (b) Schematic image of magnetization switching. By injecting voltage pulse, equal to half of precession time, magnetization direction was switched (a). For the case of same length pulse injection as precession time, magnetization direction returns to initial direction. (c), (d) The mapping of switching probability obtained experimentally (a) and simulation of spin dynamics. The experimentally obtained result was almost perfectly reproduced.

obtained switching probability and switching probability obtained by the micro-spin model simulation. The oscillation period and phase were almost perfectly reproduced. This voltage switching can reduce the switching energy to 1/500th of that required for spin-transfer switching. This demonstration attracted a lot of attention, and some projects were started to apply this effect for MRAM. However, this pulse voltage-induced magnetization switching also has some problems; requirement of ultra-short pulse and magnitude of voltage induced *interfacial* anisotropy energy change. First, to produce ultra-short pulse, .transistor is needed for each MTJ, therefore, it may have the problem in integration. Second, the ferromagnetic layer thickness is limited to few monolayer, because of small magnitude of voltage-induced *interfacial* anisotropy energy change. To memorize information, it is important to reconcile a high thermal stability and high voltage-induced *interfacial* anisotropy change evenly. To reconcile them, huge voltage induced *interfacial* anisotropy change (~1000 fJ/Vm) is needed, however, the experimentally obtained magnitude of it was less than 100 fJ/Vm at that time.

In my research, first, I looked for new voltage-induced magnetic property change in an artificial multilayer (***interfacial* DMI**). Second, I designed an artificial multilayer and enhanced the observed new voltage-induced magnetic property change and voltage-induced interfacial anisotropy energy change.

1.3 Interfacial DMI

As a new voltage-induced magnetic property change, I was interested in an *interfacial* DMI, since DMI is the origin of multifferoic in Oxides. The DMI (DMI)[23,24] is an antisymmetric exchange interaction which plays a decisive role in the formation of exotic magnetic structures. It appears in the absence of spatial inversion symmetry incorporating a spin-orbit interaction, is expressed in the form of $H = \mathbf{D}_{12} \cdot (\mathbf{S}_1 \times \mathbf{S}_2)$ with the DM vector, $\mathbf{D}_{12}$. A coexistence of Heisenberg Exchange interaction and DMI selects the chirality to the magnetism mechanism and has an indispensable effect on it in various systems such as spin-glasses[25], cuprates[26], molecular magnets[27], multiferroic materials[28], and skyrmion lattices in chiral magnets[29], which is one of the smallest magnetic structure. In ultra-thin ferromagnet, this DMI was observed by Bode in 2007[30]. They studied spin structure of few monolayer Mn on W substrate by Spin-polarized scanning tunneling microscopy (SP-STM). In the scanning image, they observed an exotic oscillating signal.

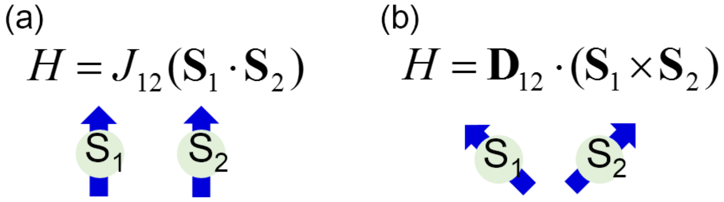

Figure. 7 Energy Hamiltonian of Heisenberg exchange interaction and DM interaction

(a) The energy Hamiltonian of Heisenberg exchange interaction. Adjacent spin pairs prefer to parallel or antiparallel, each other. (b) The energy Hamiltonian of DM interaction. Adjacent spin pairs prefer to cross, each other. In ferromagnet, if these interaction coexists, spin-structure becomes spiral under the existence of non-negligibly small DM interaction.

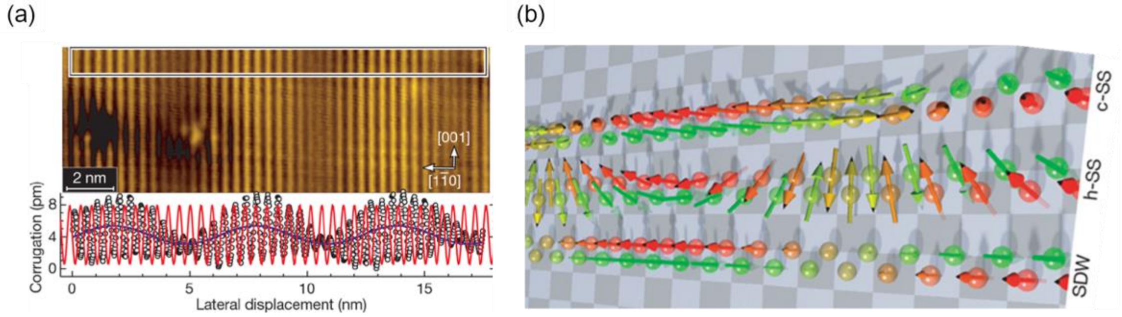

Figure. 8 The result of SP-STM and that of simulation reported by Bode.
(a) The result of SP-STM of Mn monolayer on W substrate (upper) and the averaged line section (lower). Two oscillation signal was observed in lower graph. (b) The results of simulation of a left-handed cycloidal spin-spiral (upper), helical spin-spiral (center) and spin density wave (lower).

By comparing its signal with simulation results of a spin density wave, a helical spin spiral and a left-handed cycloidal spin-spiral, they concluded the oscillating signal is a left-handed cycloidal spin spiral attributed to the DMI. The spatial inversion symmetry is broken on surface, therefore, it is called as *interfacial* DMI. After this observation of *interfacial* DMI, it had been observed in many magnetism systems, in whose film structure ultra-thin ferromagnetic layer (less than 2 nm) attached to the material with large spin-orbit interaction, such as W, Ir, Pt. In the following, I simply describe other techniques to observe and estimate *interfacial* DMI in the other magnetic structures.

The direct observation of *interfacial* DMI was firstly performed by spin-polarized electron energy loss spectroscopy (SPEELS) in W|Fe by Zakeri[31]. They characterized spin-wave property by SPEELS and observed *interfacial* DMI as resolve of degeneracy in spin waves shown in Fig. 9 (a) (see chapter 2 for the details of the relation between *interfacial* DMI and spin waves). The plots of spin-wave resonant frequency as a function of wave number obtained in W|Fe (2 ML) is shown in Fig. 9 (b)[32]. The clearer resolve of degeneracy of spin waves attributed to the *interfacial* DMI can be obtained in this relation. The *interfacial* DMI can also be observed in the other spin-wave measurement; Brillouin Light Scattering (BLS) in Pt|Co|AlOx, Pt|CoFeB|AlOx[33], Pt|Co|Ni|MgO[34] and Pt|$Ni_{80}Fe_{20}$|SiN[36]. The ferromagnetic layer thickness dependence[33] and the linear relation between Heisenberg exchange and *interfacial* Dzyaloshinskii-Moriya interaction[36] were reported. Spin-wave spectroscopy can also be performed by electric measurement by using micro-sided antennas[35]. By using this antenna method, *interfacial* DMI was also reported[37,38]. However, this measurement is strongly affected by the measurement set up, therefore, it is not suitable for the direct measurement of

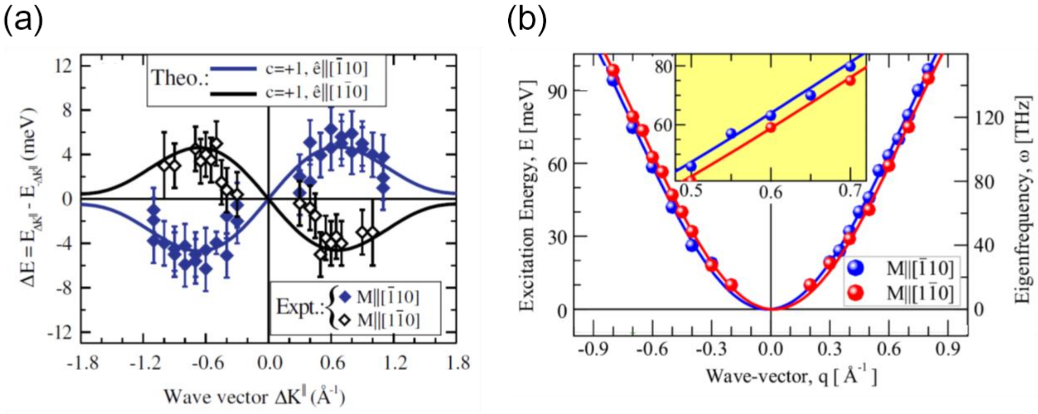

Figure. 9 The results of SPEELS reported by Zakeri[31,32].

(a) The result of SPEELS. The signal relates to the sign of wave vector and magnetization direction. The resolve of degeneracy, depending on the sign of wave vector and magnetization direction, was observed. (b) Experimentally obtained spin-wave resonant frequency as function of wave number. The clear resolve of degeneracy can be observed.

interfacial DMI.

The *interfacial* DMI has also been extensively investigated[39-43], especially in relation to current-driven magnetic domain wall motion, because *interfacial* DMI provides very high domain-wall velocity. In the existence of *interfacial* DMI, domain wall forms Neel domain wall shown in Fig. 10 (a) in one dimension ferromagnetic wire, and *interfacial* DMI are usually estimated by effective magnetic field. Figure 10 (b)

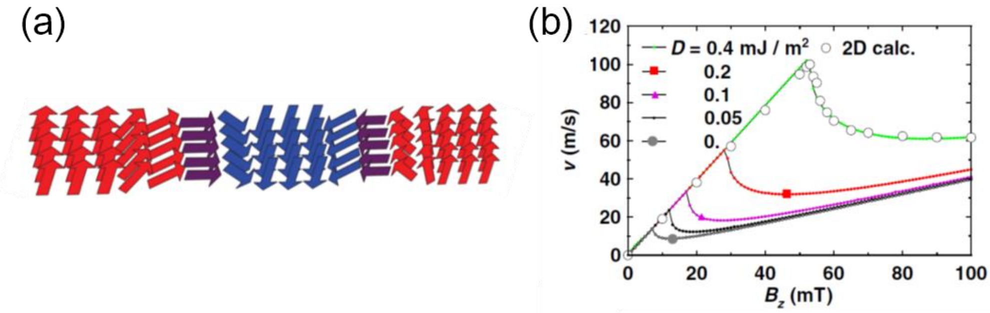

Figure. 10 The schematic image of Neel domain wall drawn by Ryu[40] and the fast domain wall motion reported by Thiaville[39].

(a) The Schematic image of Neel domain wall, that is, with their magnetization along with wire. The calculated velocity of domain walls for the case of two dimensional ferromagnetic wire. The peak position, depending on D constant, is called as walker field. Under walker field, the velocity of domain-wall motion linearly increase as increasing magnetic field.

shows the calculated relation[39] between D constant and the velocity of domain-wall. The peak position is called as Waller field, and under its field, the velocity of domain wall increase as increasing magnetic field, since it can keep Neel domain.

Skyrmion lattice is also attributed to the DMI. This skyrmion is one of the smallest magnetic order, and it is protected by topology. It has very exotic spin-structure, where spin oriented normal direction to the surface of sphere as shown in Fig. 11. Therefore, it is expected as one of the smallest memory cell, which may not be obtained in ferromagnetic cell because of the limit of super-paramagnet. The magnetic skyrmion was firstly observed in bulk material, such as $Fe_{1-x}Co_xSi$[46] and MnSi[47], in 2009. The skyrmion lattice was also observed in one-atomic-layer thickness Fe on the Ir (111)[49] attributed to the *interfacial* DMI. For the practical application, skyrmion race track memory, based on that of domain wall, was produced, for example. The nucleation and annihilation of skyrmions in artificial multilayer can be controlled by spin-polarized current[51] and voltage induced *interfacial* anisotropy change[52,53].

The origin of interfacial DMI is a spin-orbit interaction and broken spatial inversion symmetry on surface and/or interface. However, its detailed mechanism has been veiled. In the literature, the role of the proximity-induced spin polarization of Pt was highlighted[44]. However, Yang et al. used first-principle calculations to show that no direct correlation between *interfacial* DMI and proximity-induced magnetism in Pt exists[45].

The reported D constant is about 1.0 mJ/m^2 in various measurement. The enhancement of interfacial DMI energy is important for fast domain wall motion and stability of skyrmions, therefore many researcher still challenge to unveil and enhance interfacial DMI energy now.

As I introduced up to this point, *interfacial* DMI strongly acts on current spintronics research. Therefore, voltage modulation of *interfacial* DMI may open new aspect for the research of spin wave, domain wall and skyrmion, for example. However,

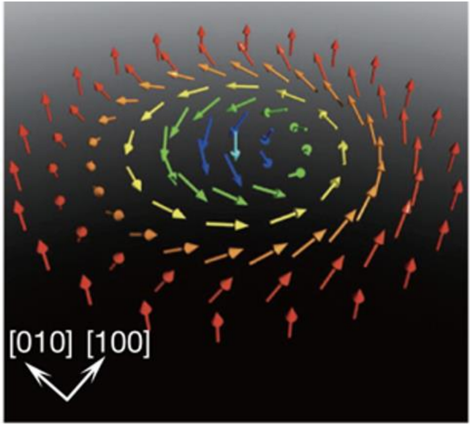

Figure. 11 Image of a skyrmion quasi-particle drawn by Yu[48].

the direct observation of voltage modulation of interfacial DMI has never been reported yet.

1.4 Purpose of this study

As mentioned in the last section, the voltage modulation of *interfacial* DMI has never been reported yet, however, it may be new milestone in the research of spintronics. Therefore, **the purpose of my research is voltage modulation of *interfacial* DMI in artificial multilayer**. After success of voltage modulation of interfacial DMI in artificial multilayer. I proposed new film structure to enhance its voltage modulation and succeeded in demonstrating the enhancement of voltage modulation of interfacial DMI in artificial multilayer by inserting one monolayer Pt into Fe|MgO interface, where voltage can be applied.

The influence caused by DMI attributes to the chirality, therefore, I have to study the chirality-dependent magnetic property. In my research, I focused on spin-wave system because of the following reason. First, the dynamics of spin waves is well known. Second, spin wave is one of the resonant state, therefore repetition of experiment is inferior to the measurement with domain walls. To study spin waves, I selected electrical measurement, since it is inferior to the optical measurement in terms of signal to noise ratio and resolution.

In the next chapter 2, first I describe the relation between spin waves and chirality. Then I will derive the spin-wave dispersion relation from the basic electromagnetism and Landau Lifshitz equation[54]. In the ferromagnetic films, three modes of spin waves exists; Magneto-static forward volume wave, Magneto-static backward volume wave and Magneto static surface spin waves. When magnetization of ferromagnet is normally-magnetized to the film surface, Magneto-static forward volume wave can be excited. When magnetization is magnetized to in-plane and propagation direction of spin waves is parallel to the magnetization, Magneto-static backward volume wave can be excited. If propagation direction is normal to the magnetization, Magneto-static surface spin waves can be excited. In this research, I selected Magneto-static surface spin waves because of the following two reason. First, because of the spatial inversion symmetry broken by the film interface, the difference between right-hand chirality and left-hand chirality can be induced. Second, spin-waves propagation length is larger than Magneto-static backward volume wave because of its faster group velocity than that of Magneto-static backward volume wave.

In chapter 3, film fabrication process and microfabrication process to fabricate spin-wave device is described.

In chapter 4, I describe voltage modulation of propagating spin waves in thin Fe film. Then, there was no report about the demonstration of voltage control of propagating spin waves. Therefore, this study was performed to investigate whether the signal intensity of voltage-modulation of propagating spin wave was detectably large. From the obtained voltage modulation signal, I elucidate the mechanism of voltage-modulation of propagating spin waves.

In chapter 5, I demonstrate the voltage modulation of *interfacial* DMI from the chirality-dependent voltage modulation signal in Au|Fe|MgO based artificial multilayer. From the thickness dependence of Fe, I discuss the contribution of surface localization property for the chirality dependent voltage effect.

In chapter 6, I designed new films structure and demonstrated the enhancement of voltage modulation of interfacial DMI. I also show the one of the example of practical application of voltage-induced interfacial DMI change; that is voltage nucleation and annihilation of skyrmion.

2.1 Spin wave

The spin wave is one of the excitation state of the group of spins. It is not only used as carrier in the field of magnonics because of low energy consumption in propagating information[55] but also used as prober to measure magnetic property. In Fig. 12 (a), the schematic image of Magnetostatic Surface Spin Wave (MSSW), used in this research, is shown. MSSWs can be excited by applying magnetic field to the film plane and propagate to normal direction of in-plane magnetic field direction. Each spin in spin waves precesses and the phase difference of each spin precession propagates with a paticular wave length. By using spin-wave, the magnetic anisotropy in *z*-direction can be measured in the in-plane magnetized film, since each spin precesses in *x*-*z*-plane. Another specially mentioned merit of spin wave is its chirality. In Fig. 1(b)-(e), the projection of Fig. 1 (a) onto *x*-*z* plane are shown for the following case; in the case of Fig. 12 (b) and ((c)), MSSWs propagate to + (−) x direction under positive magnetic field. The fig. 12 (d) and (e) show the case of negative magnetic field. As Figs 1(b) and 1(c) show, when the MSSWs propagate in the opposite direction under a magnetic field (+*y*), the sign of the vector product of adjacent spin, $(\mathbf{S}_1 \times \mathbf{S}_2)$, changes. When the external magnetic field

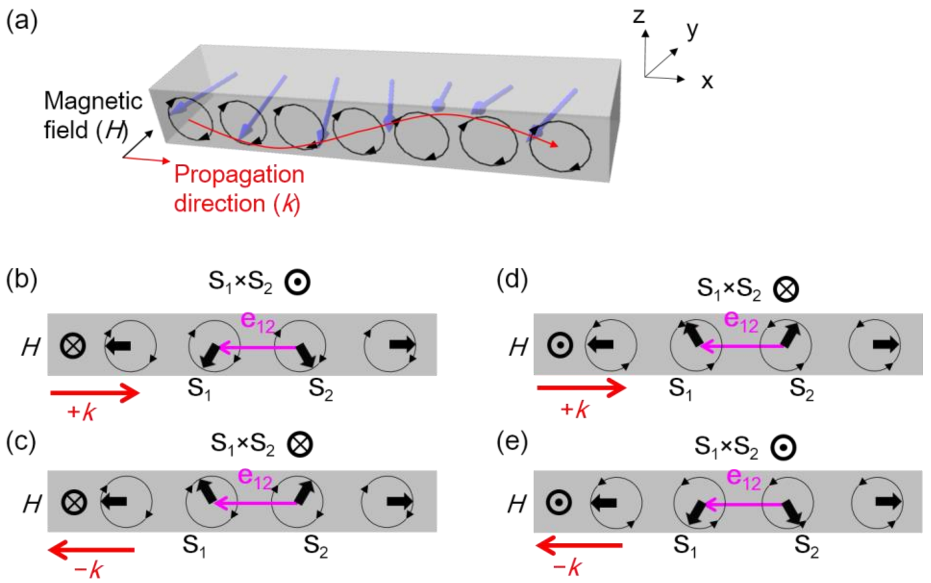

Figure. 12 Schematic of spin-wave propagation and relation between chirality and spin waves

(a) The MSSW propagates in the k-direction. (b)-(e) The projection of each spin-dynamic for the x-z plane. The vector product, $S_1 \times S_2$, is shown for all images.

is inverted to –y, its sign also changes as shown in Fig. 1(d) and 1(e). These interactions imply that the chirality of the MSSWs depends on the direction of spin-wave-propagation and magnetic field. By investigating such direction dependent properties, chirality-dependent magnetic properties, such as DMI, can be investigated. In the following, spin-wave motion equation is driven from the walker-equation[56]. Then, from the Expanded Landau-Lifshitz-equation, the dispersion relation of MSSW is derived.

2.1.1 Walker equation

In subsection, the Walker equation, used for describing magneto-static surface spin wave, is derived by following ref. 56 and ref. 57. Maxwell's equations for the material are expressed as,

$$\begin{cases} \nabla \times \mathbf{H} = \dfrac{\partial \mathbf{D}}{\partial t} + \mathbf{J} \\ \nabla \times \mathbf{E} = -\dfrac{\partial \mathbf{B}}{\partial t} \\ \nabla \cdot \mathbf{D} = \rho \\ \nabla \cdot \mathbf{B} = 0 \end{cases}, \tag{1}$$

where **H** is the magnetic field intensity, **D** is the electric flux density, **J** is the electric volume current density, **E** is the electric field intensity, **B** is the magnetic flux density and ρ is the electric volume charge density. In a material medium, the each field intensity becomes

$$\begin{cases} \mathbf{D} = \varepsilon_0 \mathbf{E} + \mathbf{P} \\ \mathbf{B} = \mu_0 (\mathbf{H} + \mathbf{M}) \end{cases}, \tag{2}$$

where ε_0 and μ_0 are the permittivity and permeability of free space, **P** is the electric dipole moment per unit volume and **M** is the magnetic dipole moment per unit volume. In the linear linear region for the first power of the field, the two instantaneous dipole moments can be expressed as

$$\begin{cases} \mathbf{P}(t) = \varepsilon_0 \bar{\chi}_\mathrm{e} \cdot \mathbf{E}(t) \\ \mathbf{M}(t) = \bar{\chi}_\mathrm{m} \cdot \mathbf{H}(t) \end{cases}, \tag{3}$$

where $\bar{\chi}_\mathrm{e}$ and $\bar{\chi}_\mathrm{m}$ are the electric and magnetic susceptibility tensor, respectively. Then it's convenient for the analysis of spin-wave dynamics to change them in the frequency domain. In the steady-state, two dipole moments can be written as

$$\begin{cases} \mathbf{P}(\omega) = \varepsilon_0 \bar{\chi}_{\mathrm{e}}(\omega) \cdot \mathbf{E}(\omega) \\ \mathbf{M}(\omega) = \bar{\chi}_{\mathrm{m}}(\omega) \cdot \mathbf{H}(\omega) \end{cases}, \tag{4}$$

By substituting them into two field intensity, they can be written as

$$\begin{cases} \mathbf{D} = \bar{\varepsilon} \cdot \mathbf{E} \\ \mathbf{B} = \bar{\mu} \cdot \mathbf{H} \end{cases}, \tag{5}$$

where the permittivity and permeability tensor are

$$\begin{cases} \bar{\boldsymbol{\varepsilon}} = \varepsilon_0 \left(\bar{\mathbf{I}} + \bar{\chi}_{\mathrm{e}} \right) \\ \bar{\boldsymbol{\mu}} = \mu_0 \left(\bar{\mathbf{I}} + \bar{\chi}_{\mathrm{m}} \right) \end{cases}, \tag{6}$$

and $\bar{\mathbf{I}}$ is the unit matrix. Here, we consider fields which depend on space and time with the form of $\exp(i\mathbf{k}\cdot\mathbf{r}-i\omega t)$, where k is the wave-number and ω is the frequency. Then Maxwell’s equations for the case for no source are expressed as

$$\begin{cases} \mathbf{k} \times \mathbf{H} = -\omega \bar{\varepsilon} \cdot \mathbf{E} \\ \mathbf{k} \times \mathbf{E} = \omega \bar{\mu} \cdot \mathbf{H} \\ \mathbf{k} \cdot \mathbf{D} = 0 \\ \mathbf{k} \cdot \mathbf{B} = 0 \end{cases} \tag{7}$$

It is convenient to define the antisymmetric matrix $\bar{\mathbf{k}}$ such that

$$\bar{\mathbf{k}} \equiv \mathbf{k} \times \mathbf{I} = \begin{bmatrix} 0 & -k_z & k_y \\ k_z & 0 & -k_x \\ -k_y & k_x & 0 \end{bmatrix}. \tag{8}$$

This matrix has the such good property as $\mathbf{k} \times \mathbf{A} = \bar{\mathbf{k}} \cdot \mathbf{A}$, where **A** is an arbitrary unit. This notation allows us to write Maxwell equation as

$$\begin{cases} \bar{\mathbf{k}} \cdot \mathbf{H} = -\omega \bar{\varepsilon} \cdot \mathbf{E} \\ \bar{\mathbf{k}} \cdot \mathbf{E} = \omega \bar{\mu} \cdot \mathbf{H} \end{cases}. \tag{9}$$

By multiplying $\bar{\mathbf{k}} \cdot \bar{\boldsymbol{\varepsilon}}^{-1}$ from the left for the upper equation and substituting, we can construct the following equation,

$$\left[\bar{\mathbf{k}} \cdot \bar{\boldsymbol{\varepsilon}}^{-1} \cdot \bar{\mathbf{k}} + \omega^2 \bar{\boldsymbol{\mu}} \right] \cdot \mathbf{H} = 0, \tag{10}$$

Similar equation can be also constructed as following for **E**

$$\left[\bar{\mathbf{k}} \cdot \bar{\boldsymbol{\mu}}^{-1} \cdot \bar{\mathbf{k}} + \omega^2 \bar{\boldsymbol{\varepsilon}} \right] \cdot \mathbf{E} = 0. \tag{11}$$

For the non-trivial solution, the determinants in Eq. (10) and (11) must vanish, therefore, the following equations are needed,

$$\begin{gathered}\det\left[\overline{\mathbf{k}}\cdot\overline{\boldsymbol{\mu}}^{-1}\cdot\overline{\mathbf{k}}+\omega^2\overline{\boldsymbol{\varepsilon}}\right]=0\\ \det\left[\overline{\mathbf{k}}\cdot\overline{\boldsymbol{\varepsilon}}^{-1}\cdot\overline{\mathbf{k}}+\omega^2\overline{\boldsymbol{\mu}}\right]=0\end{gathered}. \tag{12}$$

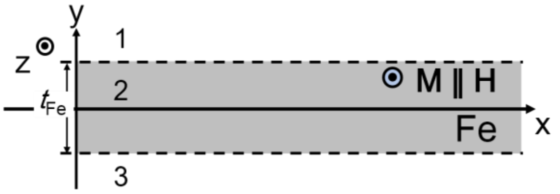

Figure. 13 Geometry for the MSSW analysis. The magnetization is saturated to *z* axis direction and spin waves propagate to the *x* axis direction

These equations select the relationships between ω and *k* for the plane wave and resulting function ω(k) is called as dispersion relation. Here, we consider the magneto-static mode, where the parts of Maxwell's equations are written as following,

$$\begin{cases}\nabla\times\mathbf{H}=0\\ \nabla\cdot\mathbf{B}=0\end{cases}. \tag{13}$$

Then, we consider the Fe thin film magnetized to *z* axis by applied external magnetic field to *z* axis as shown in Fig. 2. We consider the case of the magnetization is almost parallel to z axis, however, it also has the *x* and *y* component oscillating with frequency ω. In its situation, magnetic field also oscillate with frequency ω. Then magnetic dipole and magnetic field can be expressed as following,

$$\begin{cases}\mathbf{M}=M_0\hat{\mathrm{z}}+\mathbf{m}\mathrm{e}^{\text{-}\mathrm{i}\omega t}\\ \mathbf{H}=H_0\hat{\mathrm{z}}+\mathbf{h}\mathrm{e}^{\text{-}\mathrm{i}\omega t}\end{cases}, \tag{14}$$

where **m** and **h** are the oscillating component for magnetic dipole and magnetic field. By substituting them to the Landau-Lifshitz equation^{54}, the following equation is obtained,

$$\frac{d\left(M_0\hat{\mathrm{z}}+\mathbf{m}\mathrm{e}^{\text{-}\mathrm{i}\omega t}\right)}{dt}=-\gamma\mu_0\left(\left(M_0\hat{\mathrm{z}}+\mathbf{m}\mathrm{e}^{\text{-}\mathrm{i}\omega t}\right)\times\left(H_0\hat{\mathrm{z}}+\mathbf{h}\mathrm{e}^{\text{-}\mathrm{i}\omega t}\right)\right),$$

$$-i\omega\begin{pmatrix}m_x\\ m_y\end{pmatrix}=\omega_{\mathrm{M}}\begin{pmatrix}-h_y\\ h_x\end{pmatrix}+\omega_0\begin{pmatrix}-m_y\\ m_x\end{pmatrix}, \tag{15}$$

where $\omega_{\mathrm{M}}=\gamma\mu_0 M_0$ and $\omega_0=\gamma\mu_0 H_0$. Then magnetic susceptibility tensor can be identified as following,

$$\mathbf{m}=\overline{\chi}\cdot\mathbf{h}, \tag{16}$$

where the magnetic susceptibility and their component χ and κ is given by

$$\bar{\chi} = \begin{bmatrix} \chi & -i\kappa \\ i\kappa & \chi \end{bmatrix}, \tag{17}$$

and

$$\chi = \frac{\omega_{\mathrm{M}}\omega_0}{\omega_0{}^2 - \omega^2}, \kappa = \frac{\omega_{\mathrm{M}}\omega}{\omega_0{}^2 - \omega^2}. \tag{18}$$

By using this magnetic susceptibility, the total magnetic susceptibility tensor can be described as following,

$$\bar{\mu} = \mu_0\left(\bar{\mathbf{I}} + \bar{\chi}\right) = \begin{bmatrix} 1+\chi & -i\kappa & 0 \\ i\kappa & 1+\chi & 0 \\ 0 & 0 & 1 \end{bmatrix}. \tag{19}$$

The oscillating component of magnetic field and magnetic dipole should also allow Eq. (13), following equation is given

$$\begin{cases} \nabla \times \mathbf{h} = 0 \\ \nabla \cdot \mathbf{b} = \nabla \cdot \left(\bar{\mu} \cdot \mathbf{h}\right) = 0 \end{cases}. \tag{20}$$

Here, the magnetic field **h** can be written by the scalar potential ψ as following,

$$\mathbf{h} = -\nabla\psi. \tag{21}$$

By the combination of eq. (21) and eq. (20), we can obtain following equation,

$$\left(1+\chi\right)\left[\frac{\partial^2\psi}{\partial x^2} + \frac{\partial^2\psi}{\partial y^2}\right] + \frac{\partial^2\psi}{\partial z^2} = 0. \tag{22}$$

This equation is called as Walker equation and by using this equation with some boundary condition of films, we can calculate the dispersion relation of MSSW without any magnetic anisotropy.

2.1.2 Dispersion relation of MSSW

In this subsection, the dispersion relation for the magneto-static surface spin wave is derived. In the region 1 and 3 in Fig. 13, the wave-numbers for *x* and *y* is same, on the other hand, in the region 2, the wave-numbers for *x* and *y* is the different. Here, we prepare wave-number k_1 in the region 1 and 3 and k_{x} (k_{y}) for the *x*(*y*) axis in the region 2. Then, the scalar potential can be prepared as

$$\psi_{1,3} = \psi_{1,3}\mathrm{e}^{\mathrm{i}\nu k_1 x \mp k_1 y} \text{ (in the region 1 and 3)} \tag{23}$$

$$\psi_2 = \psi_2\mathrm{e}^{\mathrm{i}\nu k_x x \mp k_y y} \text{ (in the region 2),} \tag{24}$$

where ψ (ψ_2) is the scalar potential in the region 1 and 3 (2) and *v* means propagation direction; that is, when spin waves propagate to + (−) x direction, $\nu = +1$ (−1). In the Fe thin film, there are shape anisotropy, crystalline anisotropy and *interfacial* magnetic anisotropy, therefore, it's not isotropic. However, for the simple calculation, we think it isotropic. Then we can make $k_{\mathrm{x}} = k_{\mathrm{y}}$ in eq. (24). (More correct analysis for the relation between k_{x} and k_{y} is written in appendix 1) Then the walker equation for the scalar potential in the region 2 is written as following,

$$(1+\chi)\left(k_x{}^2 + k_y{}^2\right) = 0 \tag{25}$$

One possible solution for this is $1+\chi=0$, however, this only occurs for one specific frequency, therefore $k_x{}^2 = -k_y{}^2$ is needed. Here, we think magneto-static surface wave, which propagates in x axis, so k_{y} must be imaginary. Hence, ψ_2 will not be oscillatory but must consist of growing and decaying exponentials. Therefore, we can replace eq. (24) as following,

$$\psi_2 = \left(a\mathrm{e}^{k_x y} + b\mathrm{e}^{-k_x y}\right)\mathrm{e}^{\mathrm{i}\nu k_x x}, \tag{26}$$

Then we apply the boundary conditions at y = ±t_{Fe}/2 for the scalar potential.

$$\psi_1 \mathrm{e}^{-\mathrm{k}_1 t_{\mathrm{Fe}}/2} = \left(a\mathrm{e}^{k_1 t_{\mathrm{Fe}}/2} + b\mathrm{e}^{-k_1 t_{\mathrm{Fe}}/2}\right), \tag{27}$$

$$\psi_3 \mathrm{e}^{-\mathrm{k}_1 t_{\mathrm{Fe}}/2} = \left(a\mathrm{e}^{-k_1 t_{\mathrm{Fe}}/2} + b\mathrm{e}^{k_1 t_{\mathrm{Fe}}/2}\right), \tag{28}$$

where $k_1 = k_{\mathrm{x}}$ is needed for x direction-boundary condition. The magnetic flux density for the y axis mast be continuous. The magnetic flux density for y axis is given as following,

$$b_{\mathrm{y}(1)} = \nabla_y \psi_1 \quad \text{(in the region 1)}, \tag{29}$$

$$b_{y(2)} = i\kappa \nabla_{\mathrm{x}} \psi + (1+\chi)\nabla_{\mathrm{y}} \psi \quad \text{(in the region 2)}. \tag{30}$$

Then the needed conditions for the magnetic flux density is obtained as following,

$$\psi_1 \mathrm{e}^{-\mathrm{k}_1 t_{\mathrm{Fe}}/2} = \kappa\nu\left(a\mathrm{e}^{k_1 t_{\mathrm{Fe}}/2} + b\mathrm{e}^{-k_1 t_{\mathrm{Fe}}/2}\right) - (1+\chi)\left(a\mathrm{e}^{k_1 t_{\mathrm{Fe}}/2} - b\mathrm{e}^{-k_1 t_{\mathrm{Fe}}/2}\right), \tag{31}$$

$$\psi_3 \mathrm{e}^{\mathrm{k}_1 t_{\mathrm{Fe}}/2} = -\kappa\nu\left(a\mathrm{e}^{-k_1 t_{\mathrm{Fe}}/2} + b\mathrm{e}^{k_1 t_{\mathrm{Fe}}/2}\right) + (1+\chi)\left(a\mathrm{e}^{-k_1 t_{\mathrm{Fe}}/2} - b\mathrm{e}^{k_1 t_{\mathrm{Fe}}/2}\right). \tag{32}$$

To obtain a trivial solution from these 4 boundary conditions, the determinant of following matrix must be zero as following,

$$\det\begin{bmatrix}(\chi+2-\nu\kappa)\mathrm{e}^{k_1 t_{\mathrm{Fe}}/2} & -(\chi+\nu\kappa)e^{-k_1 t_{Fe}/2}\\ -(\chi-\nu\kappa)e^{-k_1 t_{Fe}/2} & (\chi+2+\nu\kappa)\mathrm{e}^{k_1 t_{\mathrm{Fe}}/2}\end{bmatrix}=0\,. \tag{33}$$

Then, by using eq. (18), following basic dispersion relation of MSSW is obtained,

$$\omega^2=\omega_0(\omega_0+\omega_{\mathrm{M}})+\frac{{\omega_{\mathrm{M}}}^2}{4}\left[1-e^{-2k_1 t_{\mathrm{Fe}}}\right]. \tag{34}$$

By using Eq. (33), the scalar potential for each region can be obtained as following,

$$\psi_1=a\left(e^{k_1 t_{\mathrm{Fe}}}+p(\nu)\right)\mathrm{e}^{\mathrm{i}\nu k_1 x-k_1 y}\ \text{(in the region 1)} \tag{35}$$

$$\psi_2=a\left(e^{k_1 y/2}+p(\nu)e^{-k_1 y/2}\right)\mathrm{e}^{\mathrm{i}\nu k_1 x}\ \text{(in the region 2),} \tag{36}$$

$$\psi_3=a\left(1+p(\nu)e^{k_1 t_{\mathrm{Fe}}}\right)\mathrm{e}^{\mathrm{i}\nu k_1 x+k_1 y}\ \text{(in the region 3),} \tag{37}$$

where $p(\nu)$ satisfies the following relation,

$$p(\nu)=b/a=\frac{\chi-\nu\kappa}{\chi+2+\nu\kappa}e^{k_1 t_{\mathrm{Fe}}}=\frac{\chi+2-\nu\kappa}{\chi+\nu\kappa}e^{-k_1 t_{\mathrm{Fe}}} \tag{38}$$

and *a* is an arbitrary amplitude factor. Then the scalar potentials for each region are calculated shown in Fig. 14 (c)-(d), where $\omega_0/\omega_{\mathrm{M}}$ is 0.02 and $k_1 t_{\mathrm{Fe}}$ is 10 in (c) ($k_1 t_{\mathrm{Fe}}$ is 1 in (d) and $k_1 t_{\mathrm{Fe}}$ is 0.02 in (e)). It is important to note that spin waves propagating to opposite direction localize in different surface as shown in Fig. 14 (a) and (b). Because of this reason, these spin waves are named as surface wave. When the external magnetic field is switched and magnetization is also switched, localization properties for each spin waves is also switched. This localization properties is dominated by the relation between spin-wave wave number k_1 and thickness of ferromagnetic layer t_{Fe}. When $k_1 t_{\mathrm{Fe}}$ is same level as 1 or greater than 1, two spin waves propagating opposite direction strongly localize in top and bottom surfaces. However, when $k_1 t_{\mathrm{Fe}}$ is much smaller than 1, then two spin waves propagating opposite direction doesn't localize much.

The dispersion relation of the MSSW becomes different formula for the single crystalline Fe because of anisotropies. When ferromagnet has cubic and uniaxial anisotropy, its expanded dispersion relation is derived as following[60],

$$\omega^2=\left[\omega_0+\omega_{\mathrm{M}}-\omega_{\mathrm{M}}\frac{k_1 t_{\mathrm{Fe}}}{2}-2\gamma(H_{\mathrm{a}}-H_{\mathrm{u}})\right]\left(\omega_0+\omega_{\mathrm{M}}\frac{k_1 t_{\mathrm{Fe}}}{2}-2\gamma H_{\mathrm{a}}\right), \tag{39}$$

where magnetization is parallel to the external magnetic field, MSSW-configuration and only first-mode excitation are considered, H_{a} is four-fold magnetic anisotropy field and H_{u} is uniaxial anisotropy field. If the $k_1 t_{\mathrm{Fe}}$ is much smaller than 1, the following equation is given,

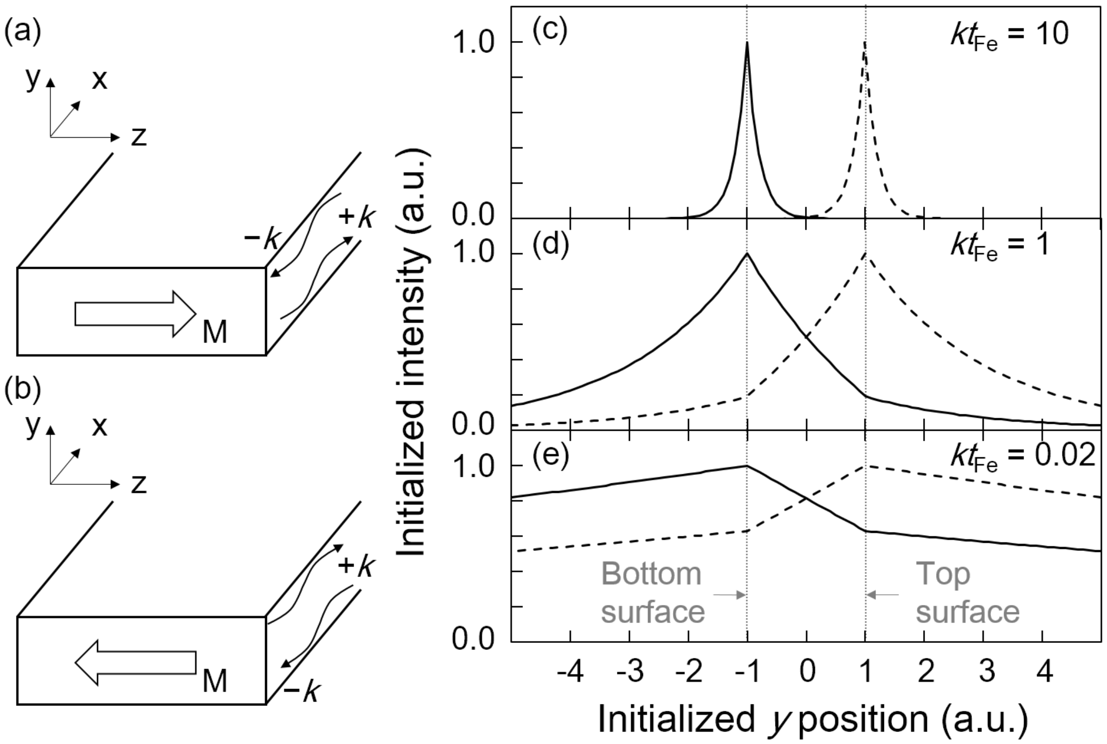

Figure. 14 Localization properties of MSSWs

(a) MSSWs in the case where magnetization is aligned to z direction. Spin wave propagating to +x (−x) direction localizes to bottom (Top) interface.(b) MSSWs in the case where magnetization is aligned to −z direction. Localization property of each spin wave switches. (c) - (d) Calculated localization properties for kt_{Fe} = 10 in (c) (kt_{Fe} = 1 in (d) and kt_{Fe} = 0.02 in (e)) and ω_0/ω_M = 0.02. The horizontal axis is the initialized y position ($2y/t_{\mathrm{Fe}}$) The localization property strongly depends on part of the $\exp(2k_1t_{\mathrm{Fe}})$. For the case of $k_1t_{\mathrm{Fe}} > 1$, spin waves localize in the top or bottom surface, on the other hand, for the case of $k_1t_{\mathrm{Fe}} << 1$, spin waves don't localize in top or bottom surface. Therefore, for the case of thin film, we don't need to consider the contribution of localization property

$$\omega^2 = [\omega_0 - 2\gamma H_{\mathrm{a}}][\omega_0 + \omega_{\mathrm{M}} - 2\gamma(H_{\mathrm{a}} - H_{\mathrm{u}})] + \omega_{\mathrm{M}}(\omega_{\mathrm{M}} - 2\gamma H_{\mathrm{u}})\frac{\mathrm{k}_1\mathrm{t}_{\mathrm{Fe}}}{2}, \tag{40}$$

where the part of k_1t_{Fe} comes from the $\exp(-2k_1t_{\mathrm{Fe}})$. Therefore, without approximation, the following equation can be obtained,

$$\omega^2 = [\omega_0 - 2\gamma H_{\mathrm{a}}][\omega_0 + \omega_{\mathrm{M}} - 2\gamma(H_{\mathrm{a}} - H_{\mathrm{u}})] + \omega_{\mathrm{M}}(\omega_{\mathrm{M}} - 2\gamma H_{\mathrm{u}})\frac{1 - \mathrm{e}^{-2\mathrm{k}_1\mathrm{t}_{\mathrm{Fe}}}}{4}. \tag{41}$$

Here, by including DMI term and changing eq. (41) to the frequency range, we obtain the following equation[61],

$$f = -\frac{\gamma}{2\pi}\sqrt{\left(|H_0|+H_\mathrm{a}\right)\left(|H_0|+M_0+H_\mathrm{a}-H_\mathrm{u}\right)+\frac{M_\mathrm{S}}{4}\left(M_\mathrm{S}-H_\mathrm{u}\right)\left(1-\exp\left(-2|k_1|t_\mathrm{Fe}\right)\right)} \mp \frac{\gamma}{\pi M_0}Dk, \quad (42)$$

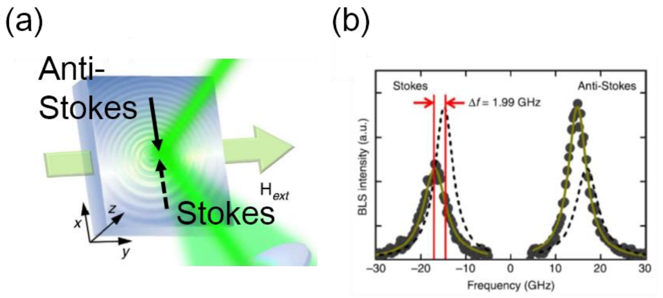

Figure. 15 (a) Schematic image of BLS measurement and typical signals of BLS in Pt|Co (1.2 nm)|AlOx reported by Cho[33].

where, D is the absolute value of **D** vector. As mentioned in the sub-section 2.1, DMI parameter D depends on the spin-wave propagation direction. This DMI term can induce the propagation-direction dependent frequency shift, therefore by measuring propagation-direction dependent frequency shift in thin film, the *interfacial* DMI can be observed. In the measurement of BLS, interfacial DMI can be estimated by estimating this propagation-direction dependent frequency shift. As shown in Fig. 15. In the following section 4-6, spin-wave spectra were analyzed by using this equation.

Chapter 3. Experimental method

In this chapter, the experimental methods are shown. The main topics of this chapter consist of the following two topics; film fabrication and microfabrication. The detailed film structure and measurement circuits are explained in each chapter.

3.1 Film fabrication

The artificial multilayers, used in this study, were almost fabricated by using Molecular Beam Epitaxy (MBE) method in Suzuki Lab. as shown in Fig. 16 (a). By using MBE method, epitaxially grown artificial multilayer, controlled in angstrom order, can be prepared. The schematic image of the artificial multilayer is shown in Fig. 16 (b). On an MgO (001) substrate, MgO (10 nm)|Cr (5 nm)|Au (50 nm)|Fe (5 nm)|MgO (10 nm)|SiO_2 (5 nm) was deposited. Before depositing materials on an MgO substrate, it was annealed at 800 °C in 10 min. to obtain growth surface. First MgO is used for preventing impurity of the substrate, such as carbon, from coming the other layer. Cr and Au layers were prepared as the buffer layer for an Fe layer. The final MgO layer was prepared as insulating layer to applying voltage. Because of pin-hole of MgO layer, it is not enough

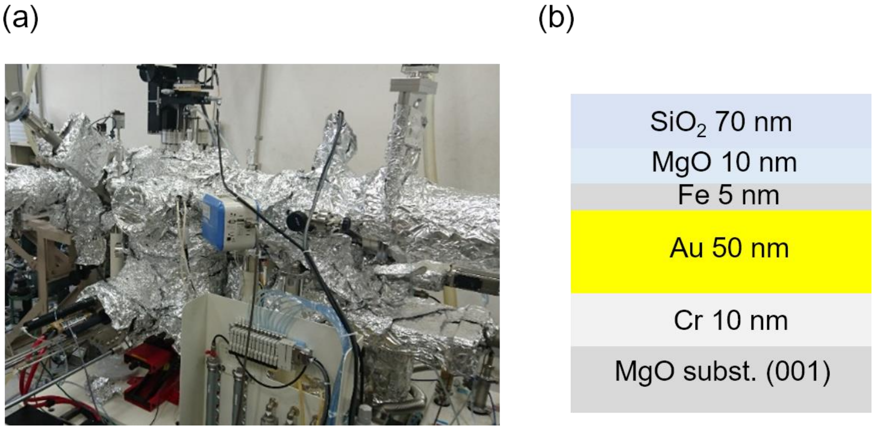

Figure. 16 Molecular Beam epitaxial chamber and schematic image of artificial multilayer

(a) The growth chamber of MBE. Base pressure is 10^{-8} Pa order. MBE growth chamber has a Reflected High Energy Electron Diffraction (RHEED) and two electron beam gun (3 kW and 6 kW). (b) The schematic image of artificial multilayer. Spin waves propagate in Fe-5-nm. By microfabrication, top electrode is prepared on SiO_2 and by applying voltage between top electrode and bottom electrode, which is Fe here, *interfacial* anisotropy and interfacial DMI can be modulated.

as barrier, therefore additional SiO_2 layer was sputter deposited. By applying electric field into MgO|SiO_2 layers, *interfacial* anisotropy and *interfacial* DMI in Fe|MgO interface can be modulated.

3.2 Microfabrication

To measure the certain spin wave by electrical measurement, microfabrication is needed. In this section, the detailed microfabrication-process is written. Figure 17 shows the schematic image of the spin-wave devices used in this research. This spin-wave device consists of Fe wire, two antennas and intermediated gate on the insulating layer, which consists of MgO and SiO_2. The antenna has a signal line sandwiched by two ground lines and is shorted at the end. The width of signal line, ground lines, and their gap were designed to be 2 μm, 1 μm, and 1 μm, respectively. This spin-wave device was fabricated by 6 times Electron Beam (EB.) Lithography, 2 times Ar^+ ion milling and 3 times lift-off process.

(1)

12 cross patterns for each device were prepared for the following EB. Lithography. The pattern shown in Fig. 18 (a) is used. After drawing and development of resist, Cr(5 nm)|Au(100 nm) was deposited to the pattern.

(2)

The wire pattern, as shown in Fig. 18 (b), for each device was drawn by the EB.

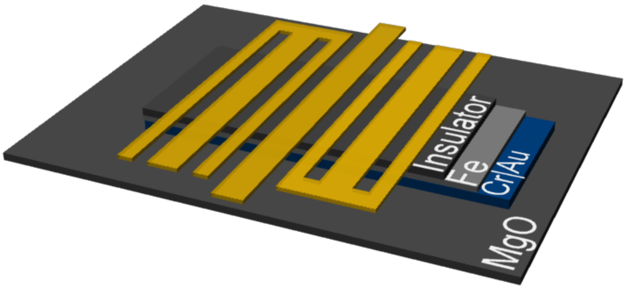

Figure. 17 Spin-wave device

Spin-wave device consists of an Fe wire, two antennas and intermediated gate on the insulating layer, which consist of MgO and SiO_2. The antenna has signal line sandwiched by two ground line and it is short circuit. The width of signal line, ground lines, and their gap were designed to be 2 μm, 1 μm, and 1 μm, respectively.

Lithography. After development of resist, the film was etched to the bottom MgO layer by using Ar^+ ion milling. After milling and before removing resist, SiO_2 20 nm was sputter deposited to protect the side from oxidization of the Fe wire and from the electric contact between Fe wire and antennas. Thicker SiO_2 deposition should be avoided, because it becomes impossible to remove the resist.

(3)

Without resist, SiO_2 65 nm was sputter deposited to eliminate the exposure of the Fe wire.

(4)

When the voltage was applied to this sample, the sample was broken from the edge of Fe wire. To enhance the endurance for the voltage, additional SiO_2 20 nm was sputter deposited, by using the pattern in Fig. 18 (c), which is very narrow wire patterns span over Fe wire edge and substrate.

(5)

To applying voltage for film perpendicular direction, the conduction path to the bottom electrode is needed. In this process, Fig. 18 (d) was used and the film was etched to the Fe or Au layer.

(6)

The antennas and intermediated gate were fabricated by using patterns shown in Fig. 18 (e) and (f). Here, the patterns are divided to two pattern. The pattern in Fig. 18 (e) is relatively large and is just used to put on the needle of prober, so rough drawing in EB. Lithography is enough. On the other hand, the pattern in Fig. 18 (f) needs very delicate drawing, because they directly depend on spin-wave excitation.

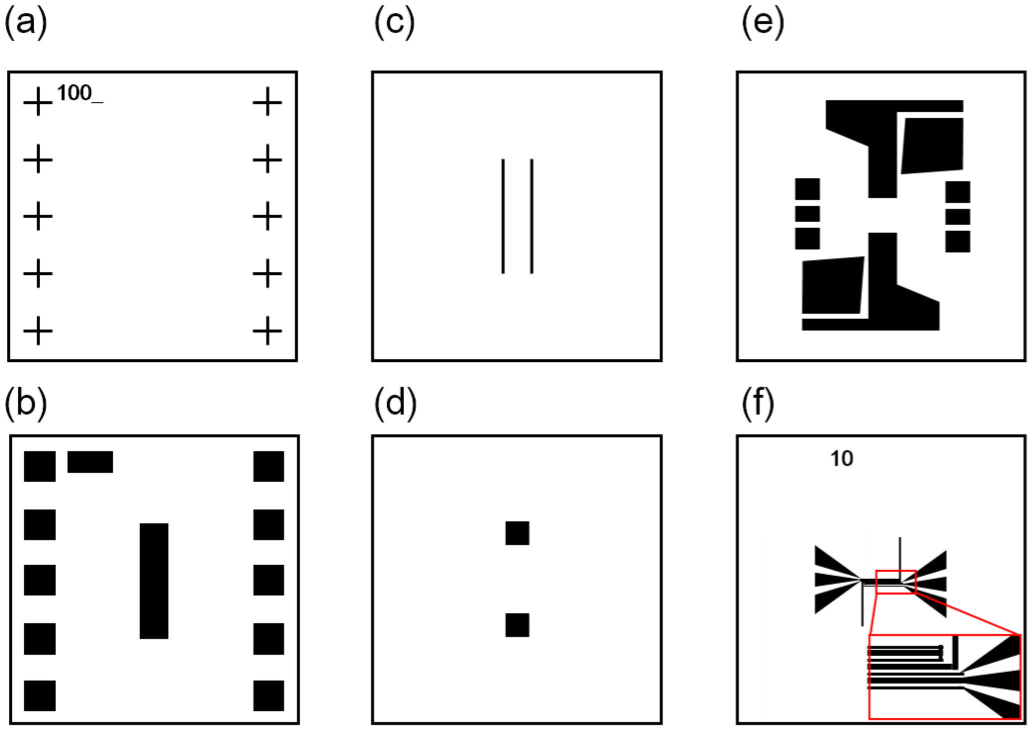

Figure. 18 The patterns for each process

(a)-(f) The patterns for each process in EB. Lithography. The inset in (f) is an expanded image of surrounded area. Antennas is shorted at the end and consist of a signal line and two ground lines. The width of signal, ground and gap between them are, 2 μm, 1 μm and 1 μm, respectively.

Chapter 4. Results and discussion 1 (Voltage modulation of propagating spin waves in Fe thin film)

As mentioned above, spin-wave spectroscopy is useful technique to measure some magnetic properties. If we can control propagating spin waves by external voltage, we can investigate not only voltage induced anisotropy change, but also voltage induced DMI change. The electric modulation of propagating spin waves in ferromagnetic metallic film were only achieved by using electric current application[58] and spin-transfer[59] but voltage modulation of propagating spin waves in artificial multilayer has never been reported yet. For this reason, first of all, I focused on measuring voltage modulation signal of propagating spin waves in Fe thin film on Au buffer layer to investigate whether the voltage modulation signal of propagating spin waves is detectably large. The main purpose of this chapter is to observe the voltage modulation signal of propagating spin waves in a thin Fe wire and to build the analysis method of the voltage modulation signal. The main results were published as Journal of applied physics **117**, 17A905 (2015)

4.1 Material and methods

4.1.1 Sample fabrication

The artificial multilayer was grown on single crystalline MgO (001) substrate by using molecular beam epitaxy method in Suzuki lab. The film structure of the MgO (001) substrate|MgO (10 nm)|Cr (5 nm)|Au (50 nm)|Fe (5 nm)|MgO (10 nm)|Cr (5 nm)|Au (10

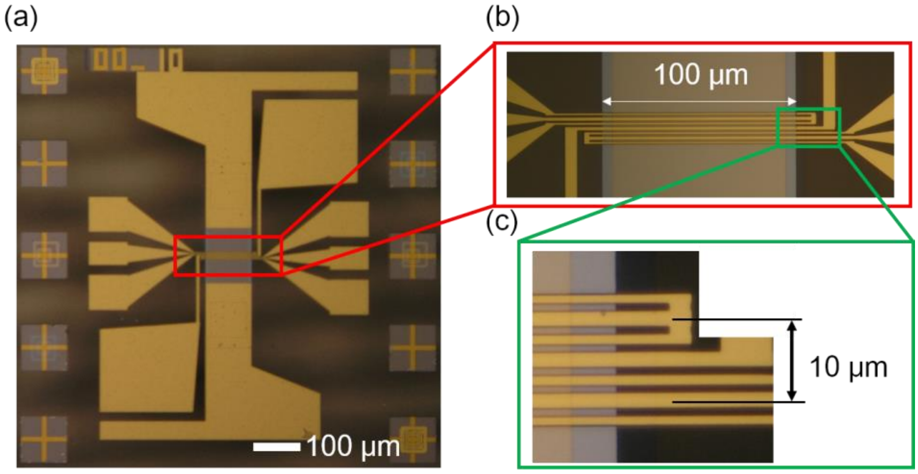

Figure. 19 Picture of spin-wave device

(a) Over view of the device (b) and (c) expanded image of surrounded area

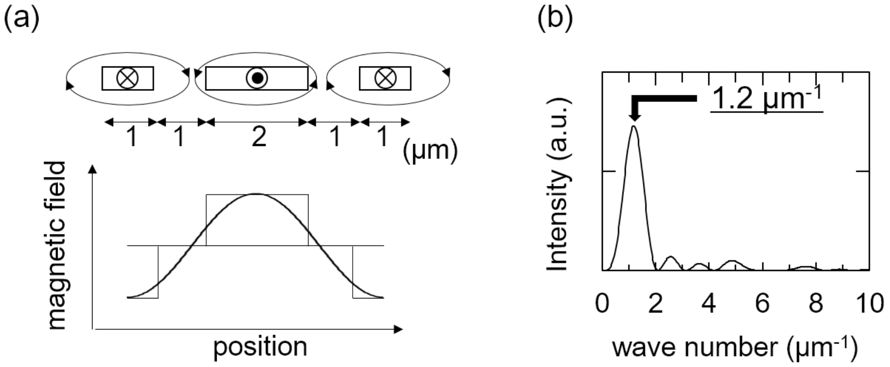

Figure. 20 Spatial distribution of magnetic field
(a) Spatial distribution of magnetic field, (b) The result of Fourier transformation of the spatial distribution of the magnetic fields

nm) was prepared under a vacuum level of < 4 × 10^{-7} Pa. Each layer was deposited by checking Reflected High Energy Electron Diffraction (RHEED) pattern. By the same microfabrication process as sub section 3.2, spin-wave devices were fabricated as shown in Fig. 19. Here the wire has rectangular shape (100 μm × 400 μm) with an edge line parallel to the Fe (100) direction. The spin-wave propagation length is 10 μm. The selected wave number by this comb-shaped antenna can be calculated by Fourier transformation of the magnetic fields produced by the electric current flowing in antennas[62]. The schematic image of magnetic field, produced by current in antenna, is shown in Fig. 8 (a). The schematic image of the spatial distribution of the magnetic fields is also shown in Fig. 20 (a). Here, Fourier transformation gives us the selected wave number by the antenna as shown in Fig. 20 (b). The main peak is 1.2 μm^{-1} and some sub peaks are also obtained.

4.1.2 Measurement

In this sub section, the detailed measurement circuit is shown. Generally, for the spin-wave spectroscopy, Vector Network Analyzer (VNA) is used, however, in this study, a Signal generator and a Spectrum Analyzer are used to use lock in technique. The measurement circuit is shown in Fig. 21. First, I describe the mechanism for measuring spin-wave signal. Signal Generator (E8257D, Agilent Technologies) feeds RF current to the left-hand side antenna. Then, the RF current produces the RF magnetic field with 1.2 μm^{-1} wave number. This RF magnetic field emits spin waves into Fe wire. Here, external magnetic field is applied to normal direction to spin-wave propagation direction, therefore MSSWs are excited. Then excited spin waves start to propagate to right-hand side and

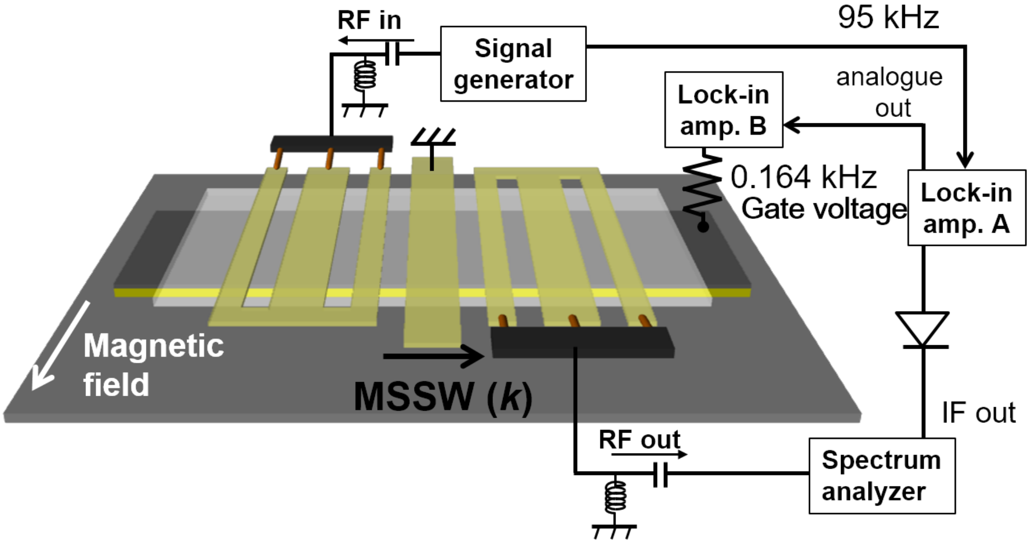

Figure. 21 Schematic image of measurement setup

An RF current is applied to the left antenna to generate the spin waves. The right antenna is set to detect the propagating spin waves using lock in Amplifier A. The voltage is applied through the gate electrode and the voltage modulated signal is detected by lock in Amplifier B through the spectrum analyzer. An in-plane magnetic field is applied normal to the spin-wave propagating direction to generate the magneto-static surface spin wave (MSSW).

left-hand side. The spin waves, propagating to right-hand side (defined as S_{21}), are only detected by the right-hand side antenna. The detected electric signal is amplified by Spectrum Analyzer. Intermediated frequency output of the Spectrum Analyzer (E4448A, Agilent Technologies) is rectified by a negative detector to change signal to the power and fed to the Lock in Amplifier (Stanford Research Systems SR830) A. The emitted RF current was frequency modulated at 95 kHz to detect its signal by using Lock in Amplifier A. Here, time constant of Lock in Amplifier A is set to 3 ms. To apply electric field into MgO|SiO$_2$ insulating layer, two antennas and gate are set to ground by using bias tee, consisting of capacitance and inductance. Then, to measure the voltage modulation signal of propagating spin waves, an AC voltage is applied to the Fe wire. The schematic image of voltage application is shown as cross section in Fig. 22. The modulated spin-wave signal is detected by Lock in Amplifier B. The modulation frequency of AC voltage is 0.164 kHz and time constant of Lock in Amplifier B is 1000 ms. Here, we have to pay attention to the relation between time constant of Lock in Amplifier A and modulation frequency of Lock in Amplifier B. For this measurement condition, the factor 116, which is decided by the time constant of Lock in Amplifier A and the modulated frequency of

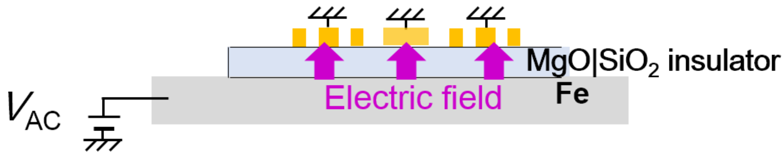

Figure. 22 Schematic image of applied electric field.
Because of two bias tee, electric fields are only applied under two antennas and gate.

Lock in Amplifier B (Details are written in appendix 2).

By applying an RF current of 12 GHz and 0.4 mW and sweeping external magnetic field from 80 mT to −80mT, spin-wave propagation signals were obtained in Lock in Amplifier A as shown in Fig. 23 (a). First, large peaks at approximately ±50 mT are found and also sub-peaks are observed. The existence of the sub-peaks can be attributed to the wave number distribution Fig. 20 (b). Second, the S_{21} intensity under the positive magnetic field is larger than that of the negative case. There are two possible mechanism; one is the localization property as show in Fig. 14 and the other is attributed to matching and mismatching between a sign of spatial rotation of the RF magnetic field produced by an antenna and that of spin waves[63]. As mentioned in chapter 2, the localization property strongly depends on the wave number and thickness of ferromagnetic layer. Here, the factor of kt_{Fe} can be estimated as 0.006. If the factor kt_{Fe} is much smaller than 1, spin waves don't localize to the interface as mentioned in chapter 2. Because of this reason, this spin-wave intensity difference is attributed to the matching and mismatching between magnetic fields of antennas and that of spin waves. Spin waves were also measured by using Vector Network Analyzer (E8364B, Agilent Technologies),

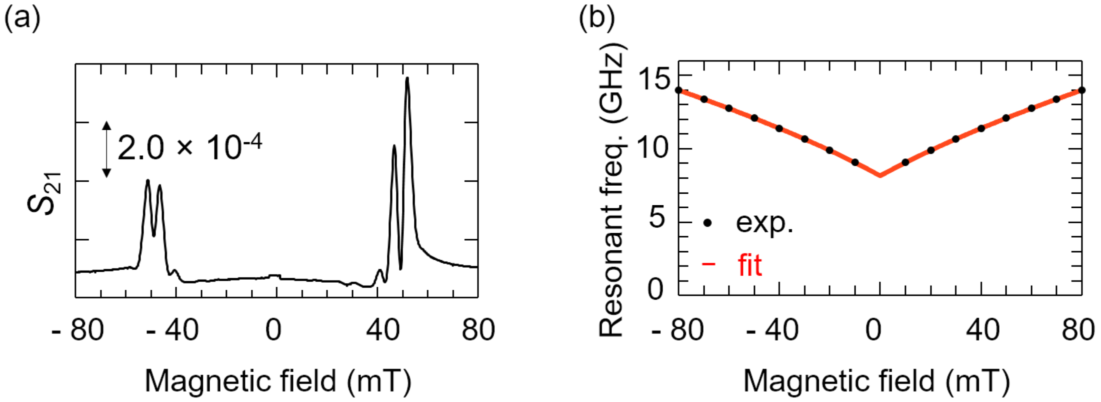

Figure. 23 Spin-wave spectrum
(a) Spin-wave spectrum obtained in Lock in Amplifier B. The detected signal is changed from mV to dB. (b) The relation between applied magnetic field and spin-wave resonant frequency peak. Black dots are experimentally obtained data by using Vector Network Analyzer and red curve is fitting results

where frequency shift was selected and S_{11} is measured. Their peak frequency at each magnetic field were plotted as black dots in Fig. 23 (b). When magnetic field is ±50 mT, spin-wave peaks are also obtained at same frequency range. This dispersion relation can be expressed as Eq. 42 as mentioned above. Here, t_{Fe}, k and $\gamma_0/2\pi$ are 5 nm, 1.2 μm^{-1} and -2.94×10^{10} T^{-1}S^{-1} for the bulk Fe[64], respectively. Then, by fitting, red curve in Fig. 23 (b) is obtained and fitting parameter crystalline anisotropy, saturation magnetization and uniaxial anisotropy field, which is *interfacial* magnetic anisotropy, are obtained as following: $H_a = 0.062$ T, $M_0 = 2.0$ T, and $H_u = 0.51$ T. Under the antenna excited spin waves start to propagate to $\pm k$ direction, therefore S_{11} spectrum should be splitting attributed to the *interfacial* DMI. In contrast, S_{11} spectrum displays the single observed peak, which indicates that the *interfacial* DMI energy was smaller than the resolution of such direct spin-wave spectroscopy ($D < 0.6$ mJ/m^2). Therefore, for the fitting described above, the *interfacial* DMI term was not included.

Figure 24 shows the voltage modulation spectra of the spin-wave propagation intensity (ΔS_{21}) measured with the lock-in Amplifier B. This spectrum was simultaneously measured with the S_{21} (Fig. 3a). The applied voltage was 3.0 V$_{\mathrm{rms}}$. At approximately ±50 mT, where the spin-wave propagation signals were also observed in Fig. 23 (a), we obtained the voltage modulation signal. The intensity of voltage modulation signal is smaller that of spin-wave propagation by almost two order and voltage modulation signal has different signal compared with propagation signal.

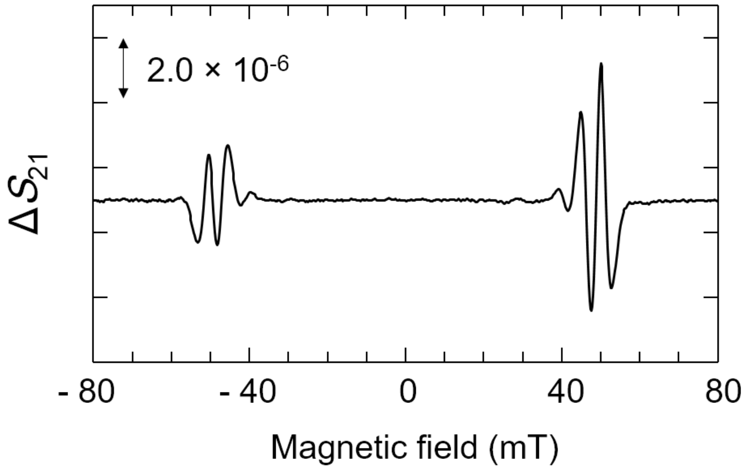

Figure. 24 Voltage modulation signal of propagating spin waves
Voltage modulation signal obtained in the Lock in Amplifier B by applying 3 Vrms. Oscillating signal were obtained at the same region as spin-wave propagation signal was observed

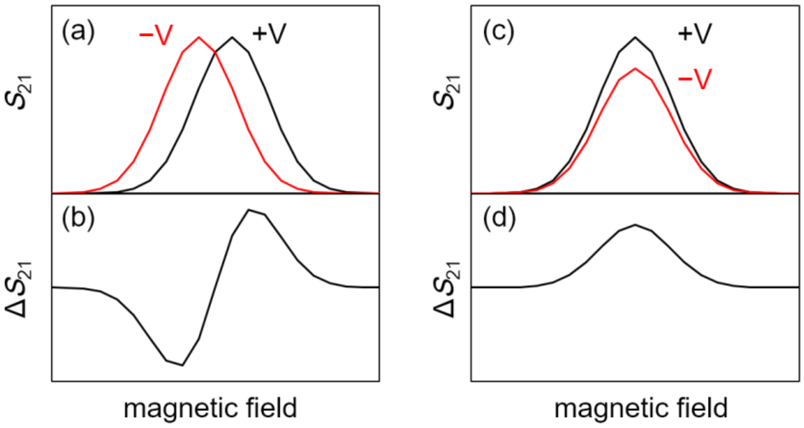

Figure. 25 Schematic image of voltage modulation signal in Lock in Amplifier B
(a), (c) The schematic image of original spin-wave signal. Black (Red) signal is the signal under positive (negative) voltage. (b), (c) The schematic image of subtracted signal, that is S_{21} (+V) – S_{12}(–V). For the case of resonant magnetic field shift, its signal becomes similar shape of numerical differentiation of original spin-wave signal, on other other hand, for the case of propagation intensity modulation, its signal becomes similar shape of original spin-wave signal.

4.2 Discussion

There will be two possible mechanisms to produce the signal obtained in Lock in Amplifier B; one is the modulation of spin-wave resonant magnetic field and the other is that of propagation intensity change. The obtained signal in Lock in Amplifier B is a subtracted signal, that is $\Delta S_{21} = S_{21}$ (3 V) – S_{21} (0 V). When the spin-wave resonant magnetic field is shifted as shown in Fig. 25 (a), the obtained signal in Lock in Amplifier B becomes similar shape of the numerical differentiation of original S_{21} signal as shown in Fig. 25 (b). On the other hand, when the propagation intensity is modulated as shown in Fig. 25 (c), the obtained signal in Lock in Amplifier B becomes similar shape of the original S_{21} signal as shown in Fig. 25 (d). Therefore, the voltage modulation signal, obtained in the Lock in Amplifier B, can be explained as following equation,

$$\Delta S_{21} = A_{\pm}(V)\mathrm{sgn}(H)\frac{dS_{21}}{dH} + B_{\pm}(V)S_{21}, \tag{43}$$

where A_+ and B_+ (A_- and B_-) are the fitting parameters for resonant magnetic field shift and spin-wave transmittance change under a positive (negative) magnetic field, respectively. A fitting result in using eq. (42) is shown in Fig. 26 as red dot oscillation signal. Since the second term is found to be negligibly small compared to the first term, the voltage modulation of propagating spin waves can be expressed as the resonant magnetic field shift of the MSSW. The fitting parameters are estimated $A_+ = A_- =120$ µT.

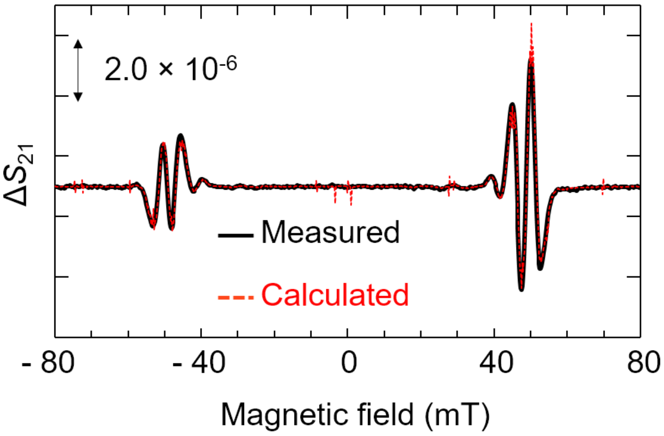

Figure. 26 Fitting result of voltage modulation signal.
Black (Red) signal is experimentally obtained (fitting) signal. The fitting signal is perfectly fitted to the experimentally obtained signal. From the fitting result, it is found that the voltage modulation is attributed to the voltage induced spin-wave resonant magnetic field shift.

Up to 3.0 V_{rms}, the amplitude of the voltage modulation signal shows linear increase to the applied voltage. As mentioned in chapter 2, by switching the magnetic field direction, chirality of spin waves is also switched. Therefore, if we have an enough resolution to measure voltage induced *interfacial* DMI change, A_+ and A_- should be changed. However, because of the accuracy of the external magnetic field, A_+ and A_- were estimated as almost same value.

In the Au|Fe|MgO artificial multilayer, the *interfacial* magnetic anisotropy in Fe|MgO interface can be controlled by the external voltage[20]. This voltage induced *interfacial* magnetic anisotropy change should be attributed to a change in band filling in the vicinity of the Fermi level due to the electric field. The effective magnetic field change caused by electric field is normal to the film plane, and therefore the resonant magnetic field shift is symmetric.

Finally, I calculated the voltage induced interfacial magnetic anisotropy energy change. The obtained fitting parameter $A_\pm$ is not *interfacial* magnetic anisotropy field shift, but the resonant magnetic field change. The relation between resonant magnetic field change and interfacial magnetic anisotropy field change can be calculated by eq. 42 as following,

$$\mathrm{d}H_\mathrm{u} = \frac{2(H_0 + A + H_\mathrm{a}) - (A + H_u) + M_0}{H_0 + A + H_\mathrm{a} + M_0(1 - \exp(-2kt_\mathrm{Fe}))/4}, \tag{44}$$

where, dH_u is the voltage induced interfacial magnetic anisotropy field change and H_0 is the resonant magnetic field. By using the parameters obtained by the fitting of the dispersion relation, dH_u is estimated as 0.29 mT. Then, we will calculate the voltage induced *interfacial* magnetic anisotropy energy change. The schematic image of its energy calculation is shown in Fig. 27. The region with oblique lines corresponds to the voltage induced *interfacial* anisotropy energy change. Here, its energy change averaged by the Fe thickness, $\mathit{\Delta} K_\mathrm{s}$ can be calculated as following,

$$\mathit{\Delta} K_\mathrm{s} = \frac{1}{2} M_0 dH_\mathrm{u} t_\mathrm{Fe}, \tag{44}$$

Here, the electric field, E, applied to the Fe|MgO interface can be calculated calculated as following,

$$E = \frac{V\varepsilon_\mathrm{SiO2}}{t_{MgO}\varepsilon_{SiO_2} + t_{SiO_2}\varepsilon_\mathrm{MgO}}, \tag{45}$$

where ε_MgO = 9.6 and $\varepsilon_{\mathrm{SiO}_2}$ = 3.6 are dielectric constant of MgO and SiO_2 and t_MgO and t_SiO2 is the thickness of MgO and SiO_2, respectively. Then its energy change par electric field can be calculated as,

$$\begin{aligned} \frac{\mathit{\Delta} K_\mathrm{s} t_\mathrm{Fe}}{E} &= \frac{1}{2} M_0 dH_\mathrm{u} t_\mathrm{Fe} \times \frac{t_{MgO}\varepsilon_{SiO_2} + t_{SiO_2}\varepsilon_\mathrm{MgO}}{V\varepsilon_\mathrm{SiO2}} \\ &= \frac{1}{2} \times 1.9 \times \frac{1000}{4\pi} \times \frac{2.9}{3} \times \frac{(50\times 9.6 + 10\times 3.9)}{3.9} \times 5\times 10^{-18} \end{aligned}, \tag{46}$$

where 1000/4π is used to change the unit and its energy change per electric field is estimated as 48 fJ/Vm. This value is almost same as that found in a previous studies of Fe|MgO based using magnetic tunneling junctions (23 fJ/Vm in Fe from ref. 65). In

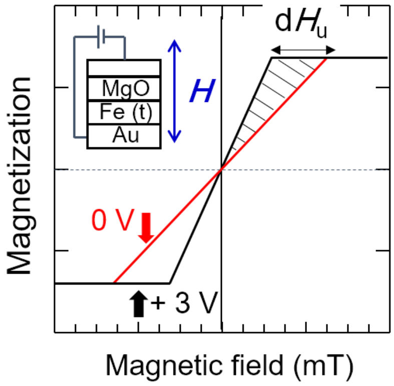

Figure. 27 The schematic image of the energy calculation.
To simplify the energy calculation, magnetic field is applied to normal to film plane direction. Then by a voltage application can change the magnetization curve from red line to black line. Then, the region with oblique line corresponds to the voltage induced interfacial anisotropy energy change.

previous researches, the quite large voltage induced magnetic anisotropy change were observed, however, they are attributed to the oxidization and reduction change of Fe[66,67,68]. Here, the observed energy change is almost same order as previous research, which may be only attributed to the electron state change. Therefore, the observed voltage modulation also be attributed to the electron state change in the Fe|MgO interface.

Here, a voltage modulation of exchange stiffness constant can contribute. However, because of the long wavelength of an MSSW, the frequency is not sensitive to the exchange stiffness, and its voltage-induced change should not be detected.

4.3 Conclusion

To conclude, the voltage modulation of a magneto-static surface waves (MSSWs) in an Fe thin film is demonstrated first in the world. I found that the mechanism of voltage modulation is voltage induced spin-wave resonant magnetic field change, attributed to the voltage induced *interfacial* magnetic anisotropy field change. In this magnetic-field-sweep measurement, voltage induced *interfacial* DMI change cannot be observed.

Chapter 5. Result and discussion 2 (Voltage induction of interfacial Dzyaloshinskii-Moriya interaction)

As shown in Chapter 4, I succeeded in measuring voltage modulation signal of propagating spin waves. The voltage modulation is attributed to the voltage induced spin-wave resonant magnetic field shift and the voltage induced interfacial anisotropy change is dominant. The signal to noise ratio is not for enough to investigate voltage induced *interfacial* DMI change for the signal, obtained by the external magnetic field sweep. In this chapter, I investigate the voltage induced *interfacial* DMI change in Au|Fe|MgO artificial multilayer system, by using Frequency sweep measurement. By the frequency sweep measurement, the voltage modulation signal of *i*DMI was observed in the propagation direction dependent signal. The main results were published as Applied Physics Express **8**, 063004, (2015)

5.1 Sample fabrication

Au|Fe|MgO artificial multilayer was also deposited on an MgO (001) substrate by using molecular beam epitaxy method. The film stack is an MgO(001) substrate|MgO(5 nm)|Cr(5 nm)|Au(50 nm)|Fe wedge(t_{Fe} = 2-23 nm)|MgO(10 nm) as shown in Fig.28. The artificial multilayer has the wedge structure to measure thickness dependence of two voltage effects; voltage induced *interfacial* magnetic anisotropy change and voltage induced *interfacial* DMI change. By the same fabrication process as Chapter 3 and 4, the spin-wave device was fabricated. The Fe layer was patterned into

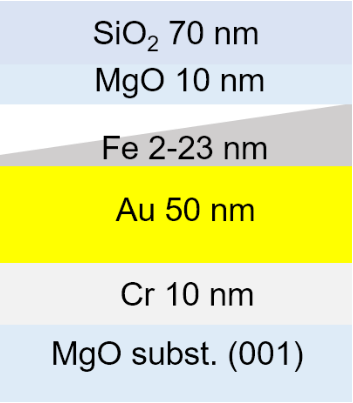

Figure. 28 Film stack used in this chapter.
Fe layer has wedge structure to measure thickness dependence of voltage induced *interfacial* magnetic anisotropy change and *interfacial* DMI change.

100 × 400 μm rectangular shape and the antennas on the Fe wire also excite MSSWs with wavenumber 1.2 μm^{-1}.

5.2 Measurement

To measure spin waves, VNA was used. Figure 29 (a) shows measurement circuit, used to measure basic spin-wave property. To measure spin-wave signal, at first, large

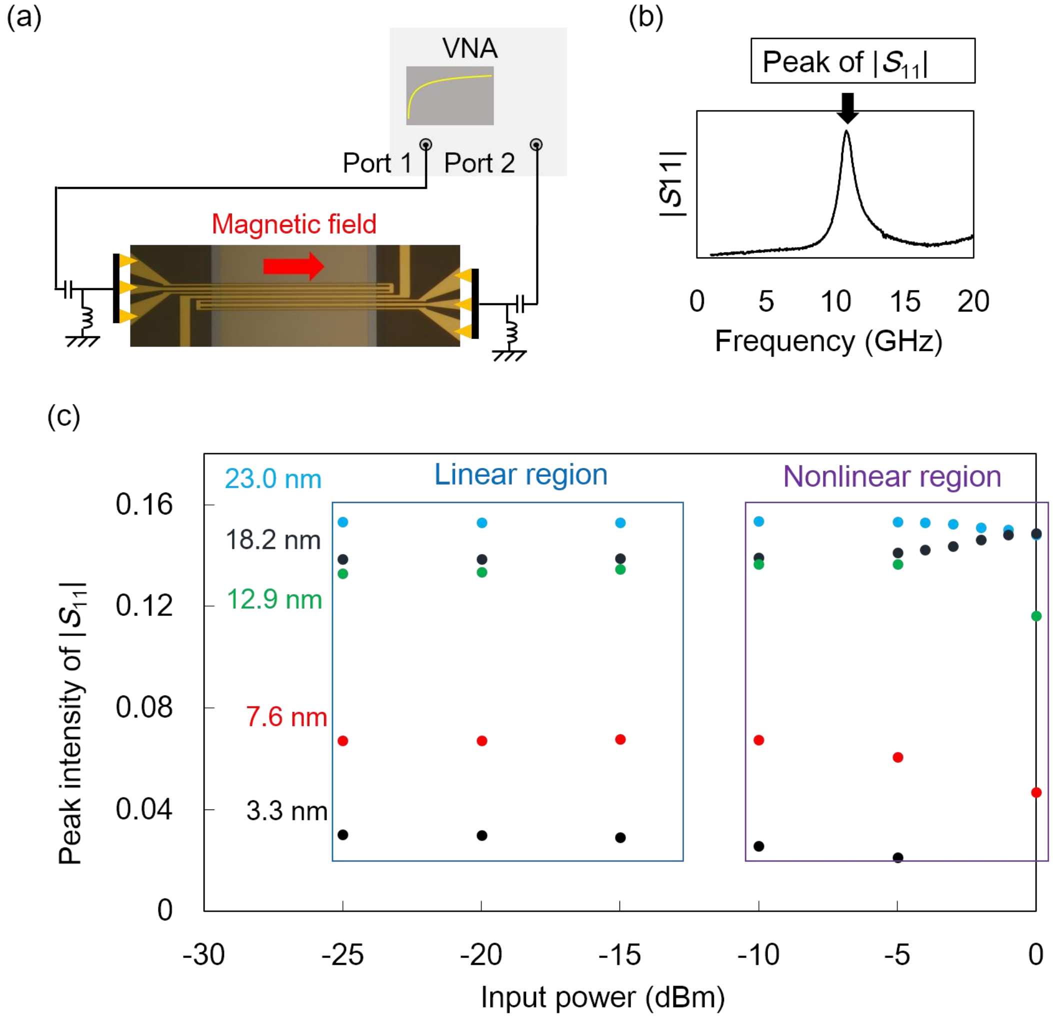

Figure. 29 Measurement circuit to measure spin-wave basic property.
(a) Measurement circuit to measure spin waves. Two bias tee is used to protect machine from static electricsity and to measure spin-wave basic property with same measurement circuit as voltage modulation measurement (b) Typical spin-wave signal in $|S_{11}|$. Single peak was observed. (c) The relation between the power of RF current and peak intensity, for each Fe thickness. Less than -15 dBm, linear relation is observed for each Fe thickness.

magnetic field, here 2,70 mT, was applied to saturate magnetization of Fe film to magnetic field direction. Then, relatively small magnetic field was applied. To obtain the spin-wave spectrum as shown in Fig. 29 (b), the spectra obtained at each magnetic field were subtracted the spectrum at large magnetic field (2,70 mT) to erase the background signal attributed to the shape of antenna, for example. To decide a power of applied RF current, the dependences of power of an RF current on the spin-wave intensity were measured for each Fe thickness. As shown in Fig. 29 (c), less than -15 dBm (32 μW), the intensity of spin waves doesn't depend on the power of RF current. On the other hand, greater than -15 dBm, the intensity starts to depend on the power. That is, less than -15 dBm, spin-wave dynamics has linear to the applied RF power, and greater than -15 dBm, spin-wave dynamics has non-linear relation to the applied RF power. Because this reason, following measurement was done with -15 dBm. Then, Dispersion relations were measured for each Fe thickness and they were fitted by using eq. 42. The obtained data of crystalline anisotropy and interfacial anisotropy are shown in Fig. 30 (a) and (b), where k and $\gamma_0/2\pi$ and M_0 are 1.2 μm^{-1} , 2.16 mT[64] and - 2.94 × 10^{10} $T^{-1}S^{-1}$ for the bulk Fe[64]. The crystalline anisotropy increase as increasing Fe thickness, and it almost saturate about 20 nm. Its saturated value almost becomes 57 mT, and its almost same as the value of balk Fe[64]. On the other hand, the interfacial anisotropy increase as decreasing Fe thickness and this is the general property for the interfacial effect. As mentioned in Chapter 4, if sample has the observable *interfacial* DMI, peak splitting should be observed in the $|S_{11}|$ signal. However, in the series of these measurement, peak splitting was not observed. Therefore, the D value was estimated to be smaller than our resolution of up to 0.5 mJ/m^2.

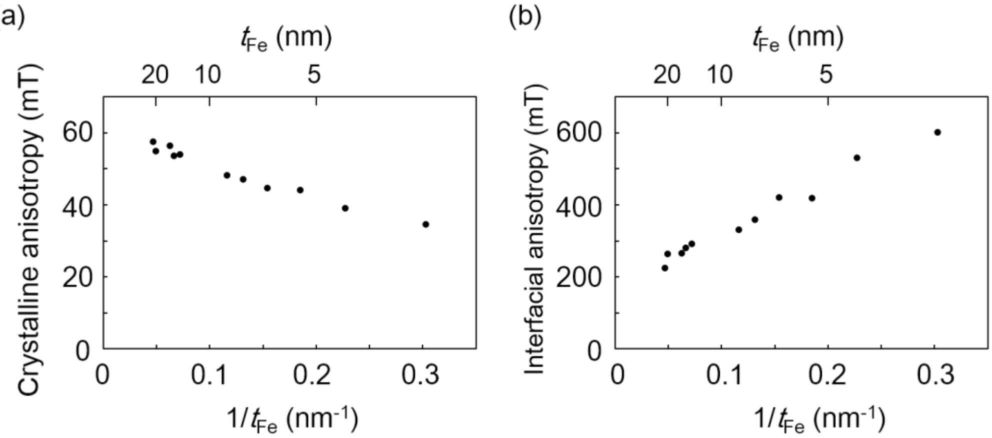

Figure. 30 Fe thickness dependence on crystalline and *interfacial* anisotropy.
(a) Thickness dependence on crystalline anisotropy. Its value almost saturate around 20 nm. (b) Thickness dependence on interfacial anisotropy. Its increase as decreasing Fe thickness. This is general property for the interfacial effect.

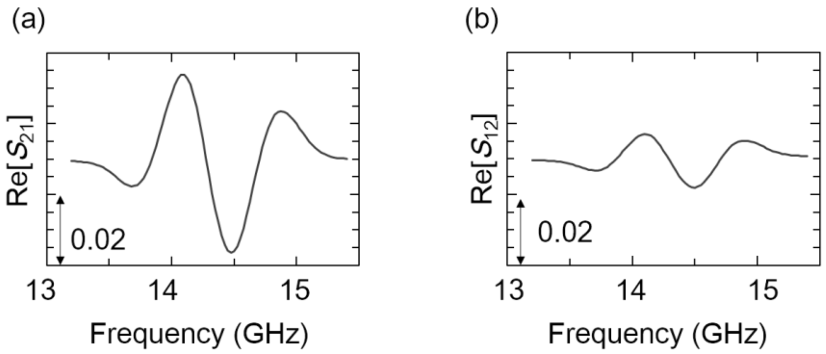

Figure. 31 spin-wave propagation signals

(a), (b) Typical spin-wave propagation signal of Re[S_{21}, S_{12}] in Au(50 nm)/Fe(20 nm)/MgO(10 nm)/SiO_2(70 nm) under 40 mT. Oscillation signal, meaning spin-wave propagation, were observed around 14.5 GHz. In the other region, magnetic field dependent spin-wave signal was not observed.

Figure 31 (a) shows spin-wave propagation signal (Re[S_{21}]) as defined in Fig. 32 (a) in 20 nm-thickness Fe film under 40 mT-external magnetic field. An oscillating signal around 14.5 GHz in the frequency domain resulted as a consequence of the spin-wave propagation. Similar signal was also obtained in Re[S_{12}] shown in Fig. 31 (b) These signal were also obtained by subtracting the background signal (Re[S_{21}] and Re[S_{12}] at 270 mT). The difference in the propagation intensity is also attributed the

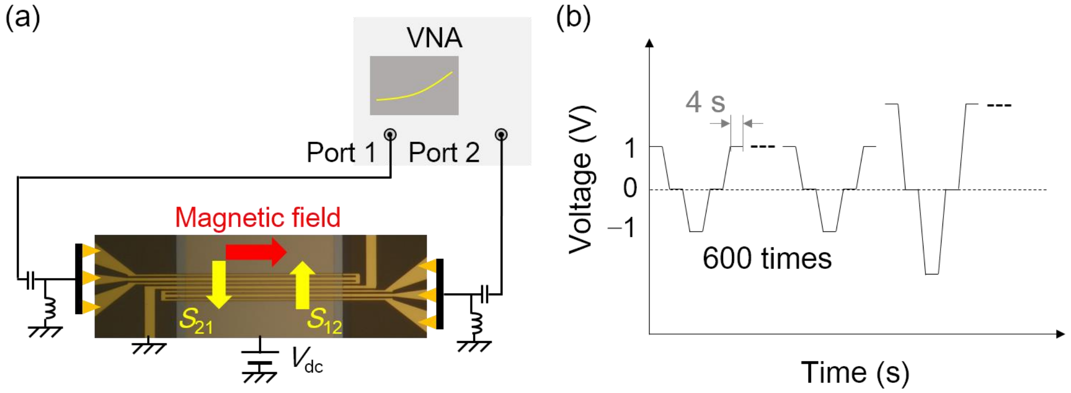

Figure. 32 Schematic image of measurement set up for the voltage application and that of measurement sequence

(a) The voltage was applied to the Fe wire. The electric field is applied into MgO|SiO_2 insulating layer under two antennas and gate. (b) The schematic image of voltage sweep. While keeping positive voltage, all spin-wave spectra were measured. Then, voltage was swept to zero, negative and zero again and also all spin-wave spectra were measured for each voltage. Finally, these obtained spectra were averaged.

rotation direction mismatch of magnetic field produced by antennas and spin waves.

Then, an external DC voltage was applied to the thin Fe wire as shown in Fig. 32 (a). In the first voltage modulation measurement, it takes about 4 hours to measure a signal for each voltage. It may damage MgO|SiO$_2$ insulating layer to apply constant voltage for 4 hours. Therefore, in this measurement, voltage-sweep was selected. The schematic image of voltage sweep is shown in Fig. 32 (b). During less than 4 second, voltage was kept positive and ten of S_{21} spectra and other ten of S_{12} spectra were taken by the VNA with 1 kHz band width. The same was repeated keeping voltage at zero, negative and zero again. These four sets of measurements were repeated 600 times. Then, the voltage modulation signal ΔRe[S_{21}] shown in Fig. 33 (a) with black line was obtained by averaging the series of all spin-wave spectra and by subtracting Re[S_{21}] at 0 V from Re[S_{21}] at 4 V, for example. As discussed in Chapter 4, voltage modulation of propagating spin waves is attributed to the voltage induced resonant frequency shift in Fe, since they are the results of frequency domain measurement. Then, the obtained voltage modulation spectra can be described as following equation,

$$\Delta \mathrm{Re}[S_{21}] = -\delta f_{21} \times d\,\mathrm{Re}[S_{21}]/df\ , \tag{47}$$

where, δf_{21} is the voltage-induced frequency shift and $d\,\mathrm{Re}[S_{21}]/df$ is a numerical differentiation of the S_{21} spectra. The red oscillating signal in Fig. 33 (a) is the fitting result of Eq. (47). The experimentally obtained ΔRe[S_{21}] was almost completely reproduced by Eq. (47), and δf_{21} was estimated to be −0.129±0.004 MHz. The same analysis was conducted for Re[S_{12}] and those results are shown in Fig 18 (b). The resonant

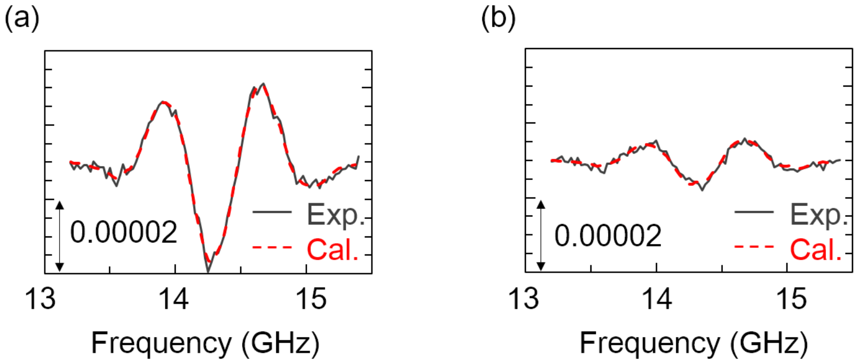

Figure. 33 Typical voltage modulation signal in Au|Fe|MgO

(a), (b) Black oscillation spectra are experimentally obtained. These voltage modulation spectra were obtained by subtracting Re[S_{21}] (Re[S_{12}] at 0 V from Re[S_{21}] (Re[S_{12}] at 4 V. Red broken oscillation spectra are fitting result. Fitting spectra is almost identified to the experimentally obtained signal.

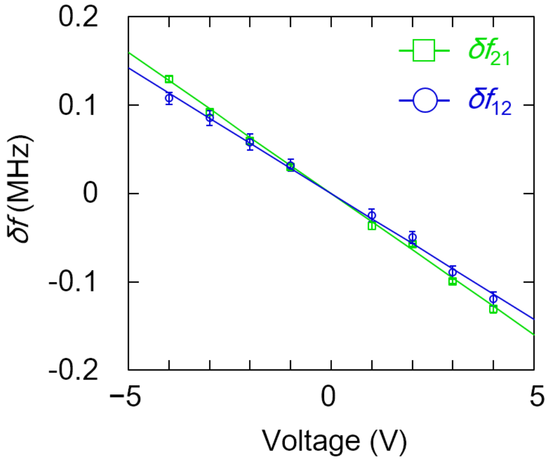

Figure. 34 Bias voltage and spin-wave direction dependence of the resonant frequency change induced by the voltage (V_{DC}) under 40 mT.

The black (blue) dots show the resonant frequency change of Re[S_{21}] (Re[S_{12}]). The black (blue) lines are fitting lines of $\delta S_{21}/V_{DC}= -0.032$ (MHz/V)($\delta S_{12}/V_{DC} = -0.028$ (MHz/V)). This directional asymmetry means that the voltage effect is attributable to not only the interfacial magnetic anisotropy change but to the *interfacial* Dzyaloshinskii-Moriya interaction.

frequency shift, δf_{21}, induced by the external voltage was estimated to be −0.108±0.007 MHz. These analysis were conducted for each voltage. In Fig. 34, δf_{21} and δf_{12} are plotted as a function of the applied voltage. From the graph, linear dependence on the voltage is confirmed for both cases. From the analysis of the time-series data, I found that the response shows neither hysteresis nor aging effect. Therefore, I believe that the effect is not from ionic conduction, such as the surface oxidation induced by the voltage.[66-68] Here, these slopes are estimated to $\delta f_{21}/V_{DC}=-0.032\pm0.001$, $\delta f_{12}/V_{DC}=-0.028\pm0.001$ (MHz/V), respectively. Note that there is a distinct difference between $\delta f_{21}/V_{DC}$ and $\delta f_{12}/V_{DC}$; that is, chirality-dependent voltage effect was observed.

5.3 Discussion

Voltage-induced frequency shifts consist of two contributions; one is propagation-direction independent, and the other is propagation-direction dependent. First, I focus on the propagation-direction independent effect. The propagation-direction independent term should be attributed to the voltage-induced *interfacial* magnetic anisotropy change at the Fe|MgO interface. Here, I prepare the equation to analyze the *interfacial* anisotropy field change caused by a voltage application. From total differentiation of eq. 42, following equations can be obtained as propagation direction dependent frequency shift,

$$\begin{aligned} \mathrm{d}f_{21} &= -\frac{\gamma}{2\pi}\sqrt{\left(|H_0|+H_\mathrm{a}\right)\left(|H_0|+M_0+H_\mathrm{a}-\mathrm{d}H_\mathrm{u}\right)+\frac{M_\mathrm{S}}{4}\left(M_\mathrm{S}-\mathrm{d}H_\mathrm{u}\right)\left(1-\exp\left(-2|k_1|t_\mathrm{Fe}\right)\right)}+\frac{\gamma}{\pi M_0}k\mathrm{d}D \\ \mathrm{d}f_{12} &= -\frac{\gamma}{2\pi}\sqrt{\left(|H_0|+H_\mathrm{a}\right)\left(|H_0|+M_0+H_\mathrm{a}-\mathrm{d}H_\mathrm{u}\right)+\frac{M_\mathrm{S}}{4}\left(M_\mathrm{S}-\mathrm{d}H_\mathrm{u}\right)\left(1-\exp\left(-2|k_1|t_\mathrm{Fe}\right)\right)}-\frac{\gamma}{\pi M_0}k\mathrm{d}D \end{aligned} ,\tag{48}$$

where I only consider voltage induced *interfacial* anisotropy field change and *interfacial* DMI change and $\mathrm{d}f_{21}$, $\mathrm{d}f_{12}$, $\mathrm{d}H_\mathrm{u}$ and $\mathrm{d}D$ are minor change of spin-wave resonant frequency, *interfacial* anisotropy change and *interfacial* DMI change. Then, by calculating propagation–direction independent term, we can obtain following equation,

$$\frac{\delta H_\mathrm{u}}{V_\mathrm{DC}} = -\left(\frac{2\pi}{\gamma}\right)^2 f\left(\frac{\delta f_{21}}{V_\mathrm{DC}}+\frac{\delta f_{12}}{V_\mathrm{DC}}\right)\Bigg/\left(H_0+H_\mathrm{c}+\frac{M_0}{4}\left(1-e^{-2kt_\mathrm{Fe}}\right)\right). \tag{49}$$

Then, voltage induced interfacial anisotropy field change, $\delta H_\mathrm{u}/V_\mathrm{DC}$, can be estimated to be 8.1 μT/V. These analysis was conducted to the other samples with different Fe thickness. The Fe-thickness dependence of the δH_u is displayed in Fig. 35 as black dots. Since the signal-to-noise ratio in the spin waves and its voltage modulation signals are quite low for the samples with $t_\mathrm{Fe} < 7$ nm, we plotted δH_u obtained only for the samples with $t_\mathrm{Fe} > 7$ nm. From Fig. 35, δH_u is inversely proportional to the Fe thickness

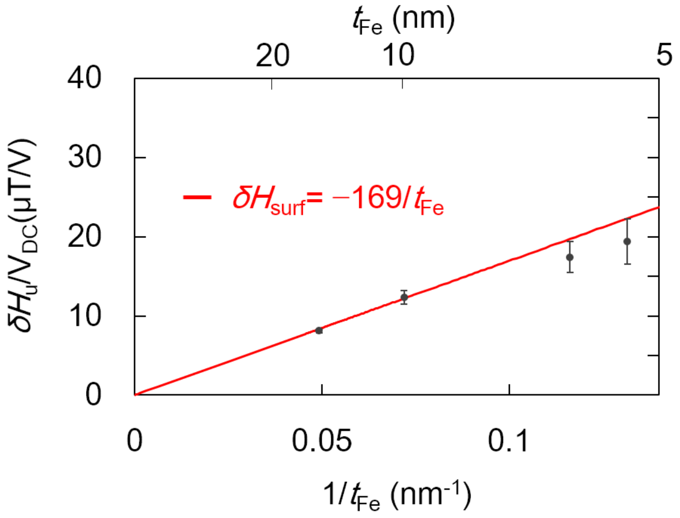

Figure. 35 Fe thickness dependence of voltage induced interfacial anisotropy field change

Black dots shows experimentally obtained effective field change by the external voltage. The line in red shows that the field change is inversely proportional to the Fe thickness (t_Fe).: ($\delta H_\mathrm{u} = 169$ (μT·nm/V)/t_Fe (nm))

($\delta H_{\mathrm{u}}/V_{\mathrm{DC}} = 169/t_{Fe}\left(\mu\mathrm{T}\cdot\mathrm{nm}/\mathrm{V}\right)$). Then, by using the dielectric constant of MgO and SiO_2 shown in Chapter 4 and above obtained $\delta H_{\mathrm{u}}/V_{\mathrm{DC}}$, voltage induced interfacial anisotropy energy change can be estimated to be26 fJ/Vm, which is also the same order as previous result. To date, studies on the voltage-induced anisotropy change are limited to ultrathin (< 5 nm) ferromagnetic metal film because the voltage effect in the large thickness region is too small to study from changes in magnetization curves. In this study, because we employed a measurement technique that uses magnetic resonance, we succeeded in characterizing the voltage effect in the relatively thick ferromagnetic metals (> 5 nm).

Second, I focus on the propagation direction-dependent effect. By breaking the inversion symmetry in Fe|MgO interface together with the spin-orbit interaction, the *interfacial* DMI can be induced into the Fe wire. The propagation direction-dependent term can be attributed to this voltage-induced *interfacial* DMI and/or to a surface localisation of the MSSW together with the anisotropy change at Fe|MgO interface. The latter mechanism clearly can be discredited because kt_{Fe} is much smaller than 1 as discussed in chapter 2. In the following discussion, I only focus only on the first

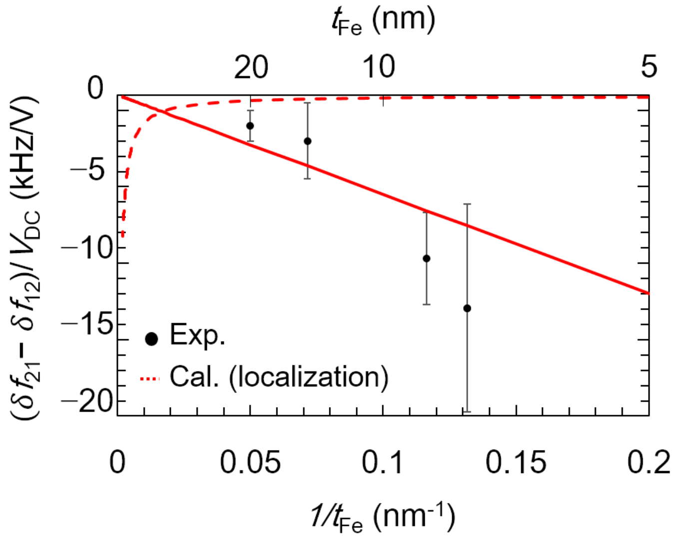

Figure. 36 Fe thickness dependence of voltage induced propagation-direction dependent frequency shift

Black dots shows experimentally obtained propagation-direction dependent frequency shift by the external voltage. The bold line in red shows the line to the eye guide and broken line in red shows the calculated line from the localization property of MSSW. As expected, the surface localization property doesn't attribute dominantly but *interfacial* DMI change attributes mechanism. Then, by calculating propagation–direction dependent term, we can obtain following equation,

$$\frac{\mathrm{d}D}{V_{\mathrm{DC}}} = -\frac{1}{2}\left(\frac{\mathrm{d}f_{21}}{V_{DC}} - \frac{\mathrm{d}f_{12}}{V_{DC}}\right)\left(\frac{\pi M_{\mathrm{S}}}{\gamma k}\right). \tag{50}$$

From the propagation direction-dependent frequency shift obtained in Fig. 34 and Eq. (50), we can estimate the *interfacial* DMI change, dD, to be −40 nJ/m^2 at 1 V. The Fe thickness dependence was also studied like *interfacial* anisotropy field change shown in Fig. 35. The black dots indicate the experimentally obtained data and the red broken curve is calculated line from the surface localization property of MSSW (See appendix 3 for details). If this propagation-direction dependent frequency shift is attributed to a voltage induced *interfacial* DMI change, its propagation-direction dependent frequency shift should be inversely proportional to Fe thickness, since it is *interfacial* effect. On the other hand, if it is attributed to a surface localization property, its shift should be proportional to the Fe thickness. As expected, the observed frequency shift is smaller for greater Fe thickness shown as red bold line in Fig. 36. The reported built in D constant of *interfacial* DMI is about 1.0 mJ/m^2 in the domain wall system and spin-wave system, for example. In the present study, we found that −40 nJ/m^2 can be induced by an external voltage (V_{DC}=1 V). It seems to be much smaller than the built in *interfacial* DMI. However, in this research, the thickness of ferromagnetic layer is thick and also Au and MgO don't have large spin-orbit interaction. Because of this reason, the observed voltage induced *interfacial* DMI change may become small. Therefore, if we employ the more appropriate multilayer system in regards to the layer thickness, spin-orbit interaction and electronegativity, the larger built in *interfacial* DMI and its voltage induced change would be obtained.

I also study the contribution from leak currents. Two mechanism can possibly cause propagation-direction dependent frequency shift. One is the spin-wave Doppler shift[62], and the other is the Oersted field. In our system, the current flow induced by the external voltage was less than 0.4 nA (80 A/m^2), which was too small to cause such current-induced frequency shift.

5.4 Conclusion

To conclude, this research investigated the effect of external voltage on propagating MSSWs in the Au|Fe|MgO artificial multilayer. The result obtained show that voltage induced frequency shift is attributed to two voltage effect; one is voltage induced *interfacial* magnetic anisotropy change and the other is voltage induced *interfacial* DMI change. The obtained voltage induced *interfacial* anisotropy change was same order and same sign as previous result. The voltage induced *interfacial* DMI change was demonstrated for the first time and its change was −40 nJ/m^2 in 20 nm- thickness-Fe. The observed *interfacial* DMI change seems to be much smaller, however, it would be enhanced by the material engineering. This voltage control of *interfacial* DMI could become a milestone for the electric control of chirality dependent magnetic property, like skyrmion lattice. In next chapter, I propose one of the idea to enhance this *interfacial* DMI change and demonstrate it.

Chapter 6. Result and discussion 3 (Enhancement of voltage induced *interfacial* Dzyaloshinskii-Moriya interaction change)

As shown in the Chapter 5, by measuring propagation-direction dependent voltage effect, I succeeded in measuring voltage modulation of *interfacial* DMI. However, comparing with the built in *interfacial* DMI, its change seemed to be too small, therefore to apply its change to control some magnetic property seemed to be impossible. In this section, I propose one of the idea to enhance voltage induced *interfacial* DMI change. The *interfacial* DMI should be attributed to the spin-orbit interaction, therefore, in this research, I inserted ultra-thin Pt into Fe|MgO interface, because Pt has large spin-orbit interaction and electric field can be only applied this interface. By inserting one monolayer Pt, the voltage induced *interfacial* DMI change was enhanced. In this chapter, I also show the possible mechanism of voltage modulation of *interfacial* DMI and the idea of practical application of *interfacial* DMI for the magnetic device; that is voltage excitation and annihilation of skyrmion lattice by using voltage induced *interfacial* DMI change.

6.1 Sample fabrication

Fe|Pt|MgO artificial multilayers was also deposited on an MgO (001) substrate using molecular beam epitaxy method in National institute of Applied Industrial Science and Technology. The film stack is an MgO (001) substrate|MgO (3 nm)|V (30 nm)|Fe (20

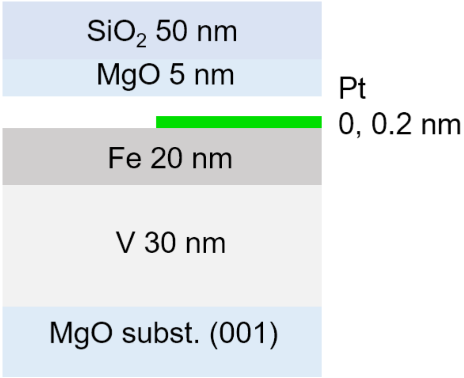

Figure. 37 Film stack used in this chapter.
Ultra-thin Pt layer were inserted into Fe|MgO interface. Pt 0 nm region was prepared to compare the result of voltage effect with Pt and without Pt on the same MgO substrate.

nm)|Pt (0, 0.2 nm)|MgO (5 nm)|SiO_2 (50 nm) shown in Fig. 37. In this research, buffer layer was changed from Au to Cr, since one monolayer Au can segregate to Top Fe surface. Thickness of MgO and SiO_2 was also changed to 5 nm and 50 nm to apply larger electric field. By the same fabrication process as Chapter 3-5, the spin-wave devices were fabricated. The Fe layer was patterned into 100 × 400 μm rectangular shape and the antennas on the Fe wire also excite MSSWs with wavenumber 1.2 μm^{-1}.

6.2 Measurement

The spin-wave property was investigated by measuring S parameter by using VNA. The power of RF current was set to -15 dBm (32 μW) to measure them in linear region. Figure 38 shows obtained spin-wave resonant frequency as function of applied magnetic field. The black (red) open circles and dot curves are experimentally obtained spin-wave resonant frequency and their fitting result by eq. 41 of Fe|MgO (Fe|Pt|MgO), where, k and $\gamma_0/2\pi$ and M_0 are 1.2 μm^{-1} 2.16 T^{64} and - 2.94 × 10^{10} $T^{-1}S^{-1}$ for the bulk Fe^{64}. From the fitting results, crystalline anisotropy, H_a, and interfacial anisotropy, H_u, were estimated to be 66 mT and 140 mT for Fe|MgO and 66 mT and 195 mT for Fe|Pt|MgO, where crystalline anisotropy was unified to what was obtained in Fe|MgO. By inserting one monolayer Pt, interfacial anisotropy was enhanced. The peak splittings were not observed in $|S_{11}|$ for both spin-wave signal, therefore, the built-in interfacial DMI was

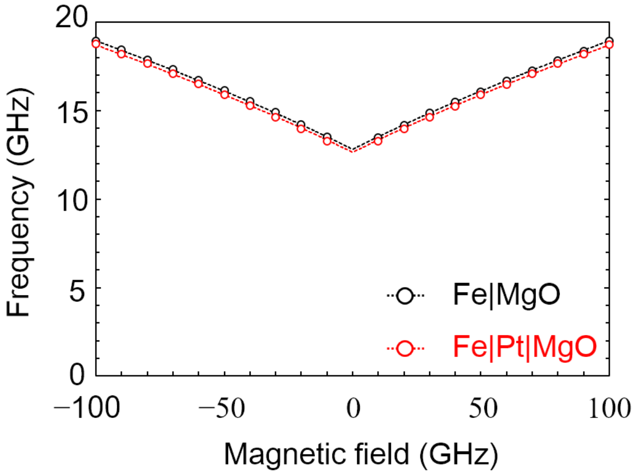

Figure. 38 The relation between applied magnetic field and spin-wave resonant frequency

Black (red) open circles and dot curve corresponds to experimentally obtained spin-wave resonant frequency and fitting curve obtained by eq. 43 of Fe|MgO (Fe|Pt|MgO)

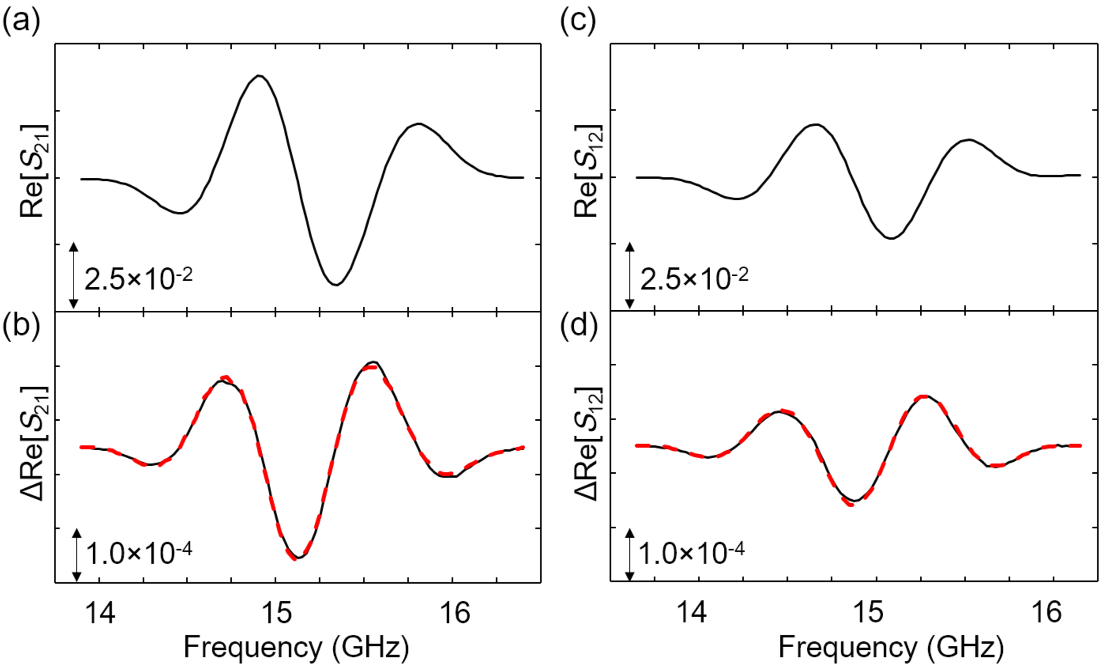

Figure. 39 Spin waves and their voltage modulation signals
(a), (c) The spin-wave propagation signal in Fe|Pt|MgO when an external magnetic field of 40 mT is applied. The real part of the S-parameters (Re[S_{21}] and Re[S_{12}]) are displayed. (b), (d) Voltage modulated spin-wave signals. The values of ΔRe[S_{21}], expressed as the solid black line, are defined as the subtracted signal of the Re[S_{21}]; the Re[S_{21}] measured at 0 V is subtracted from the value of 5 V. The dashed red curves are the fitting results from using equation (46). From the fitting, the resonant frequency shifts induced by the voltage are estimated to be 0.718 MHz and 0.638 MHz for S_{21} and S_{12}, respectively.

smaller than resolution of such direct spin-wave spectroscopy. (D < 0.6 mJ/m^2).

Figure 39 (a) shows spin-wave propagation signal (Re[$S21$]) of Fe|Pt|MgO under H_0 40 mT. An oscillating signal was observed around 15 GHz. Then, a direct current external voltage, V_{DC} =5 V, was applied to modulate the propagating spin waves shown Fig. 32(a). The voltage modulation spectrum, defined as $\Delta\mathrm{Re}[S_{21}] = \mathrm{Re}[S_{21}(5\ \mathrm{V})] - \mathrm{Re}[S_{21}(0\ \mathrm{V})]$, is shown in Fig. 39 (b) with the solid black curve. The broken red curve in Fig. 39 (b) is a fitting curve produced by the eq. (47). From the fitting, the frequency shift, δf_{21}, was estimated to be 0.718 ± 0.007 MHz. Figure 39 (c) and (d) show the same measurement and analysis performed for S_{12}. From the fitting of voltage modulation signal of S_{12}, the voltage induced frequency shift was estimated to be 0.638 ± 0.006 MHz. The propagation direction dependence was also observed in this artificial multilayer.

Figure 40 shows the summary of voltage-induced frequency shift. The green and

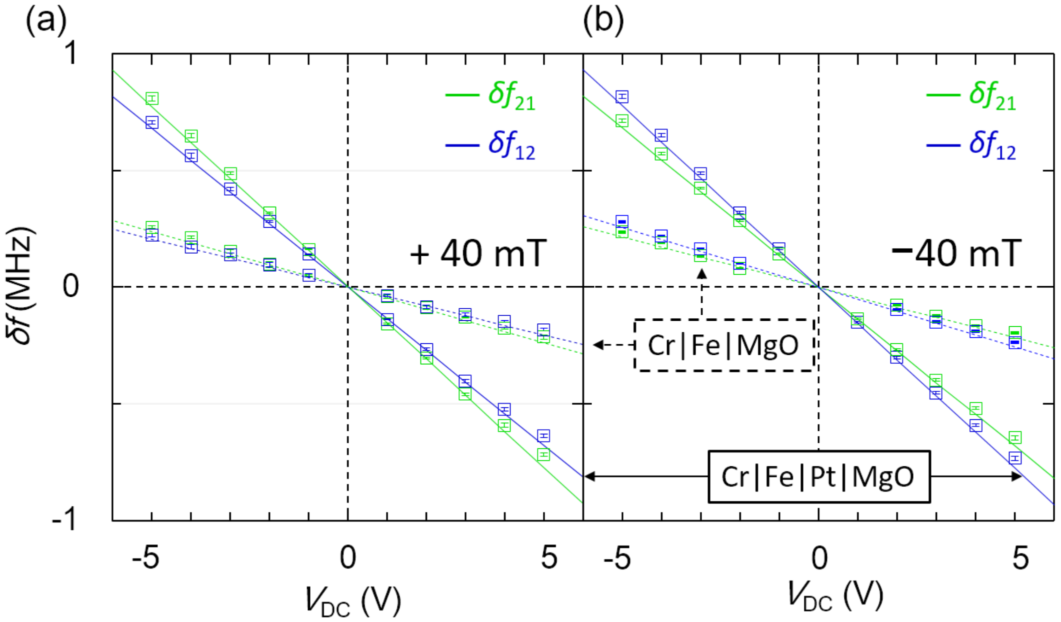

Figure. 40 Propagation direction and magnetic field direction dependence on the voltage induced frequency shift

(a), (b) The voltage induction of the resonant frequency shift in the propagating spin waves. The vertical axis plots in green and blue the resonant frequency shifts δf_{21} and δf_{12} for the propagating spin-wave signals S_{21} and S_{12}, respectively. The horizontal axis expresses the external voltage V_{DC}. Lines mark the linear fits of the experiment. The solid and dashed lines denote the fitting lines for Fe|Pt|MgO and Fe|MgO, respectively. A magnetic field of 40 mT was applied. From the fit, $\delta f_{21}/V_{DC}$ and $\delta f_{12}/V_{DC}$ for Fe|Pt|MgO and Fe|MgO are estimated to be 0.155 MHz/V and 0.048 MHz/V) and 0.136 MHz/V and 0.041 MHz/V, respectively. Note that the chirality-dependent frequency shift is enhanced by the monolayer insertion of Pt at the Fe|MgO interface.

blue plots express the frequency shift δf_{21} and δf_{12}, respectively. The lines are the linear fits. For the all cases, the frequency shifts are linear functions of the applied DC voltage. Here, the voltage-induced $\delta f_{21}/V_{DC}$ ($\delta f_{12}/V_{DC}$) = −0.155 ± 0.005 MHz/V (−0.135 ± 0.004 MHz/V). Estimates of the voltage-induced frequency shifts in Cr|Fe|MgO were $\delta f_{21}/V_{DC}$ ($\delta f_{12}/V_{DC}$) = −0.048 ± 0.003 MHz/V (−0.041 ± 0.003 MHz/V). First, one can observe the distinct propagation direction dependence of the frequency shift. Second, both the frequency shift and its propagation direction dependence are enhanced by inserting one atomic layer of Pt.

As mentioned above, the chirality of the MSSWs should have been inverted when we reversed the magnetic field direction. Figure 40 (b) shows the result where an oppositely signed magnetic field of −40 mT was applied. The propagation direction dependencies of the frequency shifts switched with one another when we compared the results in Fig. 40 (a) with those in Fig. 40 (b). Reproducibility of these results was confirmed in several devices on the same wafer. This propagation and magnetic field dependence of frequency shifts agrees with the premise that the propagation dependence is caused by voltage-induced *interfacial* DMI changes.

6.3 Discussion

As mentioned in Section 5, voltage induced frequency shifts consist of two contribution; propagation-direction independent frequency shift attributed to the voltage induced interfacial anisotropy change, and the other is propagation-direction dependent frequency shift attributed to the voltage induced *interfacial* DMI change. By using the same analysis method shown in Chapter 5, the voltage induced interfacial anisotropy energy change can be estimated to be 85± 5 fJ/Vm for Fe|Pt|MgO and 27± 5 fJ/Vm for Fe|MgO. The anisotropy energy change of Cr|Fe|MgO nearly matches the results obtained for Fe|MgO-based magnetic tunnelling junctions (23 fJ/Vm)[65]. Note that inserting one monatomic layer of Pt into the Fe-MgO interface increases by more than three times the change in voltage-controlled magnetic anisotropy. Our results show that the voltage-induced anisotropy energy change can be engineered by a one-atomic-layer insertion of Pt.

The propagation direction dependent frequency shift is attributed to the voltage induced *interfacial* DMI change. The contribution of surface localization property of MSSW is less than 10 % in Fe 20-nm-thickness sample as shown in Fig. 36, therefore, its contribution for the propagation direction dependent term may be negligibly small in

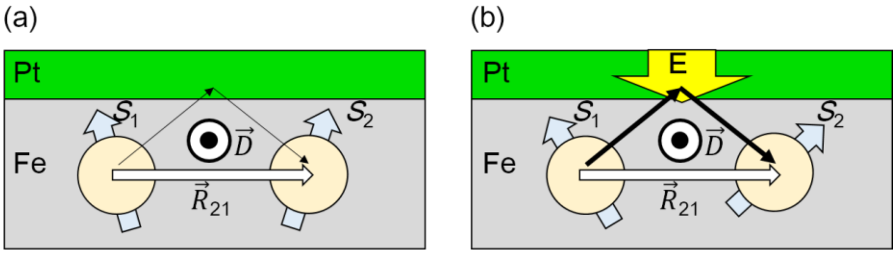

Figure. 41 Schematic image of voltage induced interfacial DMI change
(a), (b) *interfacial* DMI without (with) external electric field. Interfacial DMI can be produced without external electric field by the internal electric field attributed to the electro-negativity. The direction of interfacial DMI is selected by the direction of the film stack and/or electric field and relative position between two magnetic atoms.

these samples. The voltage induced interfacial DMI change can be calculated by eq. 50, and it was estimated to be 0.95 μJ/m^2 for Cr|Fe|Pt|MgO and 0.37 μJ/m^2 for Cr|Fe|MgO for the application of 5 V. Note that Pt insertion into Fe|MgO interface enhance threefold the voltage-induced D constant.

Since the *interfacial* DMI is strongly depends on the spin-orbit interaction of the adjacent layer, one can expect that a voltage-induced *interfacial* DMI is also strongly depends on it. The insertion of a Pt layer shields the electric field on the Fe layer; even so, we observed a large enhancement in the voltage-*induced* interfacial DMI. This result implies that the electric field applied to the Pt may cause a large change in the *interfacial* DMI. It is well known that, in multiferroic systems, the DM-vector and electric polarization $\vec{P}$ are related by the expression^{69},

$$\vec{D} \propto \vec{P} \times \vec{R}_{21}, \tag{51}$$

where $\vec{R}_{12}$ is the relative position between two magnetic atoms shown in Fig 41. Therefore, it can be thought that the externally applied electric field in Pt may enable effective voltage control of *interfacial* DMI. I also calculate this electric polarization can be induced into our system by following Ref. 69. To demonstrate electric poralization, Katsura employed a system consisting of two magnetic ions with d-states and an intervening oxygen atom with a p-state. In their model, the *d*-states in the magnetic atoms possessed both exchange and spin-orbit couplings.

Here, we introduce an alternative model in which the intervening non-magnetic Pt atom possesses a large spin-orbit interaction. Figure 42 presents a schematic of the model. Two magnetic Fe atoms and an intervening Pt atom make a linear chain along the

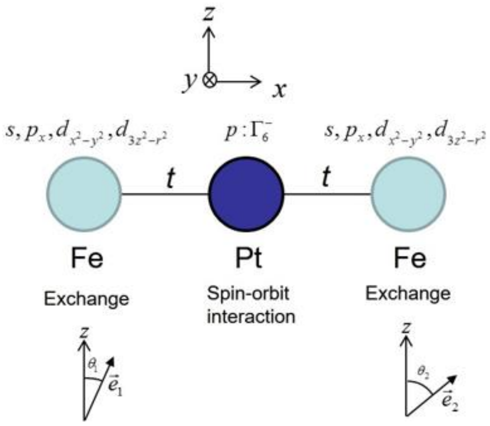

Figure. 42 Model to calculate electric polarization induced by the spatial inversion symmetry broken

x-axis. For this case, because central symmetry exists, the size of DMI is zero. In this system, I apply an electric field to produce DMI, as was done in my experiment. In the experiment, Pt was positioned 1 ML (monatomic layer) above the top-most Fe atomic layer. For this case, the system should produce DMI without an electric field. In my model, however, I put Pt between Fe atoms to clarify the role of the electric field.

Empty 6*p*-states with large spin-orbit interaction and zero-spin polarization are taken as the non-perturbative electronic states in Pt. The lowest level in the spin-orbit split empty states are doubly degenerated Γ6- states: $\{-(x+iy)\beta - z\alpha, (x-iy)\beta - z\alpha\}$. Here, α and β are the spin functions with spins parallel and antiparallel to the *z*-axis, respectively. Hybridization of the p_x and p_z states will cause coupling between double exchanges and electric polarization in the *z*-direction. As electronic state, *s*, p_x, $d_{x2\text{-}y2}$, and $d_{3z2\text{-}r2}$ states in Fe can be taken and is even functions in the *y-z* plane. Those states have a non-vanishing transfer integral, t, with Pt: p_x orbital in the Γ_6^- states. In Fe, I assume large exchange interactions with atomic spin moments but with zero spin-orbit interaction. The directions of the atomic spin moments in two Fe atoms are represented by two unit vectors, $\vec{e}_1$ and $\vec{e}_2$. Without transfer, the spins in the above mentioned Fe electronic state are parallel to the atomic spin moment. Those states in each Fe atom degenerate and stay at lower energies by Δ relative to the Γ_6^- states.

After performing similar perturbation calculations to those carried out by Katsura et al. eq. 52, we obtained electric polarisation

$$\langle \vec{P} \rangle = -\frac{2etd}{\Delta}\frac{\vec{e}_{12}\times(\vec{e}_1\times\vec{e}_2)}{|\cos(\theta_{12}/2)|}, \tag{52}$$

where, *e* is the elementary charge, *d* is the dipole integral, $\vec{e}_{12}$ is the unit vector parallel to a displacement from the first Fe to the second Fe. θ_{12} is the relative angle between spins in the first Fe and those in the second Fe, defined as $\theta_{12} = \theta_2 - \theta_1$. The result is essentially identical with Katsura's expression (Eq. (4) in Ref. 69]), although the atom with large spin-orbit interactions changed from a magnetic atom to a non-magnetic atom. The DMI energy can be estimated from dielectric dipole energy using

$$E_{DMI} = -\vec{E}\cdot\langle \vec{P} \rangle = \frac{2etd}{\Delta}\frac{\vec{E}\cdot(\vec{e}_{12}\times(\vec{e}_1\times\vec{e}_2))}{|\cos(\theta_{12}/2)|}, \tag{53}$$

This result means that DMI can be induced by an application of an electric field to non-magnetic atoms with large spin-orbit interactions. It should be noted that, in this mechanism, a magnetic polarization of Pt is not necessary[45], in contrast with previous report[44]. In addition, I found that the atoms may share their roles to make large DMI, such that (i) large exchange interactions occur in the magnetic atoms and (ii) large spin-orbit interactions and electric polarization occur in adjacent non-magnetic atom.

It also should be noted that a displacement of Pt atom positions by an application of an electric field causes modulations in DMI[70]. The relative significance of these two mechanisms should be examined by further experiments and theoretical calculations.

I also studied Pt layer thickness dependence to investigate how thick Pt can enhance voltage induced *interfacial* anisotropy change and *interfacial* DMI change most effectively. The artificial multilayer was prepared by using molecular beam epitaxy method in Osaka University. The film stack is MgO (substrate)|MgO (5 nm)|V (30 nm)|Fe(20 nm)|Pt(0.1, 0.2, 0.4, 0.8 nm)|MgO(5 nm)|SiO_2(5 nm). The device structure is same as previous study. Figure. 42 shows the Pt thickness dependence of voltage-induced frequency shift. The green and blue plots express the frequency shift δf_{21} and δf_{12}, respectively. Open circle, square, triangle and rhombus show the result obtained in Pt-thickness 0.1 nm, 0.2 nm, 0.4 nm and 0.8 nm. As shown in Fig. 26, the largest voltage

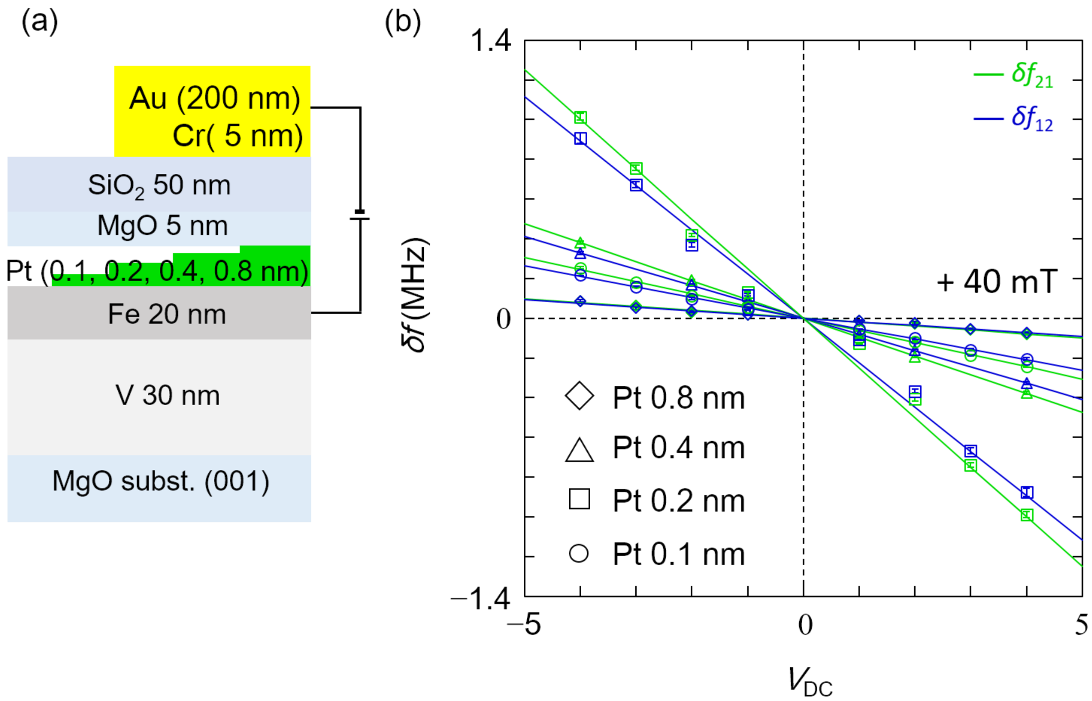

Figure. 43 Pt layer thickness dependence of the voltage-induced frequency shift. (a) Schematic image of voltage application for the film stack. (b) Voltage induced frequency shift for each Pt thickness obtained at external magnetic field + 40 mT. The data shown by green (blue) are the obtained frequency shift of S_{21} (S_{12}). Open circle, square, triangle and rhombus correspond to the result of Pt-thickness 0.1 nm, 0.2 nm, 0.4 nm and 0.8 nm. The largest voltage-induced frequency shift was obtained in Pt thickness 0.2 nm and the smallest voltage-induced frequency shift was obtained in Pt thickness 0.8 nm.

induced frequency shift was obtained in Pt-thickness 0.2 nm and the smallest voltage-induced frequency shift was obtained in Pt-thickness 0.8 nm sample. This result means that one-monolayer Pt can enhance two voltage-induced frequency shift most effectively. Figure 44 (a)-(c) show the results of *interfacial* anisotropy in (a), voltage-induced

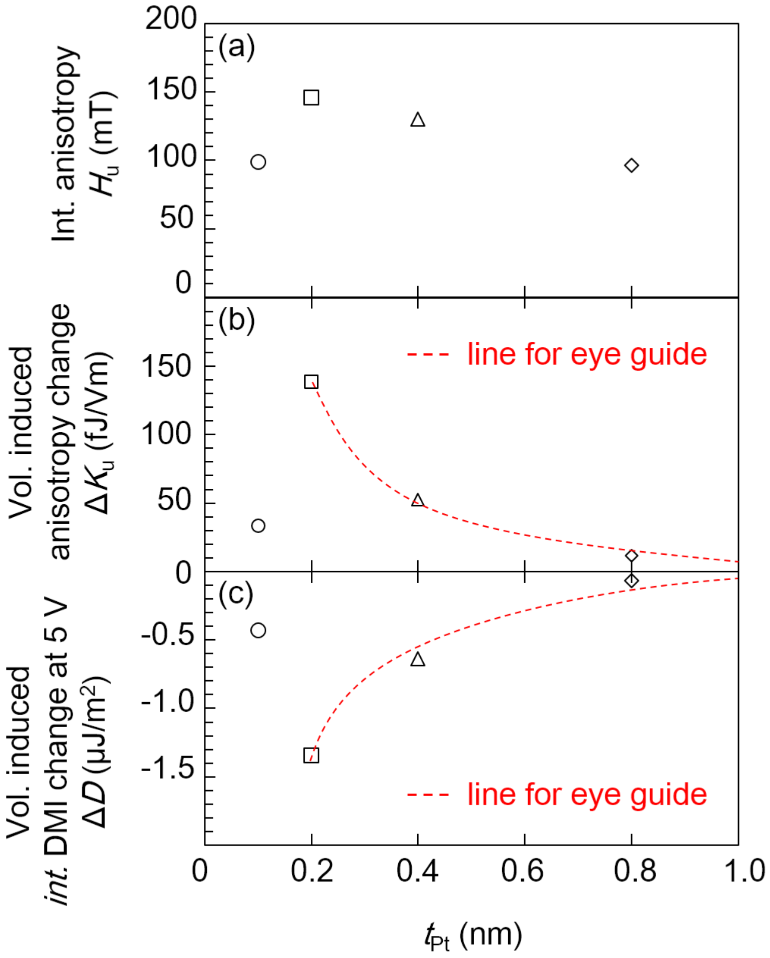

Figure. 44 Pt layer thickness dependence of *interfacial* anisotropy field, voltage-induced *interfacial* anisotropy change and voltage-induced *interfacial* DMI change. (a) Pt thickness dependence of *interfacial* anisotropy field. (b) Pt thickness dependence of voltage-induced *interfacia*l anisotropy energy change. (c) Pt thickness dependence of voltage-induced *interfacial* DMI change at 5 V. The red dot curves in (b) and (c) show the line for eye guide. The largest *interfacial* magnetic anisotropy and voltage effects were obtained in Pt-thickness 0.2 nm and smallest *interfacial* magnetic anisotropy and voltage effects were obtained in Pt-thickness 0.8 nm. These results imply that Fe|Pt interface is important for the voltage induced *interfacial* anisotropy change and *interfacial* DMI change and their results don’t contradict to the idea of electric-dipole excitation in Fe|Pt interface.

interfacial anisotropy energy change in (b) and voltage-induced *interfacial* DMI change in (c) as function of Pt thickness (t_{Pt}). The largest *interfacial* magnetic anisotropy and voltage effects, which are voltage induced *interfacial* magnetic anisotropy change and voltage induced *interfacial* DMI change, were obtained in Pt-thickness 0.2 nm and the smallest interfacial magnetic anisotropy and voltage effects were obtained in Pt-thickness 0.8 nm. The same tendency was obtained in each data, however, it can be explained in different mechanisms. First of all, for the case of interfacial magnetic anisotropy, the interfacial magnetic anisotropy can be induced by the interface of Fe|Pt and Pt|MgO. For the case of Pt|MgO, the induced *magnetic* dipole (*induced moment*) in Pt attributed to Fe plays a decisive role and its dipole is localized in Fe|Pt interface. Therefore, by increasing Pt thickness, interfacial anisotropy and voltage induced *interfacial* magnetic anisotropy may decrease. On the other hand, a Pt thickness dependence in voltage induced *interfacial* DMI may be attributed to different mechanism. The *interfacial* DMI can be induced by the *electric* dipole in Fe|Pt interface and it should localize in Fe|Pt interface. Therefore, by increasing a thickness of Pt, the voltage induced *interfacial* DMI change decreased. This idea doesn't contradict to the presented mechanism attributed to the induced electric dipole into Fe|Pt interface.

Thus, a Pt thickness dependence of these two voltage effects can be attributed to the localization of dipole. In the case of the interfacial anisotropy change, magnetic dipole plays decisive role and in the case of the interfacial DMI change, electric dipole plays decisive role. These dipole may correlate each other, however to understand the relation between them, the additional experiments and the help of numerical calculation is required. I succeeded in enhancement of two voltage effect in artificial multilayer by inserting just one monolayer Pt into an Fe|MgO interface.

6.4 Proposal for practical application (Voltage controlled excitation of skyrmions)

Finally, I now demonstrate the nucleation and annihilation of skyrmions by applying electric field in the sample. Here, excitation of Skyrmion can be controlled by perpendicular magnetic anisotropy and DMI. As shown above, voltage application can control perpendicular magnetic anisotropy and *interfacial* DMI, however, in this part, I only consider the effect attributed to the voltage induced *interfacial* DMI change. Fig. 45 shows micromagnetic simulations (see Appendix 4) that demonstrate nucleation and annihilation of skyrmions in a 0.5-nm Fe film under 300 mT along *z*-direction. Here, I used perpendicular magnetic anisotropy obtained from the previous studies[65] and voltage-induced *interfacial* DMI changes obtained from my studies obtained in Cr|Fe|Pt|MgO

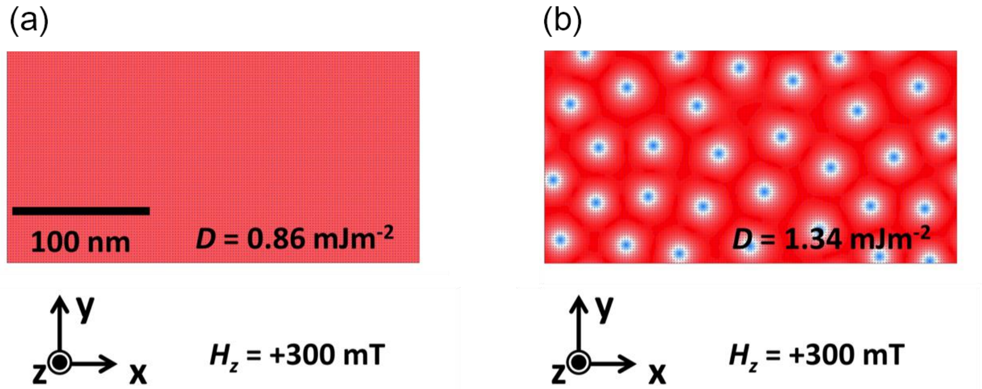

Figure. 45 The simulation results of skyrmion nucleation and annihilation by voltage induced *interfacial* DMI change in Fe 0.5 nm under perpendicular external magnetic field (300 mT).
(a) Voltage-induced annihilation of skyrmions by voltage induced *interfacial* DMI change. (b) Voltage-induced nucleation of slyrmions by voltage induced *interfacial* DMI change.

artificial multilayer. I employed *interfacial* DMI change of 0.24 mJm^{-2} for 1 V application to 1-nm-thick MgO barrier. The snapshot of the Skyrmion state is shown in Fig. 45. Fig. 45 (a) and (b) indicate the D = 0.86 mJm^{-2} and D = 1.34 mJm^{-2} of the system which assumed as applying -1 V and +1 V, respectively. If I apply -1 V with external magnetic field along z-direction, magnetic moments lie parallel to external magnetic field as shown in Fig. 45 (a). However, if +1 V is applied without changing external magnetic field, I found several features of skyrmions. First, each Skyrmion has the uniform lateral size and the similar distance. Second, whole Skyrmion exist with same Skyrmion number (m = 1, γ = 0). This simulation shows that a Fe|Pt|MgO junction with voltage induced *interfacial* DMI changes may provide voltage controllable skyrmion states.

6.5 Conclusion

In my research, I designed new artificial multilayer, where one monolayer Pt was inserted into Fe|MgO interface. By inserting one-monolayer Pt, I demonstrated the enhancement of voltage induced *interfacial* magnetic anisotropy change and voltage induced *interfacial* DMI change. I also present the the possible mechanism of voltage induced *interfacial* DMI change. Finally, I also show the one of the practical application of voltage induced *interfacial* DMI change; that is, voltage induced nucleation and annihilation of skyrmions in Fe 0.5 nm. These demonstration of enhancement and that of voltage-induced skyrmions control become the milestone of the new generation spintronics research.

Chapter 7. <u>Conclusion of total research</u>

Voltage induced *interfacial* Dzyaloshinskii-Moriya interaction in Fe|MgO is demonstrated by voltage-controlled spin-wave spectroscopy. In my research, voltage-induced *interfacial* DMI is observed through the propagation-direction dependent voltage-induced frequency shift. I also designed new artificial multilayer and succeeded in observing the enhancement of voltage-induced interfacial DMI by inserting one-monolayer Pt. Finally I showed voltage-control of nucleation and annihilation of skyrmions.

In the first study, I have studied the voltage control of propagating spin waves in a 5-nm-thickness Fe film. I succeeded in observing voltage modulation signal of propagating spin waves in an artificial multilayer for the first time in the world and found that voltage-modulation of propagating spin waves is attributed to the spin-wave resonant magnetic field shift. In this research, I selected magnetic field sweep technique to observe spin-wave spectra, therefore the signal-to noise ratio was not enough to observe the chirality dependent voltage effect; voltage-induced *interfacial* DMI change.

In the second study, I have studied the voltage-induced interfacial DMI change in an Au|Fe|MgO based artificial multilayer. By using VNA and constructing new lock-in technique with VNA, I succeeded in observing voltage-induced *interfacial* DMI change in an artificial multilayer for the first time in the world. To measure voltage-induced *interfacial* DMI change, I investigated the propagation-direction dependent, which corresponds to the chirality dependent, voltage-induced signal. Fe thickness dependence shows that voltage-induced propagation-direction dependent signal is inversely proportional to the Fe thickness. This thickness dependence declare that the experimentally obtained chirality-dependent signal corresponds to the voltage induced interfacial DMI change.

In the final study, I have studied one-monolayer-Pt-insertion effect for the voltage induced *interfacial* magnetic anisotropy change and voltage induced *interfacial* DMI change. By inserting one-monolayer Pt in to Fe|MgO interface, where external electric field can act on, voltage induced interfacial anisotropy change and voltage induced interfacial DMI change is enhanced by about a factor of three. Pt thickness dependence ensured that one monolayer Pt can enhance two voltage effects most effectively and doesn’t contradict the model fabricated in the chapter to explain the electric dipole induced between Fe and Pt. Finally I also show the idea of practical application of this voltage-induced *interfacial* DMI change; voltage-control of nucleation and annihilation of skyrmion.

Chapter 8. Appendix

In this chapter, I describe 3 appendixes part which are not described in the main manuscript; **correlation between wave number parallel to spin-wave propagation direction and that to normal to film plane**, **problem in double-lock-in-amplifier technique and its solution**, **influence of interface localization properties of MSSWs for voltage-induced frequency shift** and **simulation method to calculate voltage nucleation and annihilation of Skyrmions**.

8.1 Correlation between wave number parallel to spin-wave propagation direction and that to normal to film plane for anisotropic material

In this subsection, I describe the correlation between wave number parallel to spin-wave propagation direction and that to normal to film plane, which is attenuation length of spin waves. Here, I consider the ultra-thin single crystalline Fe. Therefore crystalline anisotropy (H_a), interfacial anisotropy (H_u) and shape anisotropy (M_0) should be considered. Each spin feel these anisotropy while precession, therefore the energy, obtained each spin with precession, can be described as following,

$$E_{\mathrm{Pr}e} = \frac{\mu_0}{2}\mathbf{m}\mathrm{e}^{-i\omega t}\mathbf{h}_{anisotropy} = \frac{\mu_0}{2}\mathbf{m}\mathrm{e}^{-i\omega t}\begin{pmatrix} h_a \\ h_a + M_0 + h_u \end{pmatrix}, \tag{54}$$

where I consider the same condition as chapter 2 except for anisotropy, E_Pre is an energy attributed anisotropy with precession and $\mathbf{h}_\mathrm{anisotropy}$ is a magnetic anisotropic field. Therefore, effective magnetic field (eq. (14)), which spins obtain with precession, can be revised as following,

$$\mathbf{H}_{effective} = H_0\hat{z} + \frac{1}{M_0}\begin{pmatrix} H_a \\ H_a + M_0 - H_u \end{pmatrix}\mathbf{m}e^{-i\omega t} + \mathbf{h}\mathrm{e}^{-\mathrm{i}\omega t}, \tag{55}$$

where $\mathbf{H}_\mathrm{effective}$ is a revised effective magnetic field. Then, by substituting eq. (55) to LL equation (eq. (15)), the relation between rotating magnetization and field can be described as following,

$$\mathbf{m} = \bar{\chi}\cdot\mathbf{h}$$
$$\bar{\chi} = \begin{pmatrix} \omega_y & -i\omega \\ i\omega & \omega_x \end{pmatrix}, \tag{56}$$

where, $\omega_\mathrm{x} = \gamma\mu_0(H_0 + H_a)$ and $\omega_\mathrm{y} = \gamma\mu_0(H_0 + H_\mathrm{a} + M_0 - H_\mathrm{u})$. Here, to simplify the

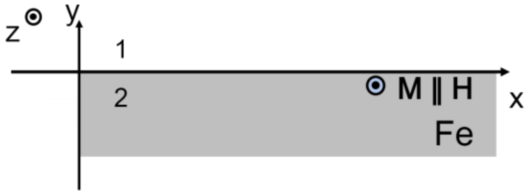

Figure. 46 Geometry for the simplified calculation of attenuation length for *y* axis

calculation, region 1 and 2 depicted in Fig. (46) are only considered. Then, the scalar potential for each region can be obtained as following,

$$\psi_1 = \psi_1 \mathrm{e}^{\mathrm{i}\nu k_1 x - k_1 y} \text{ (in the region 1),} \tag{57}$$

$$\psi_2 = \psi_2 \mathrm{e}^{\mathrm{i}\nu k_x x - k_y y} \text{ (in the region 2),} \tag{58}$$

Then, the boundary condition at $y = 0$ can be applied to the scalar potentials (eq. (57) and eq. (58)) and magnetic field calculated by eq. (13).

$$\psi_1 = \psi_2 \text{ (for scalar potential),} \tag{59}$$

$$k_1 \psi_1 = -k_y \psi_2 + m_y \text{ (for magnetic field),} \tag{60}$$

where, m_y is a y component of precessing magnetization term. Then, by using substituting ψ_1 of eq. (60) for ψ_1 by using eq. (59), the following equation can be obtained,

$$\psi_2 = \frac{m_y}{k_1 + k_y}. \tag{61}$$

Then, eq. (56) can be replaced magnetic field with the scalar potential and using eq. (21) as following,

$$\mathbf{m} = \overline{\chi} \begin{pmatrix} -i\nu k_1 \\ -k_y \end{pmatrix} \psi_2. \tag{62}$$

Here, by calculating the divergence part in eq. (13), following relation can be obtained

$$\begin{aligned} \nabla \cdot \mathbf{b} &= 0 \\ &= \mu_0 \left(\left(k_x{}^2 - k_y{}^2 \right) \psi_2 + i\nu k_x m_x + k_y m_y \right) \end{aligned} \tag{63}$$

Then, by substituting m_x and m_y of eq. (63) by them obtained in eq. (62), following relation between wave number of propagating spin waves (k_1) and attenuation length to film thickness direction (k_y) as following,

$$k_y = \sqrt{\frac{\omega_y \left(\omega_x + \omega_M \right) - \omega^2}{\omega_x \left(\omega_y + \omega_M \right) - \omega^2}}\, k_1. \tag{64}$$

where, $\omega x =$ the ω is the resonant angular momentum of MSSW, therefore, by using eq. (64) we can calculate the attenuation length of spin waves to the film thickness direction. Here, the difference between numerator and denominator in eq. (64) is $\omega_y\omega_M$ and $\omega_x\omega_M$. By inserting parameter obtained in the chapter 4-6, then the attenuation length k_y is estimated to be 2.3- 4.2 μm^{-1}. Therefore, for the case of ultra-thin film, because of large diamagnetic field, strictly speaking, attenuation length and propagation length is not same. However, it is same order, and its little change doesn’t seriously affect to magnetic property. Therefore, we neglect its change.

8.2 Problem in double-lock-in technique and its solution

In this appendix, I describe the problem in double-lock-in technique and its solution. For the measurement by using lock-in amplifier, we have to take care the relation between modulation frequency (f_{mod}) and time constant (t_{const}). If time constant is less than $3/f_{\mathrm{mod}}$, we cannot obtain true value. In the double lock-in measurement, where two lock-in amplifier with different frequency are used, the relation between time constant ($t_{\mathrm{const,1}}$) of first lock-in amplifier (large modulation frequency) and modulation frequency ($f_{\mathrm{mod,2}}$) of second lock-in amplifier (small modulation frequency) is also important. Here, for the case of long $t_{\mathrm{const,1}}$ compared with modulation frequency $f_{\mathrm{mod,2}}$, then the data point for the second lock-in amplifier decrease. Therefore, true value cannot obtained in lock-in amplifier. In the following, I studied the relation between them. To study the shift between true value and obtained data, I constructed a setup shown in Fig. 47. In this study, I selected an optical kerr effect measurement (MOKE). The emitted laser light is amplitude-modulated in 42 kHz by using photoelectric modulator and in 17-213 Hz by using optical chopper. Then the laser light is irradiated into perpendiculary magnetized film (Si|SiO$_2$ substrate|Ta (5 nm)|CoFeB (1.1 nm)|MgO (2 nm)|Ta (2 nm)) and reflected signal is detected in first lock-in amplifier and in second lock-in amplifier through the photo detector. The time constant of first lock in amplifier is changed from 30 to 3,000 μs and that of second lock-in amplifier is fixed into 1 s. Then, the intensity of magnetization curve obtained in second lock in amplifier was measured as depicted in

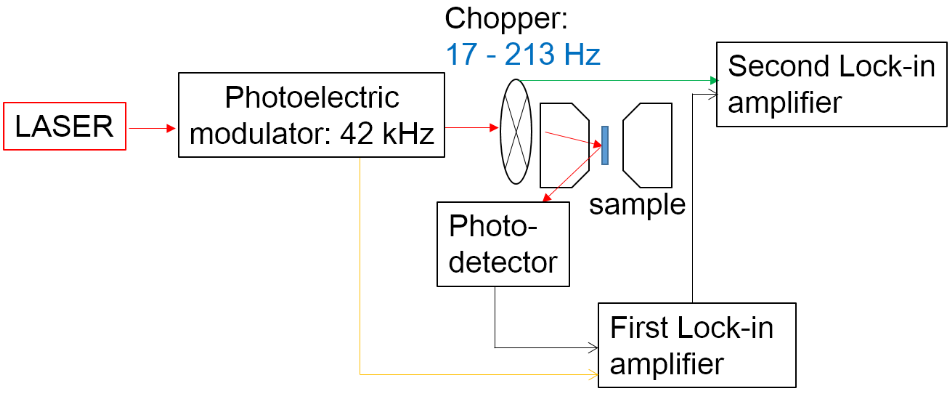

Figure. 47 Measurement set up to study the property of double lock-in technique. The emitted laser light was amplitude-modulated in 42 kHz by using phototelectric modulator and in 17-213 Hz by using optical-chopper. Then laser light is irradiated to the sample, which is perpendiculary magnetized film, and its reflected signal was detected by first lock-in amplifier and second lock-in amplifier through the photo-detector

inset of Fig. 48. A horizontal axis is data points per a period calculated by $1/(f_{\mathrm{mod},2}\times t_{\mathrm{const},1})$. The black, blue, green and red colored data points were obtained in $t_{\mathrm{const},2}$ = 3000 , 1000, 300 and 100 μs, respectively. Because of bad signal to noise ratio in $t_{\mathrm{const},1}$ =30 μs, these data are not shown here. By increasing data points per a period, MOKE intensity A obtained in second lock-in amplifier increased, and around 90, the signal almost saturated. The signal obtained around dips is obtained in the condition of $f_{\mathrm{mod},2} \approx 60$ Hz, matching to the notch filter frequency. Here, the measurement condition selected in Chapter 4 is depicted as red star. Therefore, to correct the experimentally obtained data to the true value, we have to multiply a factor of 116. To perform double-lock-in technique in saturated condition is not usually recommended, since the signal to noise ratio in first lock in amplifier may decrease and low speed measurement attributed to low modulation frequency, such as 17 Hz, may affect to the measurement because of time dependent change, for example.

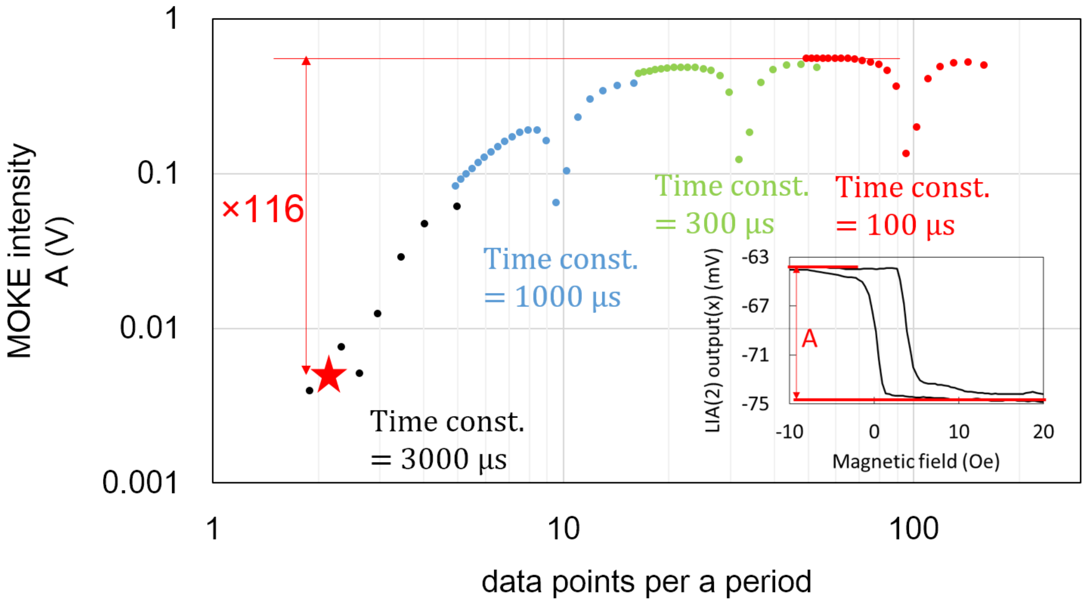

Figure. 48 Relation between MOKE intensity of second lock-in amplifier and data points per a period.

The relation MOKE intensity obtained in second lock-in amplifier and data points per a period. The data points per a period was calculated by $1/(f_{\mathrm{mod},2}\times t_{\mathrm{const},1})$. By increasing data points per a period, MOKE intensity increased and it was saturated about 90. The signal obtained around dips is obtained in the condition of $f_{\mathrm{mod},2}\approx 60$ Hz, matching to the notch filter frequency. The measurement condition of chapter 4 is plotted with red star, therefore to obtain the true value, we have to multiply 116 for the experimentally obtained data.

8.3 Influence of interface localization properties of MSSWs for voltage-induced frequency shift

In this subsection, for the case of an Au|Fe|MgO system, a mechanism for chirality-dependent frequency shifts induced by voltage, especially those caused by the localization of a magneto-static surface spin waves **(**MSSW) at the top or bottom interfaces together with interfacial anisotropy changes.

An Fe thin film is sandwiched by MgO and Au as shown in Fig. SII-1. We assume that the surface anisotropy appears only at the Fe|MgO interface. Therefore, the averaged interface anisotropy energy exerted on the MSSW propagating toward the ± x-direction can be approximated by

$$\frac{\mu_0}{2} M_{\mathrm{S}} H^{\mp}{}_{\mathrm{u}} = K_{\mathrm{u}} \frac{\int d^3 \delta(y) e^{\mp \kappa_y y}}{\int d^3 e^{\mp \kappa_y y}}, \tag{54}$$

where $H^{\mp}{}_{\mathrm{u}}$ is the averaged interfacial anisotropy field for the MSSW propagating toward the ± x-direction, K_{u} is the interfacial magnetic anisotropy energy and κ_{y} is the attenuation coefficient of the MSSW. This treatment enables us to expand the idea of the interface anisotropy field, H_{u}, to the inhomogeneous MSSW case. From Eq. (54), we can calculate the voltage-induced interfacial anisotropy field change δH_{u} as

$$\delta H_{\mathrm{u}} = \frac{2\delta K_{\mathrm{u}}}{\mu_0 M_{\mathrm{S}}} \left[\frac{\mp \kappa_{\mathrm{y}}}{\mathrm{e}^{\mp \kappa_y t_{\mathrm{Fe}}} - 1} \right], \tag{55}$$

where δK_{u} is the voltage-induced interfacial anisotropy energy change. Here, by using Eq. (55), we expand the voltage-induced frequency shift as a function of δK_{u}. The expanded voltage-induced frequency shift can be calculated as,

$$\delta f = \frac{\gamma}{2\pi} \frac{|H_0| + H_{\mathrm{a}} + \frac{M_{\mathrm{S}}}{2}|k| t_{Fe}}{2H_{\mathrm{MSSW}}} \frac{2\delta K_{\mathrm{u}}}{\mu_0 M_{\mathrm{S}}} \frac{\mp \kappa_y}{e^{\mp \kappa_y t_{\mathrm{Fe}}} - 1}, \tag{56}$$

where $H_{\mathrm{MSSW}} = (|H_0| + H_{\mathrm{a}})(|H_0| + M_{\mathrm{S}} + H_{\mathrm{a}} - H_{\mathrm{u}}) + \frac{M_{\mathrm{S}}}{4}(M_{\mathrm{S}} - H_{\mathrm{u}})(1 - \exp(-2|k|t_{\mathrm{Fe}}))$. To study the contribution of interfacial anisotropy changes to the voltage-induced chirality-dependent frequency shift, we neglect the term depending on the interfacial DMI change. Here, we divide this frequency shift into two components; one is the propagation-direction independent shift δf_{Sym}, and the other is propagation-direction dependent shift δf_{Asym}:

$$\delta f_{\mathrm{Sym}} = \frac{\gamma}{2\pi} \frac{|H_0| + H_{\mathrm{a}} + \frac{M_{\mathrm{S}}}{2}|k|t_{Fe}}{2H_{\mathrm{MSSW}}} \frac{2\delta K_{\mathrm{u}}}{\mu_0 M_{\mathrm{S}}} \frac{1}{t_{\mathrm{Fe}}}, \tag{57}$$

and

$$\delta f_{\mathrm{Asym}} = \frac{\gamma}{2\pi} \frac{|H_0| + H_{\mathrm{a}} + \frac{M_{\mathrm{S}}}{2}|k|t_{Fe}}{2H_{\mathrm{MSSW}}} \frac{2\delta K_{\mathrm{u}}}{\mu_0 M_{\mathrm{S}}} \frac{\kappa_{\mathrm{y}}}{2}, \tag{58}$$

In the case of a magnetically isotropic sample, the attenuation coefficient for the *y*-direction equals the wavenumber for the *x*-direction. Strictly speaking, our sample is magnetically anisotropic; however, we can approximate $\kappa_{\mathrm{y}} \cong k$ as introduced in appendix 1; because of small magnetic anisotropy. The ratio of the propagation direction-dependent frequency shift δf_{Asym} to the propagation direction-independent frequency shift δf_{Sym} is calculated with

$$\frac{\delta f_{\mathrm{Asym}}}{\delta f_{\mathrm{Sym}}} = \frac{\kappa_{\mathrm{y}} t_{\mathrm{Fe}}}{2} = 1.2\,\%, \tag{59}$$

for Fe with 20 nm thickness. In contrast, the experimentally obtained ratio is 6.7%, as shown in Fig. 34. The experimentally obtained propagation direction-dependent frequency shift is five times larger than the estimate obtained by using Eq. (59). In addition, the calculated propagation direction-dependent frequency shift, Eq. (59), is larger for thicker Fe thickness, as shown by the dotted red curve in Fig. 34. On the other hand, the experimentally obtained frequency shift is smaller for thicker Fe thicknesses. These results corroborate that observation that experimentally obtained propagation direction-dependent frequency shifts are attributable not to the voltage-induced interfacial anisotropy change but to the *interfacial* DMI change.

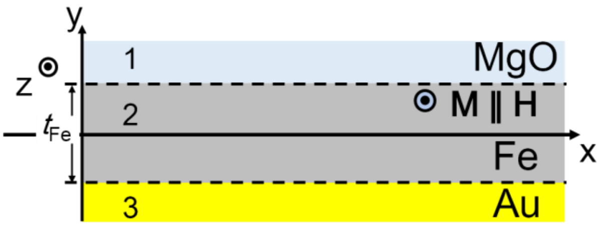

Figure. 46 Geometry for the analysis of propagation-direction dependent frequency shift attributed to the interface localization property of MSSW. In this calculation I only consider Fe|MgO *interfacial* anisotropy change.

8.4 Simulation method to calculate voltage nucleation and annihilation of Skyrmions

The micromagnetic simulations were carried out using the Object oriented micromagnetic framework (OOMMF)[71] with additional *interfacial* DMI Hamiltonian[72]. In order to ignore the dipole interaction form boundaries, I applied 2-dimensional periodic boundary condition (PBC) for the dipole-dipole interaction, the Heisenberg exchange interaction[73], and furthermore PBC for *interfacial* DMI energies in my homemade extension module for OOMMF[74]. We took the material parameters of Fe the saturation magnetization M_s = 2140 mT, the exchange stiffness constant A_{ex} = 5.0 pJm^{-1} and Gilbert damping constant α of 0.5. The perpendicular magnetic anisotropy energy K = 1.52 MJm^{-3} where thickness of 0.5-nm-thick Fe[65]. The voltage-induced *interfacial* DMI changes ΔD = ±0.24 mJm^{-2} for ± 1 V application. Build-in *interfacial* DMI value is assumed to be D = 1.10 mJm-2 under 0 bias voltage to bring the system to the border of skyrmion formation transition. The rectangular pad of 300 × 200 nm^2 with the 1 × 1 × 0.5 nm^3 cell size was considered with 2-dimensional PBC. I set the initial magnetization to the random direction which corresponds to high temperature state, and relax the spins with constant voltage under an external magnetic field of 300 mT along perpendicular to the plane. After 20 ns, I assumed the system reaches energy minimum, I save the spin configurations. All simulations were performed without stochastic field.

REFERENCES

1. Thomson, W. On the Electro-Dynamic Qualities of Metals:--Effects of Magnetization on the Electric Conductivity of Nickel and of Iron Proc. Roy. Soc. (London), 8, 546 (1857).
2. Julliere. M. Tunneling between ferromagnetic films. Phys. Rev. Lett., **54**A, 225 (1975).
3. Mcguire T. R. and Potter I. Anisotropic Magnetoresistance in Ferromagnetic 3d Alloys. IEEE Trans. Magn. **MAG-11**, 1018 (1975).
4. M. N. Baibich, et al., Giant Magnetoresistance of (001)Fel(001)Cr Magnetic Snperlattices. Phys. Rev. Let. **61**, 2472 (1988).
5. Binasch, G. et al., Enhanced magnetoresistance in layered magnetic structures with antiferromagnetic interlayer exchange. Phys. Rev. B, **39**, 4828 (1989).
6. T. Miyazaki and N. Tezuka, J. Giant magnetic tunneling effect in Fe/AlzO3/Fe junction. Magn. Magn, Mater., **139**, L231(1995).
7. Moodera, J. S., et al., Large Magnetoresistance at Room Temperature in Ferromagnetic Thin Film Tunnel Junctions. Phys. Rev. Lett., 74, 3273 (1995).
8. Bulter, W. H. et al., Spin-dependent tunneling conductance of Fe/MgO/Fe sandwiches. Phys. Rev. B, **63**, 054416 (2001).
9. Mathon, J. and Umerski, A. Theory of tunneling magnetoresistance of an epitaxial Fe/MgO/Fe(001) junction. Phys. Rev. B, **63**, 220403 (2001).
10. Yuasa, S, et al., High Tunnel Magnetoresistance at Room Temperature in Fully Epitaxial Fe/MgO/Fe Tunnel Junctions due to Coherent Spin-Polarized Tunneling. Jpn. J. Appl. Phys., **43**, L588 (2004).
11. Yuasa, S, et al., Giant room-temperature magnetoresistance in single-crystal Fe/MgO/Fe magnetic tunnel junctions. Nat. Mater., **3**, 868(2004).
12. Parkin, S. S., et al., Giant tunnelling magnetoresistance at room temperature with MgO (100) tunnel barriers. Nat. Mater., **3**, 862 (2004).
13. Novosad, V. et al., Novel magnetostrictive memory device. J. Appl. Phys. **87**, 6400 (2000).
14. Chiba, D., et al., Electric-field control of ferromagnetism. Nature, **408**, 944 (2000)
15. Chiba, D., et al., Electrical manipulation of magnetization reversal in aferromagnetic semiconductor. Science **301**, 943 (2003).
16. Kimura, T., et al., Magnetic control of ferroelectric Polarization. Nature 426, 55 (2003)
17. Wang. J, et al., Epitaxial BiFeO$_3$ multiferroic Thin Film Heterostructures. Science

299, 1719 (2003).

18. Yamasaki, Y., et al., Electric Control of Spin Helicity in a Magnetic Ferroelectric. Phys. Rev. Lett. **98**, 147204 (2007).
19. Weisheit, M., et al., Electric field-induced modification of magnetism in thin-ferromagnets. Science **315**, 349 (2007).
20. Maruyama, T., et al., Large voltage-induced magnetic anisotropy change in a few atomic layers of iron. Nat. Nanotech. **4**, 158–161 (2009).
21. Shiota, Y., et al., Quantitative evaluation of voltage-induced magnetic anisotropy change by magnetoresistance measurement Appl. Phys. Exp. **4**, 043005 (2011).
22. Shiota, Y., et al., Induction of coherent magnetization switching in a few atomic layers of FeCo using voltage pulses. Nat. Matter. **11**, 39 (2012).
23. Dzyaloshinskii, I. E. Thermodynamic theory of weak ferromagnetism in antiferromagnetic substances. Sov. Phys. JETP **5**, 1259-1541(1957).
24. Moriya, T. Anisotropic superexchange interaction and weakferromagnetism. Phys. Rev. **120**, 91-98(1960)
25. Fert, A. & Levy, P. M. Role of Anisotropic Exchange Interactions in Determining the Properties of Spin-Glasses. Phys. Rev. Lett. 44, 1538 (1980)
26. Coffey, D., et al., Dzyaloshinskii-Moriya interaction in the cuprates. Phys. Rev. B. 44, 10112 (1991)
27. Zhao, J. Z., et al., Effects of the Dzyaloshinskii-Moriya Interaction on Low-Energy Magnetic Excitations in Copper Benzoate. Phys. Rev. Lett. 90, 207204 (2003)
28. Sergienko, I. A. & Dagotto, E. Role of the Dzyaloshinskii-Moriya interaction in multiferroic perovskites. Phys. Rev. B. **73**, 094434 (2006).
29. Mühlbauer, S., et al. Skyrmion lattice in a chiral magnet. Science **323**, 915 (2009).
30. Bode, M., et al. Chiral magnetic order at surfaces driven by inversion asymmetry. Nature **447**, 190-193 (2007).
31. Zakeri, Kh., et al., Asymmetric Spin-Wave Dispersion on Fe(110): Direct Evidence of the Dzyaloshinskii-Moriya Interaction. Phys. Rev. Lett., **104**, 137203 (2010).
32. Zakeri, Kh., Magnon Lifetimes on the Fe(110) surface: The Role of Spin-Orbit Coupling. Phys. Rev. Lett., **108**, 197205 (2012).
33. Cho, J., et al., Thickness dependence of the interfacial Dzyaloshinskii-Moriya interaction in inversion symmetry broken system. Nat. Commun., **6**, 7635 (2015).
34. Di, K., Direct observation of the Dzyaloshinskii-Moriya interaction in a Pt/Co/Ni film. Phys. Rev. Lett., **114**, 047201 (2015).
35. Bailleul, M., et al., Spin waves propagation and confinement in conducting films at the micrometer scale. Euro. Phys. Lett. **56**, 741 (2001).

36. Nembach, H. T., Linear relation between Heisenberg exchange and interfacial Dzyaloshinskii-Moriya interaction in metal films. Nat. Phys. **11**, 825 (2015).
37. Lee, J. M., et al., All electrical measurement of interfacial Dzyaloshinskii-Moriya interaction using collective spin-wave dynamics. Nano. Lett., **16**, 62 (2016).
38. Gladii, O., et al., Frequency nonreciprocity of surface spin wave in permalloy thin films. Phys. Rev. B., **93**, 054430 (2016)
39. Thiaville, A., et al., A. Dynamics of Dzyaloshinskii domain walls in ultrathin magnetic films. Europhys. Lett. 100, 57002 (2012).
40. Ryu, K.-S., et al., Chiral spin torque at magnetic domain walls. Nat. Nanotech. 8, 527–533 (2013).
41. Emori, S., et al., Current-driven dynamics of chiral ferromagnetic domain walls. Nat. Mater. 12, 611–616 (2013).
42. Torrejon J., et al., Interface control of the magnetic chirality in CoFeB/MgO heterostructures with heavy-metal underlayers Nat. Commun. **5**, 4655 (2014).
43. Yoshimura, Y., et al., Soliton-like magnetic domain wall motion induced by the interfacial Dzyaloshinskii–Moriya interaction. Nat. Ohys. 12, 157 (2016)
44. Ryu, K.-S., et al., Chiral spin torque arising from proximity-induced magnetization. Nat. Commun. **5**, 4910 (2014).
45. Yang, H., et al., M. Anatomy of Dzyaloshinskii–Moriya Interaction at Co/Pt Interfaces. Phys. Rev. Lett. **115**, 267210 (2015).
46. Yi, S. D., et al., Skyrmions and anomalous Hall effect in a Dzyaloshinskii-Moriya spiral magnet. Phys. Rev. B **80**, 054416 (2009).
47. Mühlbauer, S., et al., Skyrmion Lattice in a Chiral Magnet. Science **323**, 915 (2009)
48. Yu, X. Z., et al., Real-space observation of a two-dimensional skyrmion crystal. Nature **465**, 901 (2010).
49. Heinze, S., et al., Spontaneous atomic-scale magnetic skyrmion lattice in two dimensions. Nat. Phys. **7**, 713 (2011).
50. Parkin, S. S. P., *et al*., Magnetic domain-wall racetrack memory. Science **320**, 190 (2008).
51. Sampaio, J., et al., Nucleation, stability and current-induced motion of isolated magnetic skyrmions in nanostructures. Nat. Nanotechnol. **8**, 839 (2013).
52. Hsu, P.-J., et al., Electric field driven switching of individual magnetic skyrmions. arXiv: 1601.02935 (2016).
53. Schott, M., et al., Electric field control of skyrmion bubbles stability and switching at room temperature. arXivs: 1611.01453 (2016).
54. Landau, L. and Lifshits, E. On the theory of the dispersion of magnetic permeability

in ferromagnetic bodies. Phys, Zeitsch, Sow. **8**, 153 (1935)

55. Serga, A. A., *et al.*, YIG magnonics. J. Phys. D: Appl. Phys **43**, 264002 (2010).
56. Walker, L. R. Resonant modes of ferromagnetic spheroids. J. Appl. Phys. **36**, 3453 (1958).
57. Stancil, D. D. and Prabhakar, A. Spin waves: Theory and Application (Springer, New York, 2009).
58. Vlaminck, V. & Bailleul, M. Current-induced Spin-Wave Doppler Shift. *Science*. **322**, 410-413 (2008).
59. Kajiwara, Y., *et al.* Transmission of electrical signals by spin-wave interconversion in a magnetic insulator. *Nature* **464**, 262-267 (2010).
60. Kalinikos, B. A. *et. al.*, The dipole-exchange spin wave spectrum for anisotropic ferromagnetic films with mixed exchange boundary conditions. J. Phys. Condens. Matter. **2** 9861 (1990).
61. Moon, J.-H., *et al.*, Spin-wave propagation in the presence of interfacial Dzyaloshinskii–Moriya interaction. Phys. Rev. B. **88**, 184404 (2013).
62. Vlaminck, M. and Bailleul, M. Spin-wave transduction at the submicrometer scale: Experiment and modeling. Phys. Rev. B. **81**, 014425 (2010).
63. Demidov, V. E., *et al.* Excitation of microwaveguide modes by a stripe antenna. *Appl. Phys. Lett*. **95**. 112509 (2009).
64. S. Chikazumi, *Physics of Ferromagnetism* (Oxford Science, 1997).
65. Tanaka, K., et al., Large voltage-induced magnetic anisotropy change in ferromagnetic FeGd. Appl. Phys. Exp. **8**, 073007 (2015).
66. Bonell, F., et al., Reversible change in the oxidation state and magnetic circular dichroism of Fe driven by an electric field at the FeCo/MgO interface. Appl. Phys. Lett. **102**, 152401 (2013).
67. Bi, C., et al., Reversible Control of Co Magnetism by Voltage-Induced Oxidation. Phys. Rev. Lett. **113**, 267202 (2014).
68. U. Bauer, et al., Magneto-ionic control of interfacial magnetism. Nat. Mater. **14**, 174 (2015).
69. Katsura, H et al., Spin current and magnetoelectric effect in noncollinear magnets. Phys. Rev. Lett. **95**, 057205 (2005)
70. Kashid, V., et al., Dzyaloshinskii–Moriya interaction and chiral magnetism in 3d−5d zigzag chains: Tight-binding model and ab initio calculations. Phys. Rev. B **90**, 054412 (2014).
71. Donahue, M. J. & Porter, D. G. OOMMF User’s Guide Version 1.0. Interagency Report NISTIR 6376 (National Institute of Standards and Technology 1999).

72. Rohart, R. and Thiaville, A., Skyrmion confinement in ultrathin film nanostructures in the presence of Dzyaloshinskii-Moriya interaction, Phys. Rev. B **88**, 184422 (2013).
73. Wang, W., et al., Two-dimensional periodic boundary conditions for demagnetization interactions in micromagnetics, Comput. Mater. Sci. **49**, 84-87 (2010).
74. You, C.-Y., Kim, N.-H., Critical Dzyaloshinskii-Moriya interaction energy density for the skyrmion states formation in ultrathin ferromagnetic layer, Cur. Appl. Phys. **15**, 298-301 (2015).

ACKNOWLEDGEMENT

First of all, I would like to extend my sincere gratitude to my supervisors, Dr. Prof. Suzuki (Professor in Osaka University) and Dr. Assoc. Prof. Miwa (Associate professor in Osaka University). From Dr. Prof. Suzuki, I learned a lot of things, such as how to use experimental equipment like VNA and MOKE, how to measure true data, how to analyze data and also how to consider something physically. From Dr. Assoc. Prof. Miwa, I also learned a lot of thing, such as how to use almost all experimental equipments, how to design experiment, how to make good presentation slide and how to write e-mail. Without their instruction, I never write this doctor thesis.

I would also like to thank Dr. Shiota for his kind instruction about film deposition by MBE, microfabrication and basic theory of spin waves. Because of his previous study about spin waves, I succeeded in measuring voltage modulation of propagating spin waves and measuring voltage induced *interfacial* DMI change.

I would like to appreciate Dr. Nozaki and Dr. Yuasa(researchers in AIST). Because of their good quality film, I succeeded in obtaining good results.

I would also like to Dr. Cho (researcher in Osaka University). Because of his very kind help, I can survive in Inha University in South Korea, and also because of his knowledge about spin waves, micro-magnetic simulation, *interfacial* DMI and coffee, I can develop my understanding of them and succeeded in obtaining the voltage control of skyrmion states attributed to voltage induced *interfacial* DMI change.

I would also like to appreciate Dr. Prof. Tamura, Dr. Assis. Prof. Goto, Dr. Tomita, Dr. Konishi, Dr. Doi, Dr, Shimo-Oka, Dr, Prof. Shinjo, Dr. Prof. You, Mr. Fukumoto, Mr. Kobayashi, my parents and brother. Without one of them, I also never finish writing this doctor thesis.

LIST OF PUBLICATIONS

Names written with an underline represents the thesis author
(① Authors, ② Title, ③ Journal, ④ Vol., No, pp. -, and Year.)

(1) ① Kohei Nawaoka, Yoichi Shiota, Shinji Miwa, Hiroyuki Tomita, Norikazu Mizuochi, Teruya Shinjo, Yoshishige Suzuki
② Voltage modulation of propagating spin waves in Fe
③ Journal of Applied Physics
④ **117**, 17A905-1 - 17A905-3 (2015)

(2) ① Kohei Nawaoka, Shinji Miwa, Yoichi Shiota, Norikazu Mizuochi, Yoshishige Suzuki
② Voltage induction of interfacial Dzyaloshinskii-Moriya interaction in Au/Fe/MgO artificial multilayer
③ Applied Physics Express
④ **8**, 063004-1 - 063004-4 (2015)

(3) ① Shohei Hatanaka, Shinji Miwa, Kensho Matsuda, Kohei Nawaoka, Kazuhito Tanaka, Hiroki Norishita, Monori Goto, Norikazu Mizuochi, Teruya Shinjo, Yoshishige Suzuki
② Tunnel anisotropic magnetoresistance in CoFeB|MgO|Ta junctions
③ Applied Physics Letter
④ **107**, 082407-1 - 082407-4 (2015)

(4) ① Dongseok Kim, Kohei Nawaoka, Shinji Miwa, Seungyoung Park, _Yoichi Shiota, Chunyeol You, Jaehun Cho, Byungchan Lee, Yoshishige Suzuki, Kungwon Rhie
② Magnetostatic spin wave in a very thin CoFeB film grown on an amorphous FeZr buffer layer
③ Journal of the Korean Physical Society
④ **67**, 906 - 910 (2015)

(5) ① Minori Goto, Kohei Nawaoka, Shinji Miwa, Shohei Hatanaka, Norikazu Mizuochi, Yoshishige Suzuki
② Electric-field modulation of tunneling anisotropic magnetoresistance in tunnel junctions with antiferromagnetic electrodes

③ Japanese Journal of Applied Physics
④ **55**, 080304-1 - 080304-4 (2016)

(6) ① 鈴木義茂、野崎隆行、塩田陽一、縄岡孝平、三輪真嗣
② 電圧による磁気異方性と反交換相互作用の制御
③ 固体物理
④ 50 (11), 643-656 (2015)

LIST OF CONFERENCE PRESENTATIONS

Names written with an underline represents the thesis author
(① Authors, ② Title, ③ Conference name, ④ Place, Number and Date)

2013

(1) (Oral presentation)

① 縄岡孝平 , 三輪真嗣, 水落憲和, 新庄輝也, 鈴木義茂
② 強磁性共鳴による Fe ナノ粒子の磁気特性評価
③ 日本物理学会 2013 年秋季大会
④ 徳島大学、徳島、28aKM-14、2013 年 9 月

(2) (Poster presentation)

① Kohei Nawaoka, Yoichi Shiota, Shinji Miwa, Norikazu Mizuochi, Teruya Shinjo, Yoshishige Suzuki
② Voltage-induced-modulation of propagating spin-wave
③ 第 18 回 半導体スピン工学の基礎と応用 PASPS-18
④ Osaka Univ., P-24, Dec. 2013

2014

(3) (Oral presentation)

① Kohei Nawaoka, Yoichi Shiota, Shinji Miwa, Norikazu Mizuochi, Teruya Shinjo, Yoshishige Suzuki
② Electric modulation of propagating spin-wave in Fe
③ 59th Annual Magnetism and Magnetic Materials (MMM) Conference
④ Hilton Hawaiian, Honolulu, USA, GD-12, Nov. 2014

(4) (Oral presentation)

① 縄岡孝平, 塩田陽一, 三輪真嗣, 水落憲和, 新庄輝也, 鈴木義茂
② 薄膜 Fe 中のスピン波伝搬における外部電圧印可効果
③ 日本物理学会第 69 回年次大会
④ 東海大学、平塚、28aAF-1、2014 年 3 月

(5) (Oral presentation)

① 縄岡孝平, 塩田陽一, 三輪真嗣, 冨田博之, 水落憲和, 新庄輝也, 鈴木義茂
② スピン波電圧変調における伝搬方向対称性の評価

③ 日本物理学会 2014年秋季大会

④ 中部大学、春日井、7aBF-11、2014年9月

2015

(6) (Oral presentation)

① Kohei Nawaoka, Shinji Miwa, Yoichi Shiota, Norikazu Mizuochi, Yoshishige Suzuki

② Voltage induction of interfacial Dzyaloshinskii-Moriya interaction

③ 22nd International Colloquium on Magnetic Films and Surfaces (ICMFS)

④ AGH Univ., Krakow, Polish, July 2015

(7) (Poster presentation)

① Kohei Nawaoka, Shinji Miwa, Norikazu Mizuochi, Yoshishige Suzuki

② Qualitative analysis of voltage modulation of propagating spin waves in Fe

③ Magnonics2015

④ Kloster Seeon, Seeon Abbey, Germany, Aug. 2015(Oral presentation)

(8) (Poster presentation)

① 縄岡孝平, 三輪真嗣, 水落憲和, 鈴木義茂

② スピン波電圧変調における Fe 膜厚依存

③ 日本物理学会第70回年次大会

④ 早稲田大学、新宿、21PSA-22、2015年3月

(9) (Oral presentation)

① 縄岡孝平, 三輪真嗣, 塩田陽一, 水落憲和, 鈴木義茂

② Au/Fe/MgO 系におけるジャロシンスキー守谷相互作用の電圧変調

③ 日本物理学会 2015年秋季大会

④ 関西大学、吹田、18pCM-4、2015年9月

2016年

(10) (Oral presentation)

① Kohei Nawaoka, Shinji Miwa, Takayuki Nozaki, Shinji Yuasa, Yoshishige Suzuki

② Enhancement of voltage induced Fe|MgO Dzyaloshinskii-Moriya interaction change by insertion of 1 atomic layer Pt

③ 61st Annual Magnetism and Magnetic Materials (MMM) Conference

④ New Orleans Marriott, New Orleans, USA, Nov. 2016

(11) (Invited)

① 縄岡孝平, 三輪真嗣, 塩田陽一, 野崎隆行, 湯浅新治, 水落憲和, 鈴木義茂

② “電圧印加による Fe(001)薄膜における表面静磁波(MSSW)の制御－磁気異方性と反対称交換相互作用の電界効果－”

③ 第 11 回フォト・マグノニクス技術調査専門委員会 「マグノニクス機能性材料における準粒子協調現象～マグノン・フォノン・プラズモンの機能性材料開発の先端～」

④ 日本大学、東京、2016 年 6 月

(12) (Oral presentation)

① 縄岡孝平, 三輪真嗣, 塩田陽一, 野崎隆行, 湯浅新治, 水落憲和, 鈴木義茂

② Fe|MgO における界面ジャロシンスキー守谷相互作用の電圧変調

③ 第 63 回応用物理学会、春季学術講演会

④ 東京工業大学、目黒、吹田、22a-W241-6、2016 年 3 月

(13) (Oral presentation)

① 縄岡孝平, 三輪真嗣, 野崎隆行, 後藤穣, 湯浅新治, 鈴木義茂

② Fe|MgO 界面ジャロシンスキー守谷相互作用の電圧変調に対する PT 単原子層挿入効果

③ 日本物理学会 2016 年秋季大会

④ 金沢大学、金沢、14pAP-8、2016 年 9 月

LIST OF AWARD AND GRANTS

1. 博士課程学生海外派遣支援事業(学長リーダーシップ) 2015年
2. 日本学術振興会 科学研究費補助金 DC2 (No. 16J05624), 2016年～2018年
3. 日本物理学会、学生奨励賞(内定) 2017年